Investigation of the High-Throughput Analytical Performance of an FPA-FTIR Imaging System

By

Alexander L. Enfield

Department of Food Science and Agricultural Chemistry

McGill University, Montreal

Submitted: June, 2010

A thesis submitted to McGill University in partial fulfillment of the requirements of the Masters of Science Degree.

© Alexander L. Enfield –2010

Abstract/Résumé

Focal plane array (FPA) FTIR imaging spectroscopy provides unprecedented levels of spatially resolvable chemical information for analysis of samples at the micrometer scale. This study evaluates the quantitative performance characteristics of the individual detector elements comprising the FPA camera, and applies them to making analytical measurements of a custom designed microfluidic multichannel transmission cell. Statistical descriptions are provided for the response distributions among the FPA's detector elements; RMS noise, peak response, and linear regression parameters. It was found that individual detector elements of the FPA allowed for accurate milliabsorbance measurements, however the variability was large when contrasting detector elements due to FPA detector non-uniformity issues. When applied to the microfluidic multichannel sampling system designed for the monitoring of four fluid streams, it was found that the detector elements covering the fluid stream could be averaged to generate a very repeatable response between streams — thus allowing for milliabsorbance measurements of 4 samples simultaneously with the current design.

L'imagerie par spectroscopie IRTF dans la matrice plane focale (MPF) offre des niveaux de résolution spatiale sans précédent des informations chimique dans le domaine spatial pour une analyse des échantillons à l'échelle du micromètre. L'étude actuelle examine l'ensemble des applications de la spectroscopie IRTF (MPF) avec l'utilisation d'un système micro-fluidique multicanaux de transmission de cellules conçut sur mesure comme une approche potentielle d'une analyse quantitative des échantillons liquides à haut débit. Des descriptions statistiques sont fournies selon la répartition des réponses parmi ces éléments individuels du détecteur. La réponse des éléments individuels du détecteur dans la MPF a été démontrée comme étant reproductible dans des unités de milli absorbance et ainsi, la plus importante variabilité de réponse à travers l'ensemble est due aux problèmes de non conformité associés à la MPF. La moyenne des réponses des éléments du détecteur sur lesquels les résultats de chaque canal est imagées dans de bonne reproductibilité inter-canal et ainsi compense de manière satisfaisante la non-uniformité des pixels. Les expériences qui prouvent ce concept impliquant des mesures analytiques sur quatre échantillons visualisés simultanément avec la conception actuel des cellules sont présentées.

Acknowledgements

The author would first like to acknowledge my supervisor, Dr. Ashraf Ismail, for his guidance and support, and for accepting me as a graduate student out of the blue. I would also like to acknowledge David Pinchuk from Thermal Lube Inc. for agreeing to participate in my NSERC-FQRNT IIS as an industry partner; for without this scholarship none of this would have been financially possible. The opportunity to work at Thermal Lube throughout my research proved to be an invaluable experience, and I thank Dr. Emmanuel Akochi-Koblé and Dr. Tao Yuan for their assistance during this time. Andrew Ghetler, Moeed Haq, and Jacqueline Sedman were each instrumental in giving me a sense of direction during this project, and I thank them each very much for their insight and respective contributions to my work. Various machine shops assisted in the fabrication of necessary components for this project, thus I acknowledge the staff at the physics, mechanical engineering, and farm machine shops of McGill for their professional and timely assistance. Last but not least I would like to thank my family, friends, and (in particular) my girlfriend Mylène, for their un-conditional support and patience throughout my graduate work.

Table of Contents

Ab	stract/Resume		i
Acł	knowledgments		ii
Tak	ole of Contents		iii
List	of Figures		٧
List	of Tables		vi
List	t of Acronyms		vii
1.	Chapter 1: Intro	duction	1
	1.1. General Intro	oduction	1
	1.1.1.FTIR Spe	ectroscopy as a Quantitative Analysis Tool in the Food Industry	1
	1.1.2.FTIR Ima	aging	3
	1.2. Research Ol	bjectives	4
	1.2.1.General	Overview of Research Project	4
	1.2.2.Specific	Research Objectives	5
2.	Chapter 2: Litera	ature Review	6
	2.1. IR Spectroso	сору	6
	2.1.1.Concept	ts of IR Spectroscopy	6
	2.1.2.FTIR Ima	aging Spectroscopy	9
	2.1.3.IR Detec	ctors	12
	2.1.3.1.	Photoconductive and Thermal IR Detectors	14
	2.1.3.2.	Linear Array and Focal Plane Array Detectors	17
	2.1.4.IR Spect	roscopy for Quantitative Analysis	24
	2.1.4.1.	Condensed Phase Sampling	24
	2.1.4.2.	Transmission Measurements	24
	2.1.4.3.	Attenuated Total Reflectance Measurements	25
	2.1.4.4.	Calibration Methodologies and Figures of Merit	26
	2.1.4.5.	Quantitative Applications of FTIR in Food Analysis	29
	2.2. Micro-fluidi	cs	35
	2.2.1.Micro-fl	uidic Theory	37
	2.2.1.1.	Fluids and Fluid Flow	37
	2.2.1.2.	Transport Mechanisms	40
	2.2.1.3.	Fabrication Technology	43
	2.2.2.FPA-FTII	R Detection in Micro-fluidic Analysis Systems	46
	2.2.3.Other M	licro-fluidic Detection Techniques	50
	2.3 Conclusions		51

3.	Chapter 3: FPA-FTIR Spectrometer Evaluation	52
	3.1. Introduction	52
	3.2. Experimental	54
	3.2.1.Materials	54
	3.2.2.Instrumentation	54
	3.2.3.Sample Acquisition	54
	3.2.4.Data Processing & Analysis	55
	3.3. Results & Discussion	56
	3.3.1.FPA-FTIR Spectrometer Noise Performance Characterization	56
	3.3.1.1. Pixel Selection and Co-addition Strategies	61
	3.3.1.2. Atmospheric Interferences: FPA-FTIR Purge Issues	63
	3.3.2.Polystyrene Film Analysis	64
	3.3.3.Fluid Cell Measurements	72
	3.4. Conclusions	75
4.	Chapter 4: FPA-FTIR Spectrometer Quantitative Performance	77
	4.1. Introduction	77
	4.2. Experimental	79
	4.2.1.Materials	79
	4.2.2.Instrumentation	79
	4.2.3.Sample Acquisition	80
	4.2.4.Data Processing & Analysis	80
	4.3. Results & Discussion	81
	4.3.1.Aqueous Sodium Azide Calibrations:	
	Linear Regression Modeling of the FPA	81
	4.3.2.Multi-component Analysis of Milk:	
	MLR & PLS Modeling of the FPA	91
	4.4. Conclusions	97
5.	Chapter 5: High-throughput FTIR Sampling Accessories	100
	5.1. Introduction	100
	5.2. Experimental	102
	5.2.1.1. Materials & Equipment	102
	5.2.1.2. Samples	102
	5.2.1.3. Data Acquisition & Processing	102
	5.3. Results & Discussion	104
	5.3.1. Micro-fluidic Multichannel Transmission Cell	
	For FPA-FTIR Quantitative Analysis	106
	5.4. Conclusions	111
6.	Chapter 6: Research Summary and Conclusions	113
Cit	ations	117

List of Figures

Figure 1.1. Examples of FTIR imaging of heterogeneous sample types.	3
Figure 2.1. MIR spectrum; common spectra/structure correlation generalities. Figure 2.2. Basic Components of an FTIR Spectrometer.	6 7
Figure 2.3. Representation of a hyperspectral data-cuboid.	11
Figure 2.4. Surface response profile of an LiTaO ₃ detector crystal element	14
Figure 2.5. Historical development of IR detectors into array detectors.	15
Figure 2.6. Depiction of (a) LA and (b) FPA detector format.	18
Figure 2.7. Depiction of a typical FPA hybrid array architectures.	19
Figure 2.8. A novel non-uniformity correction algorithm applied to an FPA	21
Figure 2.9. 3D plot of an MCT FPA (a) before, and (b) after linear NUC.	22
Figure 2.10. Examples of HT-FPA-FTIRI studies	48
Figure 3.1. Average FPA RMS noise value from the region between 1800-1700 cm ⁻¹ .	56
Figure 3.2. Relationship between: RMS noise, scan co-additions, integration time.	57
Figure 3.3. Impact of scan co-additions and integration energy on pixel RMS SD	58
Figure 3.4. RMS noise distribution over the FPA.	59
Figure 3.5 . 2D plot of an RMS noise cut-off for the removal of high noise pixels	59
Figure 3.6. RMS SD per pixel, the result of 20 repeated scans.	60
Figure 3.7. RMS noise (1800-1700 cm ⁻¹) average per FPA column.	62
Figure 3.8. Plot of purge conditions versus RMS noise measure.	64
Figure 3.9. Optical and IR image of polystyrene.	65
Figure 3.10. Distribution of detector element response at 1942.31 cm ⁻¹	65
Figure 3.11. Variance spectrum from 1st derivative spectra for an image of PS. Figure 3.12 . IR image and histogram depictions of individual pixel consistency of	67
response.	68
Figure 3.14. Baseline corrected measurements from peaks covering a range of	69
absorbance. Figure 3.15. Repeated measurements of polystyrene.	70
Figure 3.16 Distributions of pixel peak height ratio 1583.554/1070.49 cm ⁻¹ .	72
Figure 3.17. Apparatus used for FPA-FTIR transmission cell measurements. Figure 3.18 Distribution of FPA response through a liquid film.	73 74
rigure 3.16 distribution of FPA response through a liquid film.	/4
Figure 4.1 Linear regression data for increasing levels of FPA pixel co-addition.	81
Figure 4.2. Trends for linear regression gains upon refinement of pixel population.	83
Figure 4.3. Plots of pixel regression features (CSD and CC) against RMS noise.	84
Figure 4.4. The day to day stability of various LR calibration features of NaN ₃ .	87
Figure 4.5. Histogram representations of CSD distributions for the NaN_3 standards. Figure 4.6. Impact of CSD and RE selection on the accuracy of pixel predictive	88
ability.	90

Figure 4.7. Optical and IR images of the FPA field of view of a stopped flow of milk.	91
Figure 4.8 . Trending of SDD _a and SDD _r for two sets of milk calibration standards. Figure 4.9 . RMSECV and CC distributions for the PLS calibration of milk	95
components. Figure 4.10 The level of RMSECV distribution versus the number of latent	96
variables.	97
Figure 5.1. Multichannel sampling apparatus.	104
Figure 5.2. FPA-FTIR image of the empty multichannel cell.	106
Figure 5.3. Scanning procedures of empty micro-channels	107
Figure 5.4. IR imaging of ethanol fluid flow through the multichannel structures. Figure 5.5. One scan calibration model of aqueous NaN_3 within the multichannel	108
cell.	111
List Of Tables	
Table 2.2. Descriptions for various IR detector formats.	16
Table 2.3. List of some commercially available IR based milk analyzers (2009).	31
Table 2.4. FTIR analysis of milk – examples from the past 20 years.	32
Table 2.5. IR spectroscopic analysis of alcoholic beverages.	34
Table 2.6. FTIR analysis of edible oils.	35
Table 3.1. RMS noise average per FPA division.	61
Table 4.1 NaN ₃ linear regression data for DTGS and for FPA pixel population.	82
Table 4.2. Filtering of FPA pixels based on various parameters.	85
Table 4.3. CV _{med} vs. CV for distributions of pixel calibration features. Table 4.4. LR-analysis of fat content and NaN₃ internal standard from milk	89
standards.	92

Table 4.5. Trending of MLR fit statistics upon refinement of pixel population.

93

List of Acronyms

AOAC Association Of Analytical Communities

ATR Attenuated Total Reflectance

CC Correlation Coefficient
CCD Charge Coupled Devices
CE Capillary Electrophoresis

CMOS Complementary Metal Oxide Semiconductor

CSD Calibration Standard Deviation

CV Coefficient of Variation

P* Specific Detectivity

EDL Electrical Double Layer

FIR Far IR

FPA Focal Plane Array

FPAIRI Focal Plane Array Infra-Red Imaging

FTIR Fourier Transform Infra-Red

FTIRI Fourier Transform Infra-Red Imaging
HPLC High Performance Liquid Chromatography

HTA High Throughput AnalysisHTS High Throughput Screening

LA Linear Array

LIF Laser Induced Fluorescence
LLS Least Linear Squares Regression

MCT Mecury Cadmium Telluride (IR detector)

MD_A Mean Difference of Accuracy
MD_R Mean Difference of Repeatability

MEM Micro-Electro-Mechanical

MIR Mid IR

MLR Multiple Linear Regression
NEP Noise Equivalent Power

NIR Near IR

NUC Non-Uniformity Correction
PLS Partial Least Squares Regression
PRESS Predictive Error Sum of Squares

PS Polystyrene RE Relative Error

RMS Root Mean Square (spectral noise)
RMSECV RMS-Error of cross validation

SDD_A Standard Deviation of the Differences of Accuracy SDD_R Standard Deviation of the Differences of Repeatability

SERS Surface Enhanced Raman Spectroscopy

SNR Signal to noise ratio

TR Time Resolved (FTIR Spectroscopy)

Chapter 1: Introduction

1.1 General Introduction

1.1.1 FTIR Spectroscopy As A Quantitative Analysis Tool In The Food Industry

Infrared spectroscopy is well established as a qualitative and quantitative analytical tool. The energies associated with the infrared region of the electromagnetic spectrum correspond to those required for transitions between vibrational energy levels of molecules so that IR spectroscopy provides valuable compositional and molecular structural information about a sample. In a properly conducted IR experiment there is also adherence to Beers law which forms the basis of any calibration methodology; as such the quantitative performance of IR spectroscopy has been well evaluated in a variety of contexts. Over the past few decades engineering developments in FTIR and FT-NIR spectroscopy, together with various ingenious sampling accessories, increasingly robust calibration methodologies, and ever-increasing computational capacities, have furthered the utility of this spectrographic technique, making it particularly effective in providing process analysis solutions. Many, if not most, of the novel process applications of FTIR and FT-NIR are proprietary, often making them difficult to precisely report 1. Examples of the successful application of IR spectroscopy as a process analysis tool range from ambient air monitoring, detection of impurities in liquid chlorine, trans-fat detection in edible oils, payment analysis for raw milk, rapid quality control of alcoholic beverages - plus hundreds of other examples in the petrochemical, pharmaceutical, materials, and biomedical sciences. In short, FTIR spectroscopy is a very robust and information rich technique with high applicability to a diverse range of products.

The emphasis of this thesis will be on the application of FTIR spectroscopy for quantitative measurements on (liquid) food systems – or on model systems relevant to food analysis. Proximate analysis of raw, in-process, or finished food products is the most common analytical requirement of the food industry, resulting in significant labour, capital, and operating costs ². Each of the major components of food systems (fats, proteins, and carbohydrates) has well-defined bands in the IR spectrum, which may be modelled in a variety of ways to obtain qualitative/quantitative information from FTIR analysis of a given food system. As already mentioned, a successful application of IR spectroscopy is the proximate analysis of raw milk for payment and

herd analysis purposes, whereby milk samples are analyzed for their fat, protein, and lactose content ³, the two former components being the most significant in terms of payment calculations. These measurements are often performed at central laboratories that may analyze hundreds of thousands of samples per annum, and thus the IR instrumentation employed in these labs has been specifically designed to be up to the task of accommodating these high sample throughputs, While IR milk analysis had its origins (*ca.* 1960) prior to the advent of FTIR instrumentation ³, most of the filter-based IR instruments that were employed for this purpose have been progressively replaced by FTIR systems. It may be noted that IR milk analysis is considered a secondary technique, i.e. it must be calibrated and periodically validated against reference analyses. Given that the IR milk analyzers operated in centralized laboratories are defining cash flow through a multimillion dollar industry, they must be monitored closely for their quantitative accuracy and precision, and hence there is often a reference laboratory operated in tandem with the FTIR lab at such facilities.

An offshoot of the success of IR milk analysis that illustrates the multifunctional utility of FTIR spectroscopy as an analytical tool is seen in the wine industry, where many larger wineries use FTIR spectroscopy to monitor from the commencement of grape ripening to the finished bottled product ⁴. Because FTIR spectroscopy allows for the rapid qualitative/quantitative multi-component analysis of wines at different stages of their production, it can be invaluable to oenologists and vintners alike. However, despite all the advantages of the technique, a difficulty with the application of FTIR spectroscopy to wine analysis arises from the complexity and diversity of the sample matrix, such that calibration models must often be built locally or restricted to similar product types. It then becomes difficult for a central laboratory that handles, for instance, a variety of imported wines to reliably analyze this whole range of products. Regardless of these difficulties, the market share for FTIR wine analyzers is anything but insignificant, and further improvements in chemometric modelling are sure to come.

There are many other examples of the application of FTIR spectroscopy to the analysis of food systems, both in industry and in academia (e.g. analysis of edible oils, monitoring of beer processing, analysis of grains, etc). Thus, the speed, non-destructive sampling, spectral resolution capabilities, amenability to automation, and overall cost-effectiveness of FTIR spectroscopy all go towards making it an increasingly attractive

analytical tool to many sectors within the food industry. In addition, with ever-growing pressures on the food industry in terms of production, quality control, and safety, laboratories require analytical techniques capable of a very high sample throughput – something that FTIR spectroscopy, through its application to milk analysis, has proven quite capable. As discussed below, recently developed focal-plane-array (FPA) FTIR imaging technology can potentially further enhance the sample throughput of FTIR spectroscopy by orders of magnitude and thus could have a significant role in the food industry and, in turn, in any other analytical sector with high sampling volume needs.

1.1.2 FPA-FTIR Imaging

Utilization of focal plane array (FPA) detectors in conjunction with FTIR microspectroscopy for the collection of IR images has been of growing interest in the last 10-15 years. The collected images consist of n×n pixels (typically, n = 32, 64, or 128), each constituting a full mid-IR spectrum, and thus FPA-FTIR imaging is commonly referred to as 'hyperspectral imaging'. The spatially resolved chemical information provided by FPA-FTIR imaging of heterogeneous samples can be visualized by extracting any feature of the measured IR spectrum from the resultant image and mapping it in a two-dimensional plot, hence the term 'chemical staining' sometimes used to describe FPA-FTIR imaging. This is often how IR imaging results are presented, with artificially coloured IR images illustrating a wealth of chemical/spatial information on a variety of samples (see figure 1.1).

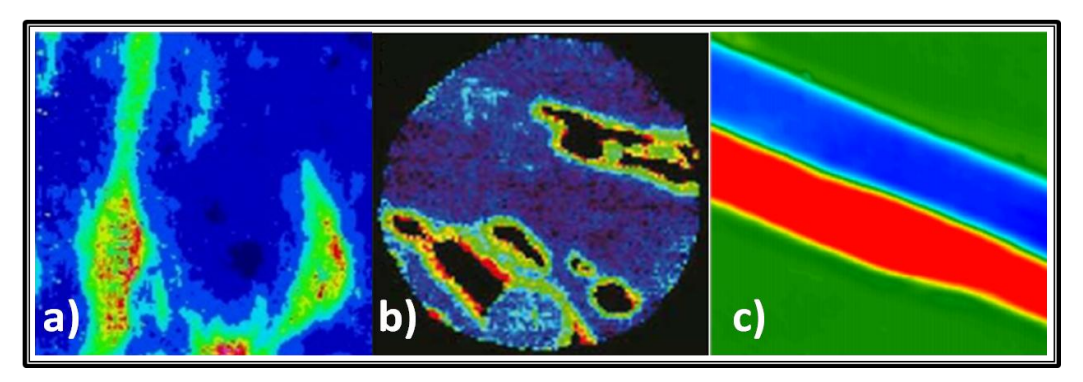


Figure 1.1. Examples of FTIR imaging of heterogeneous sample types: a) starch profile in imitation cheese ⁵; b) nucleic acid profile of prostate tissue⁶; c) forensic study of bicomponent fibres ⁷.

Many studies that utilize FPA-FTIR imaging technology do so in an effort to extract information using the high spatial resolution capabilities of the technique, i.e. the analysis is carried out on some type of heterogeneous sample to investigate the spatial-chemical features of that sample (figure 1.1). To date, the majority of applications using FPA-FTIR imaging have been within the biochemical and medical sciences, while it has also found its way into a variety of other fields including: materials science, forensic science, agricultural and food science ⁸.

Another aspect of FPA-FTIR imaging that has been much less extensively considered is its potential utility as a high-throughput analytical technique. The information-rich nature of mid-IR spectra combined with the enormous number of spectra acquired simultaneously by the FPA detector make this technique highly relevant in the era of high-throughput analytical sciences. However, several questions regarding the performance characteristics of FPA detectors need to be addressed in order to properly exploit this potential. First, the performance of each of the individual detector elements comprising the FPA becomes more significant in the context of high-throughput quantitative chemical analysis than it is when FPA-FTIR spectroscopy is utilized to probe progressive changes in chemical composition across heterogeneous samples such as those presented in figure 1. Second, in studies that have been conducted to characterize FPA detectors - mostly in relation to thermal imaging - a term that commonly appears is 'pixel non-uniformity', used to describe observations that the different detector elements of the array generate slightly different responses from one another. While a number of protocols have been proposed to address this issue, it is found that no single method can completely eradicate pixel non-uniformity. However, the effects of pixel non-uniformity in the context of high-throughput quantitative chemical analysis by FPA-FTIR spectroscopy have not yet been properly addressed.

1.2 Rationale & Research Objectives

1.2.1 General Overview of the Research Project

The overall objective of the research presented in this thesis is to investigate means of enhancing the sample throughput of FTIR spectroscopic analysis of food systems by exploiting the multichannel detection capabilities of FPA-FTIR imaging spectrometers. The approach proposed involves the development of a micro-fluidic multichannel

sampling accessory, the use of which in combination with an FPA-FTIR imaging spectrometer is envisioned to allow one instrument to perform the work of *m* conventional spectrometers, where *m* is the number of channels in the micro-fluidic cell. If one takes the example of milk analysis, where central laboratories run hundreds of thousands of samples per year, the sample throughput of such a system would be quite beneficial. The viability of this approach is contingent upon the capability of the individual detector elements in the FPA that record/build the image of each channel to provide satisfactory quantitative accuracy. Thus, the global aims of the research were (i) to assess the analytical performance of a 32×32 FPA detector through the study of several model systems, including milk calibration standards, and (ii) to fabricate a multichannel micro-fluidic demountable transmission cell and evaluate its potential utility in the context of high-throughput quantitative analysis by FPA-FTIR imaging spectroscopy.

1.2.2 Specific Research Objectives

The specific objectives to be addressed by the research are as follows:

- Development of image collection protocol for quantitative analysis applications:
 - Establishing stable environmental conditions within the instrument, including the microscope stage.
 - o Optimization of image acquisition parameters.
 - Assessment of FPA detector element response characteristics using multiple test systems (open-beam response, calibration films, model liquid systems).
- Assessment of FPA-FTIR spectrometer quantitative performance using gravimetrically prepared calibration standards and pre-analyzed milk calibration standards together with a conventional transmission flow cell.
 - Development of data extraction techniques.
 - Assessment of individual detector elements, groupings of detector elements, FPA as a single detector (averaging responses of 'all' detector elements).
- Development and testing of a micro-fluidic multi-channel transmission sampling accessory.

Chapter 2: Literature Review

2.1.1 Concepts of Infrared Spectroscopy

Infrared (IR) spectroscopy involves the interaction of a controlled source of IR radiation with a sample of interest, and the subsequent detection and interpretation of resultant changes to the source radiation upon this interaction. The IR region of the electromagnetic spectrum (EMS) is most often measured by convention with the inverse of the wavelength (in centimetres) – termed the wavenumber (cm⁻¹), and spans from roughly 10-14,000 cm⁻¹. This region is further subdivided into the near, middle, and far IR regions (NIR, MIR, and FIR respectively) each exhibiting different energetic interactions with molecular bonds.

The IR region constitutes the portion of the EMS associated with vibrational energy transitions of molecules, and thus IR spectroscopy is often referred to as vibrational spectroscopy (a term that also encompasses the complementary technique Raman spectroscopy). The interaction of a molecule with IR radiation is often portrayed as a physical vibration but is more accurately described as an excitation, within quantized vibrational energy states, of a molecule upon absorption of incident radiation matching one of its "fundamental" frequencies; some examples illustrated in figure 2.1.

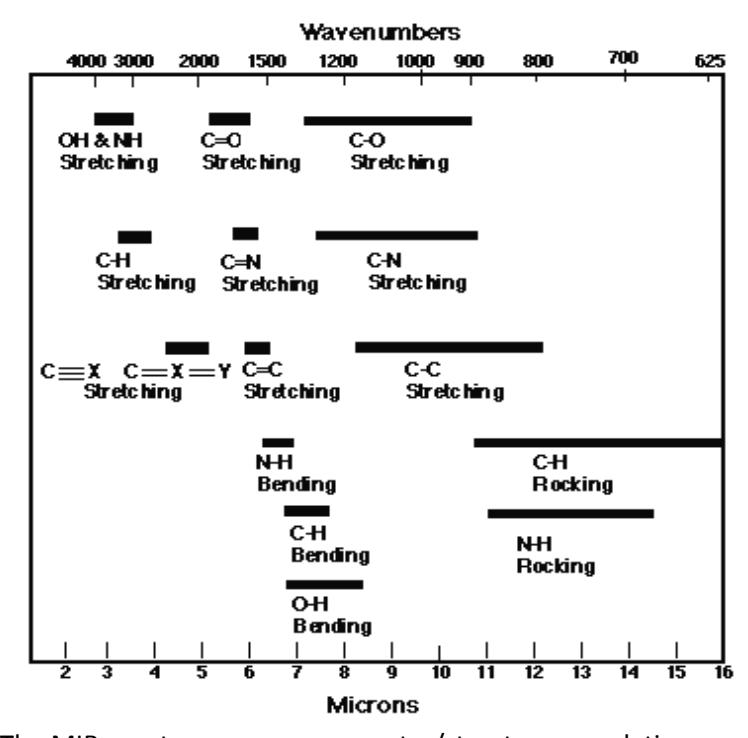


Figure 2.1. The MIR spectrum; common spectra/structure correlation generalities.

Modern IR spectrometers are said to have stemmed from the World War II era, where developments in electronic amplification methods, detector technologies, and the advent of double- beam spectrometers greatly increased their utility ^{9, 10}. The essential components of any IR spectrometer include a source of radiation (ranging from conventional Globar and Nernst glowers to the more modern free-electron laser and synchrotron sources), some means of resolving the wavelengths contained within the radiation from a broadband source (e.g., a monochromator or an interferometer), a detector, optical components directing/focusing the source radiation onto the sample and towards the detector, and a data collection/display system (e.g. PC, printout). Because there are few convenient materials that transmit a sufficient range of IR wavelengths, the optical components are nearly always reflective rather than transmissive, and because of a lack of 'bright sources' (until recently) the apparatus must enable a high throughput of the source energy ¹¹. IR detectors are of particular interest to this review and will be explored further in the following sections.

Dispersive IR spectrometers employ a monochromator to select a narrow bandwidth for analysis and are quite useful in process analysis applications where only a few selected wavelengths are needed for analysis, however collection of full spectra (e.g. spanning the MIR range) with a scanning monochromator is time-consuming and has been overshadowed by a superior approach, Fourier transform IR (FTIR) spectroscopy.

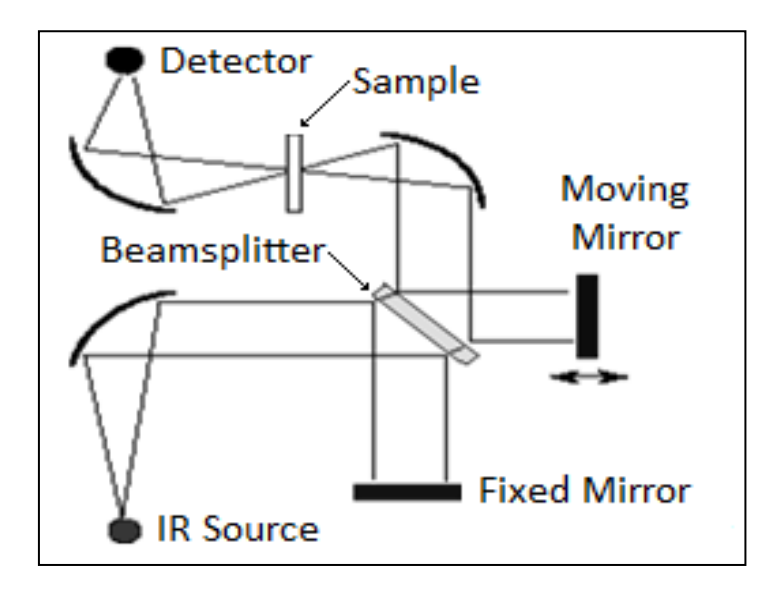


Figure 2.2. Basic Components of an FTIR Spectrometer ¹².

FTIR spectroscopy is a form of IR technology that has been available to researchers since the early 1970s. The advantages of FTIR over conventional dispersive IR spectrometers are derived from the replacement of a monochromator by the *two-beam interferometer*, the concept of which was originally developed by Michelson in 1891 ⁹. As depicted schematically in figure 2.2, the full bandwidth of the radiation from a broadband IR source is passed through an optical component called a beam splitter, which partially reflects and partially transmits the source radiation onto two mirrors, one of which is stationary while the other is moved backward and forward, either at a constant velocity (continuous-scan mode) or in fixed increments (step-scan mode). Owing to the varying difference in the distances traveled by these two beams when they are reflected back to the beam splitter, their recombination at the beam splitter results in a pattern of constructive and destructive interference (an *interferogram*) as a function of the *optical retardation* of the beam reflected back from the moving mirror.

The advent of FTIR spectroscopy is often said to have revitalized, if not revolutionized, the field of vibrational spectroscopy. Apart from collateral advantages accruing from the fact that FTIR spectroscopy necessitated that the spectrometer be equipped with a dedicated computer, the following fundamental advantages of this technique arise from its use of interferometry:

- All resolution elements are collected at all times (Fellgett's advantage).
- Efficient energy throughput at each resolution element (Jaquinot's advantage).
- Internal laser establishes wavelength stability, providing a universal reference for
 FTIR spectrometers enhancing reproducibility and repeatability of measurements.
- Significant reduction in scan time; sample throughput potential revolutionized.
- Superior spectral resolution and wavelength accuracy.
- Simpler/smaller instrumentation; portable devices are now commercially available.

A principal disadvantage of FTIR spectroscopy lies in the fact that it is a multiplexing technique in the time domain, making it quite sensitive to fluctuations in the source intensity – particularly periodic fluctuations, which will result in narrow spectral noise features ¹³. Another disadvantage of FTIR spectroscopy and IR spectroscopy in general, is that the achievable signal to noise ratio (SNR) is often limited by the detector used in the system.

2.1.2. FTIR- Imaging Spectroscopy

FTIR imaging (FTIRI) is defined as a spectroscopic technique that employs FTIR microscopy and multichannel detector (array) technology for the rapid and simultaneous acquisition of a set of n spatially resolved IR spectra (where n = the number of detector elements in the array) ¹⁴. Strictly speaking, there are three methods for the collection of FTIR images: 1) the original point-by-point "mapping" technique using a single-element detector and an x-y stage, 2) the use of a linear array (LA) detector, and 3) the use of an FPA detector. Each of these has its advantages and disadvantages, and many examples employing some combination of the three can be found in the literature.

A common thread between the three FTIR image building techniques is that each usually employs an IR microscope, although FTIRI has also found application on a macroimaging scale. The IR microscope is analogous to an optical microscope, with the exception of a few key difference: 1) IR radiation from the interferometer as its source; 2) reflecting optics; 3) an aperture at the primary image plane for sample definition; and 4) an IR-sensitive detector 15 . A minor difference between conventional IR microscopes and imaging IR microscopes is that the latter are designed for homogenous illumination over the field of view, while the former are designed for maximum light throughput 16 . A regular feature of IR microscopes is that they incorporate a white light microscope in the same optical path as the IR microscope. The limiting spatial resolution in IR microscopy is roughly 2λ – also known as the diffraction limit. Thus, on going from high to low wavenumber in a spectrum, the attainable spatial resolution is diminished. For a typical mid-IR spectrum, the spatial resolution at the focus will range from 5 to 30 μ m 15 .

The first image collection method mentioned above, point-by-point mapping, has an obvious time disadvantage with respect to the other two (in that a spectrum corresponding to one pixel in the image is collected, the sample moved, the spectrum corresponding to the next pixel in the image is collected, and so on), countered by the advantage of flexible pixel size through adjustments to the aperture. Typically, the spatial resolution is no better than 15 μ m ¹⁴. Mapping techniques that employ a synchrotron IR beam-line and a technique called compressive imaging have recently been reported to offer diffraction-limited spot sizes, a higher SNR, and no requirement for mapping at every spatial point - hence increasing the speed of the process ¹⁷.

The second image collection method, which employs an LA detector consisting of m individual detector elements (most commonly 16), allows m spatially resolved spectra to be collected simultaneously. The building of a full $n \times n$ image of a sample requires n^2/m 'sweeps' and therefore this technique may be considered a hybrid of point-by-point mapping and FPA imaging, and to some it is simply a stepping stone to the advent of FPA-FTIRI. However, an advantage of the technique appears to be that the fabrication of 16 high-quality detector elements is easier to accomplish than that of the >1000 detector elements found in FPAs, effectively reducing non-uniformity issues. In their study comparing confocal synchrotron single-point mapping with LA-FTIRI, Miller et al. ¹⁸ found that higher spatial resolution could be achieved with the synchrotron mapping method; however, the LA detector was still able to provide faster data collection at a reasonable resolution. Thus, the synchrotron mapping system lends the potential advantage of better spatial resolution; however, the need for access to a synchrotron source limits the technique's availability, and it is still much slower than the LA and, in turn, the FPA methods of image collection, each of which provides reasonable spatial resolution.

The third method of image collection involves the simultaneous collection of all pixels of the image using an FPA detector, lending an obvious speed advantage relative to the other methods of image collection described above. For example, a typical FPA format of 64 x 64 detector elements allows for the collection of 4096 high-quality IR spectra within minutes, generating a 'three-dimensional data cube', often referred to as a hypercube – but perhaps more correctly referred to as a hypercuboid ¹⁹. These hypercuboids consist of both spatial and spectral information, generally configured with spatial information in the x and y directions, and spectral information in the z-direction, as represented in figure 2.3. The information within the data cube is typically displayed as: 1) all of the z (spectral) data points at one x, y (spatial) location or 2) one of the z data points at all of the x, y locations ²⁰. The process of hyperspectral data cube building is described in further detail elsewhere ¹⁴.

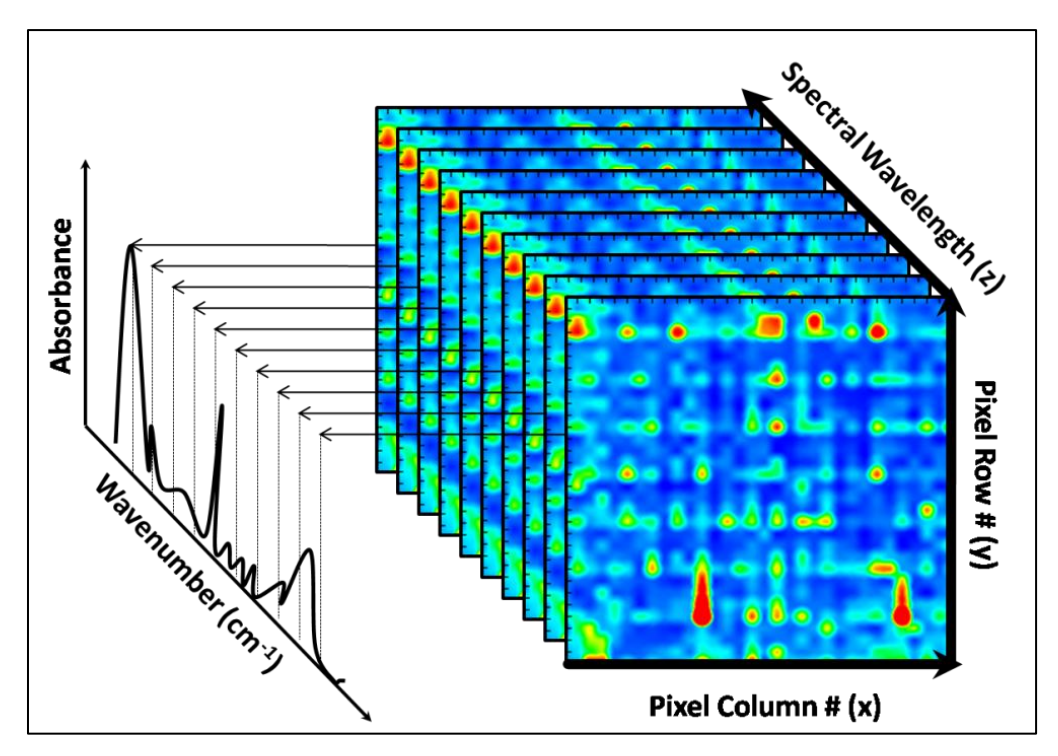


Figure 2.3. Representation of a hyperspectral data-cuboid. Each point along the z-axis represents a spectral feature plotted in the spatial (x, y) plane as a color intensity, red=high and blue=low. Note that the depicted spectrum is fictitious, present purely for illustrative purposes.

The multichannel detection capabilities of FPA detectors enable the monitoring of dynamic chemical processes, spatially resolved characterization of large heterogeneous samples, and the simultaneous characterization of many small samples. There are a range of accessories available for FTIRI purposes, including a selection of Cassegrain objectives with varying magnifications and numerical apertures, lending some flexibility to the spatial resolution capabilities of the instrument ⁸. Additional developments in ATR sampling accessories enable further improvements of the spatial resolution, due to the high refractive index of an ATR crystal, which thus can serve as a solid immersion lens — while there are also macro-ATR sampling accessories for the imaging of larger sample areas ⁸. Recently, there have also been developments in the combination of a synchrotron radiation source with FPA-FTIRI systems, giving advantages of 1) better SNR than with a Globar IR source, 2) higher spatial resolution, and 3) very short acquisition times ²¹. Again, the limited availability of a synchrotron light source does not make this a realistic solution for the average laboratory.

Two modes of data acquisition, each originating in conventional FTIR spectroscopy, may be employed in FPA-FTIRI: 1) the step-scan mode and 2) the continuous-scan mode; detailed descriptions of these image collection schemes may be obtained elsewhere 16. In the first FTIRI systems, the step-scan mode was exclusively employed owing to the slow frame rates of the first-generation FPAs, such that the detector read-out electronics were not capable of sampling every point of an interferogram as in modern continuous-scan systems ¹⁶. An advantage of the step-scan mode is that the retardation in a step-scan modality is decoupled from the time domain; thus, each point of the interferogram can be measured for any desired length of time. This capability has allowed for substantial SNR enhancement in monitoring repeatable transient events ¹⁶. Disadvantages of step-scan systems include additional controls and higher cost, plus a time requirement for stabilization of the interferometer before data collection may commence. As late as 2005 it was believed that step-scan interferometry was the most practical way to conduct FTIRI experiments, though it was acknowledged that advancements in detector technology were already making continuous-scan systems viable ¹⁶. The continuous-scan mode has become the standard method for image collection, due largely to the development of second- and now third-generation FPAs, which have frame rates of up to 3000 Hz ⁸. The continuous-scan mode is more time efficient in the collection of signals from the FPA, as there is no time spent on the stabilization of the interferometer at specific retardations. The SNR achievable with continuous-scan systems is limited by the positional error (~10-25 nm) of the moving mirror within the interferometer, making imaging in continuous-scan mode an inherently lower SNR technique than imaging in step-scan mode. The SNR can be improved by increasing the number of co-added scans, though this does diminish the time advantage of the continuous acquisition scheme over the step scan.

2.1.3. IR Detectors

Modern FTIR spectrometers are often described as 'detector noise limited', meaning that the fluctuations of the detector component represent the main source of noise in the measured signal. Detector type will also define the wavenumber range of the recorded IR spectrum, the speed of response, and the dynamic range of response – in essence, the detector has a very significant impact on the end quality of spectral data. It

is therefore constructive, when discussing detector technology, to define terms which allow the properties of detectors to be properly assessed and compared. Conventionally used descriptions of IR detector performance include ²²:

- Signal to noise ratio (SNR): Ratio of the signal to the noise corrupting the signal (see equation 4); the higher the SNR, the less obtrusive the noise.
- Responsivity: Ratio of electrical output (volts or amps) to the incident IR power (watts); defines ability of a detector to convert IR radiation into an electrical signal.
- Noise equivalent power (NEP): Ratio of the noise power per unit bandwidth (noise power density) at the detector output to the detector responsivity (W Hz^{-1/2}); used for describing a detector's ability to measure small signals.
- Specific detectivity, $D^* = Area^{1/2}/NEP$: Ratio incorporating detector active area and NEP, equivalent to the SNR of a detector of unit area in a unit bandwidth when one watt of power is incident on the detector (cm $Hz^{1/2}$ W^{-1}); dependent on measurement conditions, which must therefore be defined.
- Response time, τ: Defines how quickly the output of a detector can follow a dynamic incident signal.
- Linearity: Condition achieved when a detector's output is proportional to the IR signal being measured. Detectors may be inherently linear; however, the entire detection system can be made nonlinear if utilizing unsuitable read-out electronic hardware.
- Spatial uniformity of response (figure 3): Describes the largest deviation of the detector response at different points on the active area, expressed as a percentage of the maximum response. Nonuniform response may be a consequence of poor fabrication techniques, impurities within the active area, and variable thickness of detector element(s).

$$\label{eq:SNR} SNR = \frac{U_{\bar{\nu}}(T)\Theta\Delta\bar{\nu}\,\xi}{NEP}t^{1/2},$$

Equation 2.4. Expression of SNR for conventional wide beam single element detector in an FTIR spectrometer using Michelson type interferometer. See reference for full derivitization and meaning of each component of the equation ²³.

The D* is one of the more versatile measures of detector performance, and it is often said that it should be the starting point in every detector selection process ²². The advantage of knowing the D* is the ability to compare detectors of different active areas; once a group of detectors has been selected with known active areas, the NEP may be individually determined for further interpretation of detector performance.

The last point in the list above brings up the issue of the possible spatial non-uniformity of detector response as a result of physical imperfections in the detector, such that different regions of the detector exhibit slightly different responsivities. To illustrate this point, the surface response profile of a pyroelectric LiTaO₃ detector is depicted in figure 2.4, showing the extent to which the response may be distributed over a single detector due to variations in crystal thickness ²².

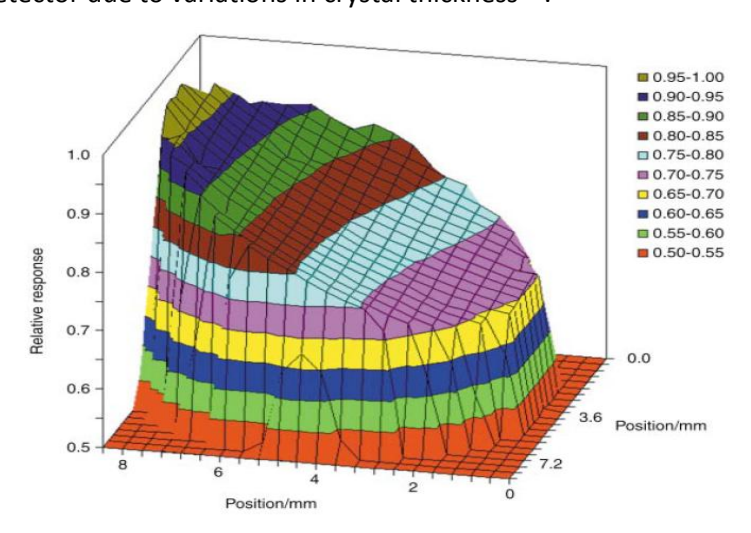


Figure 2.4. Surface response profile of an LiTaO₃ detector crystal element ²².

2.1.3.1. Thermo-detectors and Photo-detectors

Figure 2.5 depicts the historical development of IR detection materials, and from this list the generalization can be made that "all physical phenomena in the range of 0.1 to 1.0 eV may be proposed for IR detection" ¹⁰. This encompasses a range of possibilities, but the most common found within the field of IR detection may be subdivided into two main categories: thermal and photon detectors ²². The former category of detectors monitors any physical process affected by a temperature change generated by an incident radiation and includes thermocouples, thermistors and bolometers. The fundamental limit to the sensitivity of thermal detectors is determined by the random temperature fluctuations in the detector element ¹⁰. A further (general) limitation to

thermal detectors is that their response times are rarely faster than 1 millisecond (ms). Thus, the response times of the thermal detectors that were traditionally employed in IR spectroscopy are too slow to allow their use in FTIR spectroscopy. This limitation has been overcome through the use of pyroelectric. bolometers, particularly the deuterated triglycine sulfate (DTGS) detector commonly supplied with FTIR spectrometers. Although this detector has relatively low detectivity at higher frequencies and a slower response than photon detectors, it does possess numerous advantages, such as the ability to operate at room temperature, light-weight components, and relatively low cost. Overall, the DTGS is a very rugged detector which serves its purpose quite well.

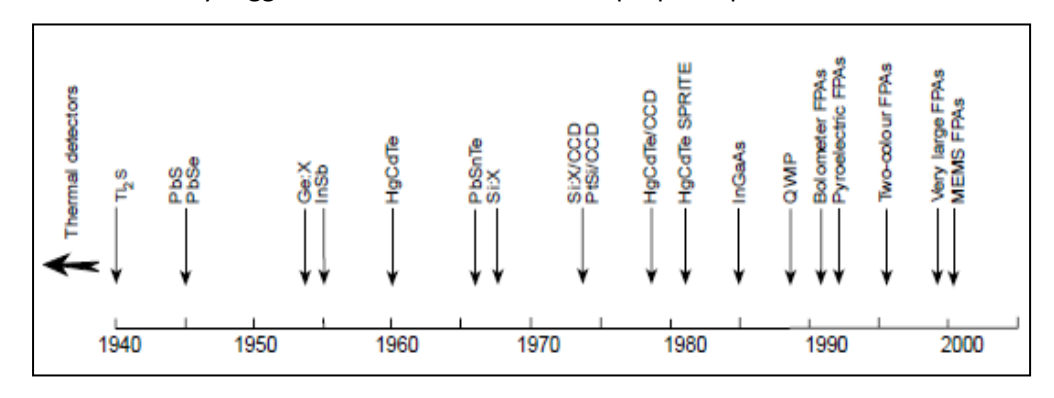


Figure 2.5. Historical development of IR detectors into array detectors ¹⁰.

Photodetectors are founded on the photoelectric effect whereby a photon with threshold energy, collides with a substance (e.g. the detector material) releasing an electron and creating an electrical response that is interpreted as the signal. More precisely, within a photodetector the incident radiation increases the mobility of a charge carrier by increasing its energy substantially enough to move it from the valence band of a semiconductor material to the conduction band where it is free to move under the influence of an electric field ²². It follows that photon detectors must be constructed from some type of semiconductor material; the most commonly used semiconductor material over the past four decades has been mercury-cadmium-telluride (Hg_xCd_{1-x}Te, or MCT by convention), which encompasses the MIR and FIR spectral regions. Materials science has led to the growth/production of a wide variety of semiconductor materials (see figure 4), but to date MCT remains predominant in the fabrication of photodetectors for the 1-25 µm range ¹⁰. These photodetector materials typically exhibit an increase in D* with increasing wavelength, with a sharp cut-off after a certain point ¹⁰. The more common MCT detectors are considered *intrinsic*

photoconductive detectors, defined as possessing a relatively low energy band gap upon irradiation compared with the energy of the IR radiation being detected. *Extrinsic* photoconductive detectors, which are defined by their relatively large energy band gaps, are also available. Existing *extrinsic* photodetectors generally require extreme cryogenic conditions (~4 K) to achieve D* equivalent to that of an *intrinsic* MCT detector, while due to their lower dielectric constants they possess inherently faster response times than *intrinsic* photodetectors ²².

Detector Type:	D* (cmHz ^{1/2} W ⁻¹)	Comments:
Ge(Ga), Bolometer	3 x 10 ¹³ (< 4 K)	Broad spectral response, liquid helium
	(11.7	temperatures of operation.
	10 ⁸ - 3.5 x 10 ⁹ (rt)	Spectral response, 6000-350 cm ⁻¹ ; only
DTGS, pyroelectric		thermal detector operating at room
		temperature
InGaAs, p.v.	$10^{13} - 10^{14} (77 \text{ K})$	Spectral response, ~6800 cm ⁻¹ to visible
	10 - 10 (77 K)	(@ 77 K); low spatial non-uniformity.
	10 ⁸ - 10 ¹⁰ (193 K)	Spectral response, 10000~1500 cm ⁻¹ ,
PbSe, <i>p.c.</i> (<i>i</i>)		active control of detector temperature is
		required.
InSb <i>p.v.</i>	~10 ¹¹ (77 K)	Spectral response, 10000 – 1800 cm ⁻¹ ;
	10 (77 K)	good spatial uniformity and linearity.
		Different Hg _x Cd _{1-x} Te mixes can modify the
Ha Cd To no (i)	10 ⁹ – 10 ¹¹ (77 K)	spectral response; typical = 5000 – 850
$Hg_xCd_{1-x}Te p.c.$ (i)		cm ⁻¹ . Relatively poor spatial uniformity
		and limited dynamic range.
Co. Cu n o (o)	$10^9 - 10^{10} (4 \text{ K})$	Spectral response, ~5500 – 350 cm ⁻¹ ;
Ge: Cu <i>p.c.</i> (e)	10 – 10 (4 K)	liquid helium temperatures of operation.

Table 2.2. Descriptions for various IR detector formats. p.c. = photoconductive; p.v. = photovoltaic; i = intrinsic; e = extrinsic; rt = room temperature.

Main advantages of photodetectors over thermal detectors include: a significantly faster response time (τ) (~10⁻⁹ seconds), and response over a narrower range of the spectrum generating lower thermal background noise and a higher D* ²². In order for the *intrinsic* MCT to achieve these conditions however, it must be cooled to ~77 K (see table 2.2). The fact that photodetectors generally require a bulky cooling unit combined with the associated overhead costs of cryogenic cooling introduces a disadvantage to the technology. As previously stated, *extrinsic* photo-detectors are further limited in this sense due to their liquid helium operating temperatures (4 - 30 K). It was observed by Theocharous that there was a drift in the spectral responsivity of cryogenically cooled

MCT detectors at specific wavelengths (3.1, 11-13 μ m), a phenomena attributed to the gradual development of an ice layer within the Dewar on the active area of the detector 24 . These effects were found to be temporarily treated by evacuating and baking the Dewar at 50°C for 48 hours, and it was cautioned that liquid nitrogen cooled Dewar's containing rubber O-rings resulted in the largest ice build up with time. It has been stated that current engineering advances have largely eliminated the issue with newer instrumentation 25 . Further disadvantages of the MCT detector specifically include: variable reproducibility with crystal growth, requirement of hazardous chemicals for production, high degrees of spatial non-uniformity, and a restricted dynamic range of response. Despite its assortment of problems the MCT detector remains in high rotation within IR instrumentation as a higher end detector technology.

2.1.3.2. Linear Array and Focal Plane Array Detectors

The terms linear array (LA) and focal plane array (FPA) refer to a collection of IR detector elements in a linear or 2D arrangement, allowing for the collection of spectra at all detector elements simultaneously ¹⁸. LAs and FPAs are sometimes referred to as scanning arrays and staring arrays, respectively, both conventions arising because of their respective mechanisms of image collection (see figure 2.6). The terms FPA and LA are restricted to detectors which are IR sensitive, but these detectors are analogous to detectors operating in the visible spectrum, e.g. charge-coupled devices (CCD) or complementary metal-oxide semiconductor (CMOS) sensors. The utilization of an FPA or LA detector within an FTIR apparatus has provided researchers with powerful instrumental multiplexing capabilities ²⁶. Within the past two decades the number of relatively low-cost, high quality, and commercially available LAs and FPAs has been on the rise ²⁷ – refer to the latter portion of figure 4 to appreciate the trends in development. The rate of FPA development is comparable to that of RAM technology but lags behind in terms of chip size by about 10-15 years, indicative of the potential growth in FPA technology ¹⁰.

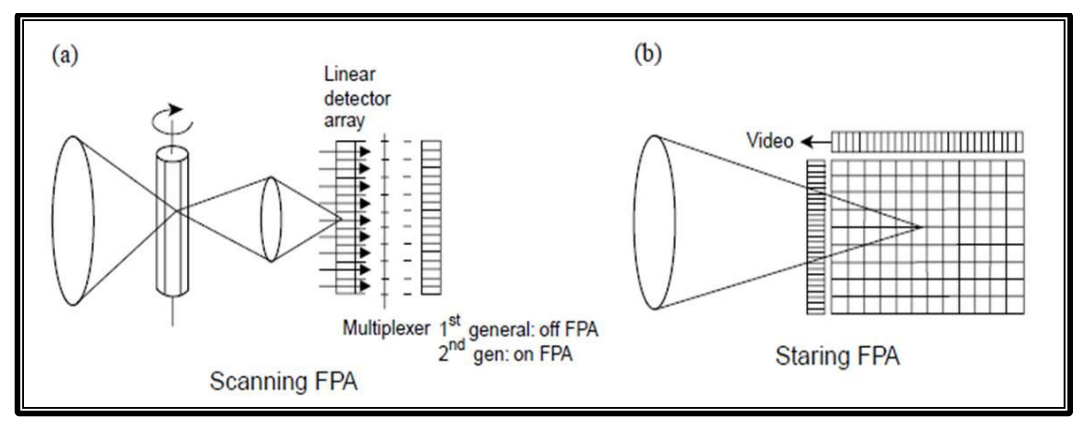


Figure 2.6. Depiction of (a) LA and (b) FPA detector format ¹⁰.

As with conventional IR detectors, the type of imaging detector selected for measurements will critically impact the speed of data acquisition and the quality of the recorded data, but a further consideration in the case of imaging detectors is the quality of the individual detector elements ²⁸. In this regard, the different architectures of LAs and FPAs must be considered. Essentially, any array design must be able to perform three fundamental tasks: photon detection, charge storage, and multiplexed readout. In this regard, LAs and FPAs are classified as monolithic and hybrid detectors, respectively (see figure 2.7 for a depiction of hybrid architecture); the former performs the three tasks upon the same chip, whereas the latter performs photon detection within a narrow band-gap semiconductor and then transfers the signal to a silicon multiplexer (one contact per detector) ²⁹. It is apparent in figure 2.7 that there are minor differences in the surface areas of each of the detector elements, the consequences of which will be elaborated on below. The greater complexity of the hybrid detector architecture is compounded by the much larger number of individual detector elements in FPAs as compared to LAs; the latter typically consist of 16 detector elements, whereas common FPA formats range from 32x32 to 256 x 256, with the individual detector elements typically measuring tens of microns to a side, and the complete array on the order of square millimetres ¹⁶. In addition, it has been reported that LA detectors have better SNR performance than FPA detectors ³⁰, though the argument that this is offset by time of analysis is often made ¹⁹.

FPA detector technology has undergone considerable development since the first example of FPA-FTIRI was reported in 1994 ²⁶, with current state-of-the-art FPA detectors being classified as third-generation FPA technology. The first-generation FPA

detectors had frame rates of less than 20 Hz, necessitating image acquisition in the step-scan mode, while the second- generation FPAs, which became available ~6 years ago, were much faster and could be utilized with a continuous-scan interferometer, although they still had stability issues with respect to the response of the individual detector elements ⁸. With the current third-generation FPAs, which became available ~3 years ago, the stability issues have been addressed to an extent and the detector uniformity is said to be significantly improved relative to the earlier generations ²⁹.

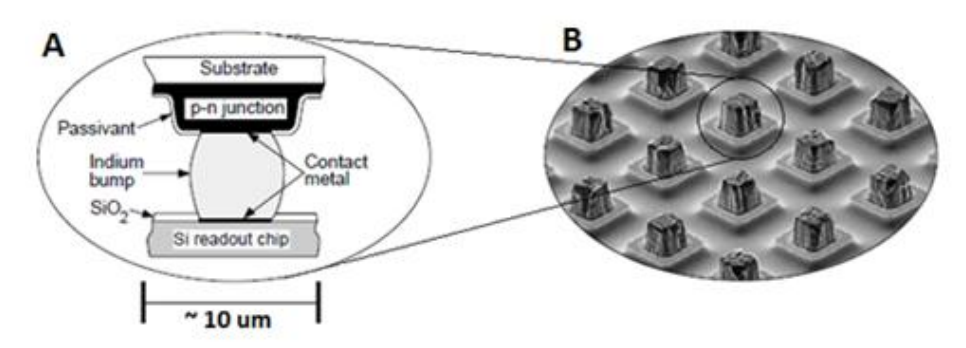


Figure 2.7. Depiction of a typical FPA hybrid array architecture; a) Detector element architecture, b) visual image of detector array segment ¹⁰.

As described in the previous section, various materials may be used for IR detection - array detectors are no exception; examples of materials that have been incorporated include InSb, MCT, silicon arsenide (Si:As), and barium strontium titanate (BST) ²⁸. For further reference, a summary of the key parameters of various representative FPA formats from major manufacturers is presented in a review by Rogalski 10. Analogous to conventional IR detectors, MCT has been the most utilized material, owing largely to its availability and affordability while providing access to the fingerprint regions of the IR spectrum (extending to 750 cm⁻¹ in the case of third-generation FPAs) ^{8, 28}. As previously stated, MCT detectors require cryogenic cooling - as do many of the other semiconductor materials used in IR detector array fabrication - in order to control thermal generation (thermal noise) and achieve higher performance ¹⁰. It has been observed that the continuous temperature cycling of array detectors can result in debonding and edge delamination, resulting in the gradual development of inoperative pixels ¹⁴. Owing to the disadvantages of cooled detector arrays, there have also been considerable efforts by both the US Department of Defense and the commercial circle to further develop thermal detector arrays due to their superior durability, facile implementation, and higher pixel densities at significantly lower cost ²⁵. Developments in micro-bolometer and ferroelectric detector arrays (the former being more mature than the latter) are expected to compete for detection purposes in the spectral region below 12 μm (< 800 cm⁻¹) ³¹. The BST hybrid array illustrates a current uncooled photodetector format; advantages include lower manufacturing costs, lower installation and maintenance cost, possibility for larger formats, sensitivity to longer wavelengths than second-generation MCT-FPAs (useful for investigation further into the fingerprint region of the mid-IR spectrum), and of course no need for time-consuming/expensive cryogenic cooling and the associated consequences of temperature cycling ¹⁴. Another recent study reports an uncooled 128x128 micro-bolometer FPA detector integrated within an already well-developed CMOS format, demonstrating a simple, low-cost fabrication process, capable of generating a detector array with respectable performance ³². However, the key disadvantage of thermal detector arrays is that their sensitivities are currently inferior to those of photodetector arrays, a significant drawback when looking to make quantitative measurements of chemical systems.

Aside from cooling issues, there exist more fundamental problems with IR FPA technology in its current state. The issue of non-uniformity between detector elements is a well-characterized problem of FPAs, as it is of some concern in that the purpose of the technology is to obtain spatially resolved (thermal and chemical) images of scenes/samples. There is a response pattern embedded within each FPA due to the imperfections in the fabrication process (see figure 2.8), an effect initially so severe that it impeded the development of FPA technology for several years ³³. This issue arises because all of the detectors and much of the multiplexing electronics are fabricated collectively, and there is little possibility for post-processing of individual detector elements ²⁹. Non-uniformity problems are compounded by the driving forces behind FPA technology, i.e. the desire for increasingly large detector array formats constructed from novel semiconductor materials, resulting in less developed fabrication techniques and more potential for irregularities among the detector elements within the array. As a consequence of this embedded non-uniformity, individual detector elements in the array exhibit differences in their respective spectral response, which has an impact on interpretation of FPA-FTIR images ³³. In order to be assessed, detector non-uniformity must be measured in the time domain to compensate for the effects of temporal (white) noise – this can be accomplished through co-additions of scans in spectroscopic

measurement or frames in thermal camera measurements. Once the pattern is established, it may be compensated for through non-uniformity correction (NUC) techniques. The most commonly applied FPA correction is referred to as a two-point NUC. This standard technique involves measurements at two irradiance levels, and the responses of each detector element are employed to calculate individual offset and gain corrections for each element, thus forcing the detector output to be (ideally) uniform across the FPA for these two irradiance levels (see figure 2.9) 34. More elaborate correction procedures range from simply extending the two-point NUC by measurements at additional irradiance levels to fuller algorithmic treatments which attempt to more thoroughly model the detector element non-uniformities (see figure 2.8) 35-40. The downside of increasingly exhaustive NUC techniques is the corresponding increase in the computational power required, compounded by the fact that these NUCs must be conducted regularly due to the often variable nature of detector element nonuniformity over time ³⁹. Through the application of NUCs, the performance of the detector array can approach temporal noise-limited characteristics, though it is noted that patterned noise will often persist even after rigorous treatments 35. Thus, an additional term to be defined for FPA response characterization is spatial noise, the nonuniform noise patterns that persist after NUC procedures. Spatial noise exists primarily due to the fact that non-uniformity is difficult to model, and there always exist random variations in camera operating conditions and environmental conditions ³⁶.

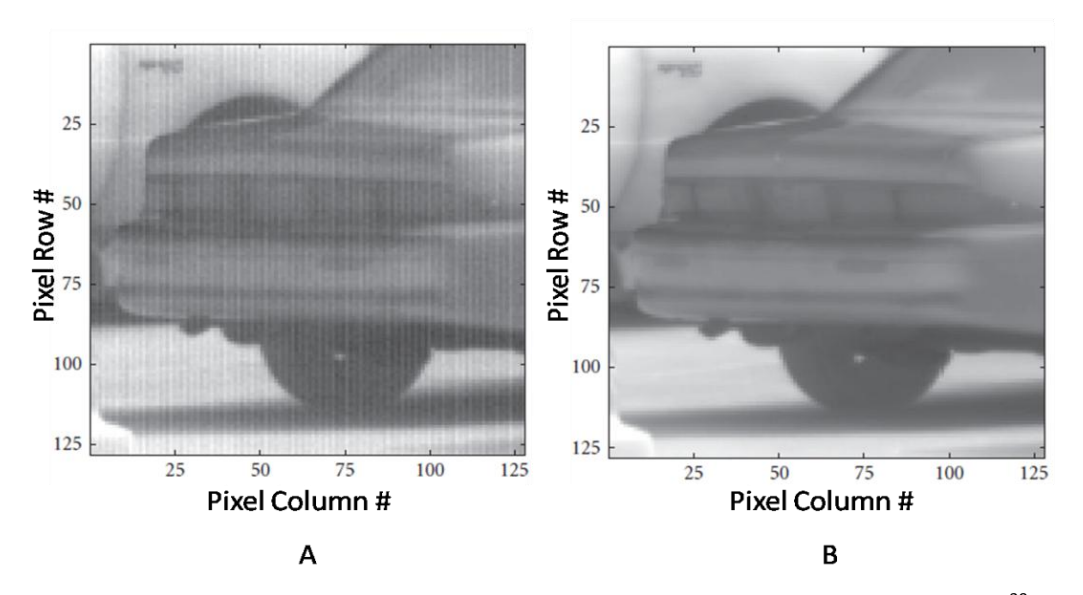


Figure 2.8. A novel non-uniformity correction algorithm applied to an InSb 128 x 128 FPA ³⁹.

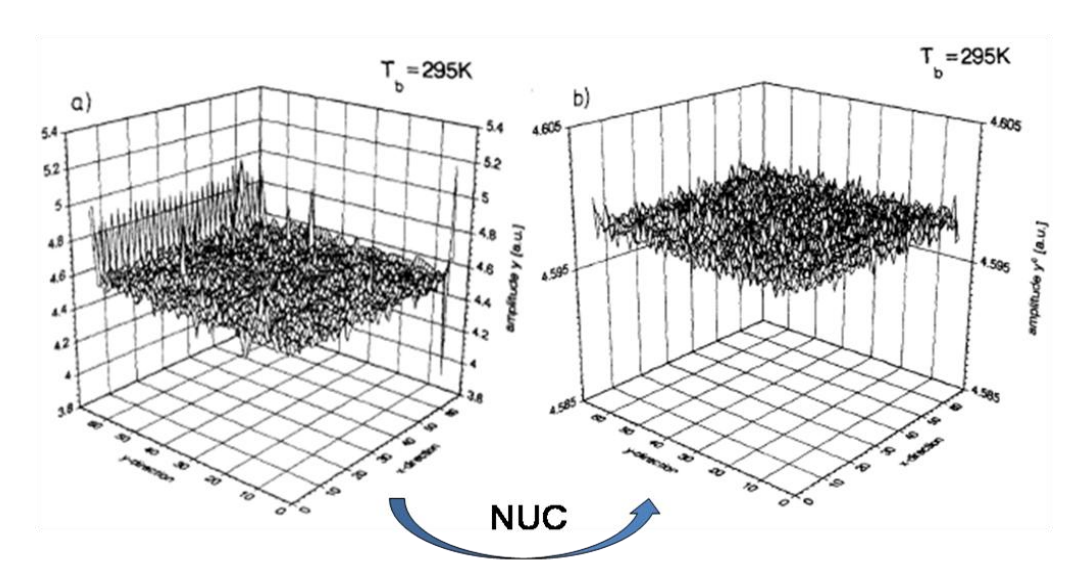


Figure 2.9. 3D plot of an MCT FPA (a) before, and (b) after linear non-uniformity corrections (NUC). Pixel coordinates on the x, y axes, detector element response value on the z-axis 41 .

Other issues with FPA detectors include ^{29, 36}:

- Limited spatial resolution capabilities compared with optical microscopy techniques.
- Poor detector element SNR; charge transfer efficiency and crosstalk problems.
- Detector element saturation leading to requirement of DC suppression and subframe integration strategies – leads to more complexity in electronic readout systems.
- High investment costs due to these detectors being produced for high priority/low volume applications; note that growing interest in FTIR imaging is shifting this trend.

In assessing FPA performance, the most common measures of detector performance (D* and NEP) have been reported to be inadequate ³³. The use of these parameters rests on the implicit assumption that all detector elements in the array are exactly the same and thus does not account for FPA detector element response variations. As a consequence, expectations of FPA detector performance based on these figures of merit are often very optimistic. A parameter proposed by Mooney et al. ³³ is the contrast signal-to-noise ratio (CSNR), a parameter similar to the NEP and D* in that it incorporates signal- independent noise and shot noise, but goes further by including the

spatial noise of the FPA. This same group describes two principal means of quantifying FPA non-uniformity: 1) task-based and 2) reference-based techniques ³⁶. Task-based techniques involve the measurement of some controlled system – the detection of a 4-bar pattern of adjacent hot and cold bars with the FPA detector is a classic example of a task-based technique used with thermal imaging FPAs. The figure of merit used for this task-based techniques is the minimum resolvable temperature (MRT), which is equal to half the difference between the temperatures of adjacent hot and cold bars. The reference-based techniques involve imaging of a uniform source with the FPA camera and quantifying any deviations from uniformity among the detector elements. The figures of merit used for reference-based techniques include the percent nonuniformity (%U), the CSNR, and the nonuniformity D* (simply the mean/SD of the D* per detector element); however, Mooney et al. stated that none of these parameters are fully satisfactory, in that non-uniformity and spatial noise vary unpredictably with changes in operating conditions, and that each parameter is specific to an individual detector – hence, the versatility of D* as a basis for comparisons among detectors is lost ³⁶.

An effort at approximating the impact of the unique characteristics of FPA detectors on quantitative chemical measurements was made by Snively et al. ²³. Essentially a reference-based technique, their measurements of a benzonitrile solution yielded a coefficient of variation (CV) for the pixel absorbance values within the image of ~16% or higher; increasing the number of co-added scans reduced the CV to ~12%, still a significant variation ²³. Other findings of this study include:

- Impact of diffuser on source intensity distribution of the FPA found to be minimal.
- Effect of increased scan co-additions on the overall SNR of the FPA was found not to result in the expected square root increase.
- Linear relationship between SNR and decreased spectral resolution (R² = 0.968).
- LOD (for benzonitrile) of 9 mol% (5 μm pathlength); linear range of 30 mol%.
- With further advancements in FPA technology, high quantitative fidelity would be quite feasible ^{19, 23}.

2.1.4. IR Spectroscopy for Quantitative Analysis

2.1.4.1. Condensed Phase Sampling

Many techniques exist for obtaining an IR spectrum from a wide variety of samples – indeed, this is one of the strengths of IR spectroscopy. Two prominent techniques for making such measurements on fluid samples are transmission and attenuated total reflectance (ATR). The basic principles behind each technique are important to understand when determining which will best suit a particular experimental design. It is recognized that there are various other possibilities for IR analyses (e.g. diffuse reflectance, photo-acoustic, emission) but these are generally not pertinent to the handling of fluid samples and hence may be disregarded for the purposes of this review.

2.1.4.2. Transmission Measurements

Transmission measurements on fluid samples require the use of optical windows made from an IR- transparent material. Lists of typically used window materials and their associated ranges of IR transmission are available in the literature ⁴² and from suppliers (e.g. ICL, PerkinElmer). The simplest means of preparing a sample for a transmission measurement is to place a drop of the liquid on one window and then 'sandwich' the sample by placing another window on top of the sample, thus creating a film thickness of approximately 10-20 µm, referred to as a 'capillary film'. Other means involve the use of sealed or demountable transmission cells, in which two optical windows are separated by a spacer, ranging in thickness from 10 μm to several millimetres, which effectively determines the cell path- length; the latter may be precisely measured by the interference fringe method or the Lambert law method, with the former being the more accurate of the two ⁴². In sealed cells, the two windows are held together by a metal frame containing two filling ports, which are aligned with two holes drilled into the upper window so that liquid sample may be 'loaded' into the cell by means of a syringe. Demountable cells are similar in concept to sealed cells, the only difference being that the former must be disassembled in order to "load' the sample. Given that the path-length of a demountable cell may thus change slightly from one sample to the next, the use of a sealed cell is preferable for precise quantitative work.

Generally, for pure liquids the more polar the liquid, the thinner the transmission-cell path-length should be. Though it is preferable to work with pure liquids, many analytical situations require that liquid samples be diluted with a solvent. This may be done in order to provide a reproducible environment for the analyte, to increase the transmittance of a strongly absorbing liquid component, or to decrease the viscosity of a particular liquid (e.g. highly viscous oils) 42. In the case of solutions, concentrations of solute are typically in the range of 5-10% (w/v), and as long as the solvent absorbance is not too strong, the solvent spectrum may be subtracted from the spectrum of the solution in the absorbance mode ⁴². Typical solvents include chloroform, carbon tetrachloride, carbon disulfide, hexane, iso-octane, acetone, dioxane, tetrahydrofuran, and water 42. A rather significant disadvantage of transmission measurements of liquid solutions is that common solvents absorb very strongly in the mid-IR region. Water in particular absorbs over broad ranges of the mid-IR spectrum (for a 10 µm cell around 650-930 cm⁻¹, 1580 - 1750 cm⁻¹, and 2930 - 3650 cm⁻¹) and requires a very short pathlength to avoid signal saturation - thus compromising experimental sensitivity. Ideally, the path-length should be as small as possible; however this introduces problems with experimental reproducibility due to path length variation, practicality of filling the cells, and interactions of solvent molecules with surface materials. Another consideration is the possibility of solvent-solute interactions that may modify the resultant spectra of the solute. Such associations will result in a frequency shift of the absorption bands of the associated polar components of the solute molecule.

2.1.5.3. ATR Measurements

The ATR technique is based on the attenuation of a totally internally reflected IR beam through its interaction with the sample. This technique is implemented by placing the sample in contact with an "IR transparent' internal reflectance element (IRE), through which the IR beam from the source undergoes total internal reflection (TIR) by impinging on the IRE at an angle from the normal that exceeds the critical angle, θ_c = arcsin(n_2/n_1), where n_1 and n_2 are the refractive indices of the IRE material and the sample, respectively. The crystalline substance comprising the IRE must be of a higher refractive index than the sample in order for TIR to occur. Various materials are used for ATR IREs, including: ZnSe (nr=2.4 at 1000 cm⁻¹), Ge (nr=4.0 at 1000 cm⁻¹), Si (nr=3.4 at

1000 cm⁻¹), GeAsSe (nr=2.5 at 1000 cm⁻¹, and diamond (nr=2.4 at 1000 cm⁻¹) ^{43, 44}. When the incident IR beam passes through the IRE and contacts the sample medium at an angle greater than the critical angle (thus satisfying the requirements for TIR), an evanescent wave is produced at the surface of the IRE. Evanescent, meaning "tends to vanish", refers to the property of this near-field standing wave to decay exponentially from its point of origin, with the distance at which the amplitude of the evanescent wave has decayed to 1/e of its initial amplitude being termed the depth of penetration. The latter is proportional to the wavelength and also depends on the refractive indices of the IRE material and the sample but is generally on the order of 0.5–5 μm. Within this minute distance, IR absorption by the sample will result in attenuation of the evanescent wave, and, the attenuated energy of the evanescent wave is then returned to the totally reflected IR beam, which then exits the IRE onto the detector element. The short penetration depth of the evanescent wave makes the ATR technique ideal for highly absorbing materials (e.g. water solutions) as well as surface and thin film measurements. When used with solid samples, the short penetration depth makes it essential to ensure that the sample is in direct contact with the IRE of the apparatus, which is often achieved with the use of a pressure device.

2.1.5.5. Calibration Methodologies & Analytical Figures of Merit

Agencies such as the Association of Official Analytical Chemists International (AOAC International) impose strict guidelines for the performance of calibrations applied to specific analytical problems, e.g. the proximate analysis of raw milk for fat, protein and lactose contents. Because FTIR spectroscopy is a secondary method, its results must be continually confirmed by a reference method, and there must be a defined level of agreement. A way to establish the level of agreement is defined as the mean difference for accuracy (MDa) and the standard deviation of the differences for accuracy (SDDa). The MDa measures the differences between measurements made on calibration standards using the reference method and the FTIR method and is reported with a sign to indicate both the magnitude and the direction of the bias of the FTIR method relative to the (presumed to be accurate) reference method. The SDDa measures the width of the distribution of those differences, giving an indication of the precision of the FTIR method relative to the reference method; it is noted that the SDDa is inherently limited

by the precision of the reference method 45 . An additional set of measurements describe the level of reproducibility of an FTIR method and are analogous to the MD_a and SDD_a parameters, replacing the reference method measurements with a set of repeated FTIR measurements. These parameters are reported as the mean difference for reproducibility (MD_r) and the standard deviation of the differences for reproducibility (SDD_r) .

Linear Regression

According to IUPAC "a calibration in analytical chemistry is the operation that determines the functional relationship between measured values and analytical quantities characterizing types of analytes and their amounts" 46 . The simplest of calibration models is a linear least-squares estimation (LLS); the relationship between signal intensity (y_i) and analyte concentration (x_i) in an LS model is expressed in equation 2.5.

Equation 2.5.
$$y_i = B + M x_i$$
 ($B = \text{Experimental Blank}$; $M = \text{Experimental Sensitivity}$)

In terms of spectroscopic analysis, the response (y_i) is the absorption of electromagnetic radiation at a specific wavelength by a quantity of analyte (x_i) . The Beer-Lambert-Bouguer law (or simply Beer's law) describes the relationship between the attenuation of a monochromatic beam of electromagnetic radiation of fixed radiant power on interaction with an absorbing medium 47 . When a number of requirements are satisfied 47 , a chemical system may be found to adhere to Beer's law, whereby the directly proportional relationship between analyte concentration and signal response is described by equation 2.6. When a linear model is made relating concentration to absorbance for prediction of concentration from absorbance, the calibration is referred to as an inverse Beer's law calibration 19 .

Equation 2.6.
$$A(\lambda) = a(\lambda)bc$$

(A=absorbance; λ = wavelength; a = absorptivity; b = path-length; c = analyte concentration).

Looking from equation 2.5 to equation 2.6, it is observed that the term M (in equation 2.5) in spectroscopy is in fact a combination of the measured path-length and molar absorptivity of the analyte – which will be different from one case to another.

Building a calibration is usually conducted in such a way that there is the upmost confidence in the true values of the calibration standards which should be prepared in suitably graduated amounts 46 . This creates a 'controlled' situation where the level of error associated with the x_i component becomes negligible when compared to the level of error in the y_i component (dependent variable) of the calibration, ensuring that the error introduced to the calibration model is as minimized as possible. Some descriptors of the quality of a particular calibration model include the correlation coefficient (CC), the calibration standard deviation (CSD), linearity (*a priori* or *a posteriori*), comparison of experimentally obtained calibration parameters (*B* & *M*) and the condition of *homoscedasticity* (where the standard deviation of the points around the curve is assumed to be equivalent along the length of the curve); see reference for elucidation and/or further descriptions of each of these parameters 46 .

Multiple Linear Regression

Multiple linear regressions (MLR) take into consideration that the correlation of y_i may not be solely with x_i but with x_n , where n could equal any number of explanatory variables. In other words, MLR attempts to model the relationship between 2 or more explanatory variables and a response variable by fitting a linear equation to an observed data set. In equation 2.7 an example of a two-predictor linear regression model is provided ⁴⁸.

Equation 2.7.
$$y_1 = \beta_0 + \beta_1 x_1 + \beta_2 x_2 + \epsilon$$

This model is linear in each of the parameters β_0 , β_1 , and β_2 , and describes a threedimensional plane with the axes y_1 , x_1 , and x_2 . The parameter β_0 is the intercept of the plane, while the parameters β_1 and β_2 are called the partial regression coefficients. Parameter β_1 represents the change in the response corresponding to a unit change in x_1 when x_2 is held constant, and vice versa for parameter β_2 .

Partial Least Squares Regression

Partial least squares regression (PLS) is a multiple linear regression technique that is said by some to be the *de facto* standard calibration method in spectroscopy ⁴⁹. PLS is

often referred to as a "whole spectrum" technique because the calibration model may be built utilizing the complete vector which represents the spectrum, as opposed to LR and MLR techniques which utilize single or relatively small portions of the overall spectra (e.g. peak heights and/or peak areas of interest). It is also referred to as an 'indirect method' in that it only requires knowledge of the concentration of the analyte(s) in question. In short, PLS involves the determination of a set of latent variables through a data matrix rotation which determines the components within the data matrix that are also relevant to the (in the case of chemical measurement) concentration values ¹⁹. The latent variables which are calculated describe the variability attributed to the data matrix and the concentration values; the first latent variable describes the largest source of the variability, the second latent variable the second largest source of variability, and so on. The selection of the number of latent variables to define the PLS calibration model is an important consideration, where the simplest and most commonly employed method is to utilize the latent variable associated with the minimum predictive error sum of squares (PRESS) value ¹⁹. In this procedure the PRESS values are plotted against an increasing number of latent variables and the minimum of this plot is then selected as the optimum condition of calibration.

A significant advantage of using PLS calibration models is that they are often robust enough to build calibrations for sample matrices that exhibit highly overlapped spectral features — i.e. it can prove to be quite trivial to build multi-component calibration models from complex sample matrices. Given the multiplexing advantage of FTIR spectroscopy, it does in some circumstances seem suitable to make use of that wealth of information, which is where PLS (among other multivariate matrix based techniques), is quite well suited.

2.1.4.5. Quantitative Applications of FTIR Spectroscopy in Food Analysis

FTIR spectroscopy is reliable (inherently high wavelength accuracy and reproducible measurements), fast (to various degrees, depending on interferometer/detector/method), often non-destructive to the sample, and simultaneously acquires a wealth of chemical information in a single measurement. It has been demonstrated that there are a variety of potential calibration schemes (most using matrix methods based on the additive nature of Beer's law) that can access this

chemical information to varying degrees, easily achieving multi-component calibrations from complex sample matrices ². All of these attributes make FTIR spectroscopy highly adaptable to process analysis applications; a sector which has seen significant levels of success in the application of FTIR spectroscopy is the food industry. The needs of the food industry lie mainly in proximate analysis, be it raw materials, process products, or finished products. The main constituents in foods are fats, proteins, carbohydrates, and moisture – followed by a list of minor constituents such as vitamins, minerals, phytosterols, organic acids etc. Of particular interest to this review are those applications which require quite high levels of sample throughput, and to give an impression of such requirements three applications will be highlighted: milk analysis, wine analysis, and edible oil analysis.

Milk Analysis

The dairy industry is a notable example of the successful application of IR spectroscopy for the regular proximate analysis of a food product. The modern application of FTIR spectroscopy to milk analysis is preceded by a significant background of IR utilization in the industry. The traditional chemical reference methods for compositional analysis of milk include the Babcock and Mojonnier ether extraction methods for fat, the Kjeldahl procedure for protein, and polarimetry or HPLC for lactose ⁵⁰. These methods carry a high degree of precision; however they are inefficient in terms of time of analysis and require substantial amounts of chemicals, particularly when performed on a large commercial/industrial scale. These issues motivated the search for a rapid analysis technique, and in 1960 the first IR milk analyzers were created by Goulden et al. ³; these were eventually commercialized as the IRMA by Grubb-Parsons. This analysis technique was accepted by the AOAC as an official method, and later the IRMA was purchased by FOSS - now a global leader in IR milk analyzer systems; see table 2.3 for a list of companies marketing dedicated IR milk analyzers. The adoption by industry of these IR milk analyzers resulted in their gradual evolution from diffraction grating based systems to filter based, and eventually interferometer based systems. The current utilization of FTIR spectrometers for the analysis of raw milk is illustrative of the high-throughput potential of the infrared analysis technique. Some of these analyzers (e.g. MilkoScan series from FOSS) utilize an automated flow system and are capable of scanning up to 600 samples/hour. Further, it is not uncommon for central laboratories to operate several of these units simultaneously, amounting to a potential of several thousand samples/hour. The incorporation of FTIR spectrometers into these instrument designs enables the simultaneous selection of appropriate spectral bands for the quantification of the main components of milk; carbonyl groups from the ester linkages of fats (C=O stretching vibration modes), peptide linkages (Amide II) in proteins, and O-H groups in lactose ⁵⁰. Current instrumentation/calibration techniques are capable of measuring the fat, protein, lactose, total solids, solids-non-fat, freezing point depression, total acidity, free fatty acids, density, urea, and casein values from a milk sample. Depending on the exact analyzer system being used, they are also adaptable to creams, concentrated milks, infant formulas, and an increasingly wide variety of milk products. Table 2.3 illustrates the potential versatility of FTIR analyzers in the dairy industry, highlighting several studies of dairy products. A list of several publications regarding FTIR analysis of dairy products is provided in table 2.4 (following page).

Company	<u>Product</u>
FOSS	MilkoScan™ FT+ (FTIR)
	MilkoScan™ FT2 (FTIR)
Delta Instruments	LactoScope FTIR Automatic
	LactoScope Filter C ₃ +/C ₄ +
Metron Instruments	Calais Milk Analyzer
	York Dairy Analyzer
Bruker Optics	MPA & Matrix FT-NIR
Unity Scientific	SpectraStar™ 2400 (NIR, grating)

Table 2.3. List of some commercially available IR based milk analyzers (2009).

Sample Set	Reference	Spectrometer/Calibration/Analytes/Other	
Milk Standards (12c)	Van de Voort et al	FTIR with MLR, CLS, and PLS calibration model, measures of fat/protein/lactose/TS.	
Milk Standards	Ulberth et al ⁵¹	FTIR, derived methyl ester + direct measures of TFA content	
Sweetened Condensed Milk Standards (20c, 30v)	Nathierdufour et al ⁵²	ATR-FTIR, PLS calibration model, measures of fat and solids.	
Milk Standards	DeJong et al ⁵³	FTIR, 2 nd Derivative measurements, measures of fat/protein/lactose.	
Raw Milk Standards (~300c, 20v)	Hewavitharana ⁵⁴	FTIR, PLS and PCR calibrations, measures of casein content	
Milk Standards (~900c, xv)	Hansen ⁵⁵	FTIR, Multivariate calibrations, various pre- treatments, measures of urea content	
Milk Standards (180c)	Heuer et al ⁵⁶	FTIR, PCA/PLS, truncation & 2 nd derivative pre-treatment, measures of acetone content	
Chocolate Milk Standards (18c, xv)	Cocciardi et al ⁵⁷	FTIR, PLS calibration, measures of fat, sucrose, lactose, and total solids.	
Milk Standards (45c, 15v)	Sivakesava et al ⁵⁸	FTIR, FT-NIR, PLS calibration, measures of tetracycline content	
Milk Standards (33c, 48v)	Inon et al ⁵⁹	ATR-FTIR, HCA selection, PLS-1 PLS-2 calibration; measures of fat, protein, carbohydrates, calcium, caloric content.	
Infant Powdered Milk (11 – qualitative)	Deng et al ⁶⁰	FTIR, 2nd derivative; measures of fat, protein, lactose, maltodextrin, sucrose.	
Spoiled Milk Samples (252)	Nicolaou et al ⁶¹	ATR-FTIR and HT-FTIR, PCA/ PLS calibrations, metabolic fingerprint measures.	
Rumen Standards (n/a)	Uden et al ⁶²	FTIR, measures of acetate, propionate, butyrate, 1mM accuracy.	

Table 2.4. FTIR analysis of milk – examples from the past 20 years. c = calibration set; v = validation set; CLS = Classical Least Squares; TFA = Trans-Fatty Acids; PCR/A = Principal Component Regression/Analysis; HT-FTIR = High-Throughput – FTIR.

Alcoholic Beverage Analysis

Alcoholic beverages can be defined as those beverages with an ethanol content of 60% (v/v) or less and can be divided into two main categories – distilled liquors (or spirits) and fermented liquors 63 . The first component that likely comes to mind when making measurements of alcoholic beverages is that of the ethanol content, an important measurement for both social and economical reasons, and something that is performed in producer, government and customs laboratories. As with milk, there are tedious time-consuming official methods for the analysis of the ethanol content of liquors. It is possible to make measurements of ethanol using FTIR spectroscopy in both the transmission and ATR modes, while measurements using NIR spectroscopy are also quite common. Regarding transmission measurements, as with milk measurements, the path-length must be kept smaller than 50 μ m in order to keep the water absorption under control. A constant issue with direct measurements of ethanol is that there is often strong interference from carbohydrate bands, resulting in a variety of innovative calibration approaches (see table 2.5, following page).

The analysis of wines is another excellent example of the high-throughput potential of FTIR spectroscopy, with commercially available dedicated wine analyzers receiving considerable attention from industry and research communities alike ⁴. Using multivariate calibration techniques, mainly PLS regression, it is possible to make quantitative measurements on upwards of 10 components (with varying degrees of accuracy) on a single sample of wine – a nice touch for an industry with such prestige. The main challenges in FTIR analysis of wines are: 1) the chemically similar profiles of wines, 2) interferences from dominating components (mainly ethanol and water), 3) outliers due to the high variability of wine samples, and 4) the restricted LOD afforded by FTIR spectroscopy ⁴. Table 2.5 highlights several studies using FTIR spectroscopy for the direct measurement of an alcoholic beverage, with some pre-treatment of the sample in some cases. The wide ranges of products that open themselves to multivariate analysis make alcoholic beverages an excellent candidate for FTIR quantitative analysis.

Other Food Products

The application of FTIR for food analysis is of course not limited to milk and wine; there exist a wealth of products that the versatile range of FTIR techniques can handle. Edible oils form another significant area of FTIR research (table 2.6, following page), where the analysis of fat composition, moisture content, FFA's, peroxide values, iodine values, among other parameters, has been achieved with excellent accuracy ⁶⁴. Fruit juices, cola drinks, energy drinks, and essentially any sugar solutions comprise another successful example. FTIR has firmly established itself in the food industry, where the number of applications continues to grow rapidly.

Sample Set	Reference	Description	
Wine (72c, xv)	Schindler et al ⁶⁵	FTIR (SI); PLS calibration; measures of	
	Schindler et al	sugars, alcohols, organic acids.	
Beer	Haberkorn et al ⁶⁶	FTIR (SI); measures of carbohydrates, in	
	riaberkorii et ai	situ monitoring of enzymatic reaction.	
Wine (72c, 77v)		ATR-FTIR; PLS calibrations; measures of	
Distilled Liquor (xc,	Cocciardi et al 67	alcohol (distilled liquors); measures of	
12v)		alcohol, TR sugars, TA, and pH (wines).	
Wine (150c, 45v)	Dixit et al ⁶⁸	ATR-FTIR, ANN & PLS calibrations;	
		measures of glycerol adulteration.	
Alcoholic Beverages	Gallignani et al ⁶³	FTIR, online LL EtOH extraction with	
		CHCl ₃ , LR calibration, measures EtOH.	
Wino (907c, vv)	Moreira et al ⁶⁹	FTIR, PLS calibration; measures of TA,	
Wine (897c, xv)		tartaric, malic, lactic, acetic, citric acids.	
Cider (51-147c, 25-47v)	Lobo et al ⁷⁰	ATR-FTIR, PLS calibration; measures of	
Cider (31-1470, 23-47V)	Lobo et ai	TA,VA, EtOH, specific gravity, pH, fructose.	
Wine phenolic extract (64c, 22v)	Fernandez et al ⁷¹	FTIR, SPE, PLS calibration, 2 nd	
		derivative; measures of tannins	
(040, 224)		(phenolic content).	
Spirit drinks & Beer		FTIR, PLS calibration; 9 components for	
$(535c \& 461c, v = 1/3^{rd})$	Lachenmeier et al ⁷²	beer, 7 components for spirits.	
of c)		beer, / components for spirits.	

Table 2.5. IR spectroscopic analysis of alcoholic beverages. SI = Sequential Injection; ANN = Artificial Neural Networks; TR = Total Reducing; TA = Total Acidity; VA = Volatile Acids; SPE = Solid Phase Extraction.

Application	Reference	Description
Virgin Olive Oil	Tena et al ⁷³	ATR; SWMLR calibrations; TFA, total polar
		compounds.
Edible Oils (synthetic)	Christy et al ⁷⁴	Reflectance; PLS calibration; FA
		determination.
Thermally Stressed Oils	Dubois et al ⁷⁵	PLS calibrations; aldehyde formation, and
		determination of anisidine value.
Fats and Oils	Ismail et al ⁷⁶	Transmission and ATR; LR calibration; FFA
		determination.

Table 2.6. FTIR analysis of edible oils. SWMLR = Stepwise MLR; FA = Fatty acid.

2.2. Micro-fluidics

The field of micro-fluidics, which deals with fluid properties and applications at the sub millimetre scale ($<10^{-3}$ m), is a highly multidisciplinary science encompassing the areas of engineering, physics, chemistry, micro-technology, and biotechnology to name a few. According to Tabeling and Cheng (2005), "Micro-fluidics can be defined as the study of flows that are simple or complex, mono- or multiphase, which are circulating in artificial micro-systems" ⁷⁷. Over the past two decades this field has been increasingly explored, evolving from its earliest applications in basic flow analysis procedures towards more involved applications like micro total analysis systems (μ TAS) and the 'lab on a chip'.

It is alleged that micro-fluidics was born of four parent technologies: molecular analysis, bio-defence, molecular biology, and microelectronics ^{78, 79}. Molecular analysis refers to the advancements in capillary analysis technologies such as high performance liquid chromatography (HPLC) and capillary electrophoresis (CE) – both highly employed analytical techniques whose successes encouraged the development of increasingly compact designs ⁷⁹. Secondly, fears of biological and/or chemical weapons technology stimulated the Defence Advanced Research Projects Agency (DARPA) to develop highly compact, field deployable micro-fluidic instrumentation for their detection ⁷⁸. These suspicions provided what some consider to be the main stimulus for academic advancements in micro-fluidics during the 1990's ^{78, 79}. The field of microbiology made major contributions to the development of micro-fluidics during the search for more efficient methods of DNA sequencing during the genomics boom of the 1980's;

techniques with higher throughput, sensitivity and resolution were essential for advancements in this research ^{78, 79}. Lastly, the field of microelectronics supplied a precedent for the fabrication of micro-fluidic devices (e.g. photolithography, wet/dry etching, deposition), which enabled the precise design of the channels and contours required for different micro-fluidic devices. Micro-electromechanical (MEM) devices provided the makings for various micro-components such as heaters, valves, and pumps that have since been adapted into novel micro-fluidic systems.

It is noteworthy that nature provides exquisite examples of micro-fluidic systems that make our current innovations seem crude at best. One example is the capillary systems found within trees, which employ networks of countless capillaries ranging in size from a hundred micrometers in the trunk to tens of nanometres within parts of the leaves. Despite the complexity of the capillary system, it is able to provide a near homogenous supply of sap throughout the organism – reminiscent of the circulatory and respiratory systems in animals ⁷⁷. Another example is the ability of any common spider to spin a thread 10's of micrometers in diameter with remarkable mechanical characteristics. This is accomplished through the synthesis of proteins having a specific combination of crystalline and amorphous structures that give the silk its extraordinary properties, which are then manipulated through a series of glands to be expelled as the final product ⁷⁷. Looking to examples such as these, one might consider the field of microfluidics to be open to biomimetics ^{78,80}.

The accomplishments of manmade micro-fluidic systems have yet to reach those seen in nature; however it is currently recognized as a young science with plenty of promise. The fact that micro-fluidic systems require minute sample/reagent volumes, generate respectively small volumes of waste, possess reaction/separation/detection times with high sensitivity and resolution, offer the possibility for integration and automation, have a high energy throughput, have reduced dimensions compared to conventional analytical instrumentation, and are relatively cheap – makes micro-fluidics quite an attractive technology ^{78, 79, 81, 82}. It is apparent, as indicated by the above list of qualities, that micro-fluidic technology derives most of its advantages from its relative size. The details of the behaviour of fluids at the micro scale shall now be discussed in more detail.

2.2.1. Micro-Fluid Theory

When thinking about micro-fluidics, it should be apparent that small fluid volume is the cornerstone of the technology. Columns typically range from 5-500 μ m in diameter, and fluid volumes range from micro- to femtoliters $(10^{-6}-10^{-15}\ L)^{-81}$. Micro-fluidic technologies take advantage of both the physical scale of a particular system, and the properties of fluid behaviour at that scale 79 . It may not be intuitive that liquids at the micro scale should behave differently than those in the macro-world, after all the micro scale is still several orders of magnitudes larger with respect to molecular and intermolecular distances. Still, there are situations where physical descriptions that may apply in the macro world prove unaccommodating at the micro-scale of fluids.

Some relevant works for introductory concepts to micro-fluidics include: Patrick Tabelings "Introduction to Micro-fluidics" ⁷⁷; Henry Bruus's "Theoretical Micro-fluidics" ⁸³; Nguyen and Werely's "Fundamentals and Applications of Micro-fluidics" ⁸⁴; and an assortment of journal articles and reviews ⁷⁹. In the following sections the characteristics of fluids and fluid flow, and transport mechanisms within micro-fluidic systems are considered in brief. It is suggested that if the reader would like a more in depth treatment of these concepts they refer to the listed material.

2.2.1.1 Fluids and Fluid Flow

Fluid: "A material that deforms continually under shear stress or with the application of an external force attempting to displace part or all of the fluid elements at a surface boundary."

The term fluid and liquid are often used synonymously, however this is not strictly correct as gasses and liquids (separate phases) both exhibit fluid characteristics. That said, there are fundamental differences between these two types of fluids as a consequence of their vastly different densities^{83, 84}. Three important parameters when considering fluids are: density (ρ), pressure (P), and viscosity (η). Density is defined as mass (m) per unit volume (V). Pressure is defined as the mechanical force per unit area of a surface. Pressure within a fluid is a function of the depth of the point of interest in the fluid, i.e. pressure will increase as you descend from the surface of a liquid. In terms of micrometers, the change in pressure (ΔP) is minute, allowing for the safe

approximation that pressure changes due to depth within microfluidic systems can be ignored. As will be discussed in section 2.2.1.2, external pressures are often applied to micro-systems containing inlets and outlets as a means of obtaining fluid flow. When a fluid flows within a confined area there will be resistance, giving rise to fluid viscosity. Viscosity can be defined by equation 2.8, which shows the viscosity coefficient equal to a ratio of shear stress (Force (F)/Area (A)) to shear rate (displacement (dx)/liquid thickness (dy)). Sheer stress refers to a stress force parallel to the face of a material, while sheer rate refers to the displacement of the film relative to the films thickness.

$$\eta = \frac{F/A}{dx/dy}$$

Equation 2.8. Viscosity Coefficient (ratio of sheer stress: sheer strain).

There are three possible scenarios surrounding the relationship presented in equation 2.8. The first is that the relationship between the viscosity coefficient and the sheer stress is directly proportional. Any fluid that exhibits this behaviour is classified a Newtonian fluid. The second and third possibilities involve situations where the two parameters are not directly proportional (i.e. the viscosity changes with the magnitude of sheer stress) and are called Non-Newtonian fluids. In the case of Non-Newtonian fluids the viscosity can either increase (sheer thickening) or decrease (sheer thinning) with the amount of sheer stress.

The main issue when going from macro to micro-fluidics has to do with the relative importance of various physical effects, a problem that may be simplified by using dimensionless parameters ⁸⁵. A dimensionless parameter is used to define a unit such as volume, length, or linear flow rate in such a way that it can be assumed to be constant throughout an entire system, a scaling technique used by engineers when there are large number of variables involved with a particular system ⁸⁶. A commonly quoted dimensionless parameter in regards to fluid flow properties is the Reynolds number (*Re*), defined in equation 2.9.

$$Re = \frac{\rho dv}{\eta}$$

Equation 2.9. Reynolds number (d=diameter or channel depth; v= average velocity of the moving liquid, and η = viscosity).

This dimensionless parameter describes the flow properties of a fluid as a ratio of inertial effects to viscous effects, i.e. in terms of turbulent or laminar flow $^{79, 85}$. Turbulent flow is characterized by the presence of eddies, vortices and other flow fluctuations, while laminar flow is characterized by a smooth, stable fluid motion 85 . Empirical observations estimate fluids with a Re of >2300 to be turbulent (inertial forces are dominant). With a Re of approximately <2000 a fluid begins to be dominated by laminar flow (viscous forces). In regards to equation 3.2 it is apparent that micro-scale channels will generate a low Re at practical velocities – in fact a flow rate approximately the speed of sound would be required to see inertial forces resurface 79 ! This has implications to how fluids will be able to mix within micro-fluidic channels, as without some form of agitation, mixing will be entirely diffusion controlled. It is recognized that due to the nature of fabrication techniques (section 2.2.1.3) micro-channel designs are often semi-rectangular, and as such the hydraulic diameter (equation 2.10) may be used in determining the Re. The wetted perimeter (P_{wet}) refers to the entire perimeter of the channel that is exposed to the fluid.

$$D_h = \frac{4A}{P_{wet}}$$

Equation 2.10. Hydraulic Diameter (D_h), Area (A), P_{wet} (wetted perimeter).

There are various dimensionless parameters related to surface tension that may be useful, depending on the particular micro-fluidic application ⁸⁵:

- Capillary number (Ca) compares viscous effects to surface tension effects useful when working with multiphase flow.
- Weber number (We) compares fluid inertia to surface tension useful for analysis of bubble/droplet formation.
- Bond number (Bo) compares gravitational effects to surface tension effects minor effect observed in gas-liquid systems.

Navier-Stokes equations are based on combinations of fundamental laws (conservation of mass/energy/momentum) with fluid properties (viscosity, thermal conductivity etc.), and are used for the theoretical treatment of fluid flow. These equations require several boundary conditions or equations of state in order to obtain

meaningful solutions. A key boundary condition is that of the 'no slip condition', which states that the velocities found at a phase boundary must be equal. In the case of phase boundary between a fluid and solid capillary or channel, the velocity must then be equal to zero. Another boundary condition is the 'no temperature jump' condition – used to ensure that a gradual temperature gradient is in place for data treatment ⁸³.

The Poiseuille flow equation (equation 2.11) presents a solution to the Navier-Stokes equations that is useful for describing flow conditions in a system with a pressure gradient as the driving force 79,83 . Within equation 3.4 exists the reciprocal of the fluidic resistance, $8\eta L/\pi R^4$; its inverse dependence on the capillary radius demonstrates an increased fluid resistance with decreased size. As a result of the increased resistance the required pressure gradient (ΔP) needed to flow liquids through dimensions at the microscale is quite large. Currently there is no known analytical solution to the Poiseuille flow problem when presented with rectangular channel dimensions – it is instead approximated as a Fourier sum with reasonable accuracy 83 .

$$Q = \frac{\Delta V}{t} = \frac{\pi R^4}{8\eta L} \Delta P$$

Equation 2.11. Poiseuille Equation (Q): (R = capillary radius, L = capillary length, ΔP = hydraulic pressure, ΔV = volume of liquid in system, t = time).

2.2.1.2. Transport Mechanisms

A key function of many micro-fluidic devices is that they have a fluid (or some combination of fluids) flow through a simple or complex network of micro-channels for some purpose. There are two different types of transport in micro-fluidic systems: directed transport and statistical transport ⁷⁹. Directed transport is achieved through the application of work to the system. Two common means of achieving directed transport in micro-fluidic systems are pressure driven flow and electro-osmotic driven flow ^{87, 88}. Statistical transport is defined as entropy driven transport, whereby flow only occurs when the fluid is moving in such a way that it is more disordered than its initial state (e.g. diffusion controlled transport). Mixed transport (a combination of directed and statistical transport) is also a possibility, an example is forced heat convection – the fluid is pressure driven through the channel while a heat source causes the molecules in

contact with the channel walls to diffuse to the center ⁷⁹. Due to the high ratio of surface area to volume in micro-channels there are many interfacial phenomena that could be explored as driving forces e.g. wetting properties, surface tension, capillary effects, electrokinetics ⁸⁹. For the purposes of this review only electro-osmotic and pressure driven directed transport are discussed further.

Electrokinectic Drive (Electro-osmotic Flow): Electro-osmosis is the electrokinetic flow of fluids with respect to a fixed, charged solid surface ^{90, 91}. Note that the key difference between electro-osmosis and electrophoresis lies in the size of the charged particles in the ionic liquid; if comparable to the size of the fluid molecules you are dealing with electro-osmosis, whereas if the particles are large (e.g. macromolecules, proteins) you are dealing with electrophoresis ⁹². The flow phenomena observed in these systems is dependent on the applied electric field, the physical characteristics of the microchannels, and the physical properties of the fluid ⁹³. The principles behind electro-osmosis (and electrokinetics) can be explained with a model case ^{77,89}:

- Establish a uniform surface charge at a solid-liquid interface within a capillary or channel, brought about by the functional groups of the surface material.
- Surface charge attracts counter ions from the contained electrolyte solution.
- An excess charge is developed near the solid-liquid interface, forming an electrical double layer (EDL) with thickness equal to the Debye screening length.
- This EDL of counter-ions screens the electric field so that it decays over the Debye length – the potential drop over this distance is referred to as the zeta potential (typically less than 100 mV for electrolyte solutions).
- Application of an external electric field parallel to the capillary/channel produces an
 electrical force within the EDL, driving the mobile ions within.
- Fluid surrounding the ions moves due to fluid viscosity, bulk fluid motion is produced.

Note: The EDL results in a screened electric field normal to the surface whose strength depends on surface charge density, thickness ranges from \sim 10-100 nm relative to electrolyte concentration (\sim 10⁻³ – 10⁻⁵ M) ⁸⁹.

When an ion containing fluid (e.g. water) is placed into a micro-channel with a fixed charge on its surface and the voltage is applied, the fluid will essentially move as a plug ⁷⁸. There are several advantages to electro-osmotic driven flow as it relates to micro-

fluidics, e.g. the simplicity of having the driving force embedded into the device, no external moving parts, convenient power supplies (batteries), compact size, minimization of fluid plug broadening, and the high resolution separation of ionic components ^{78,89}. However, depending on the specific application you are interested in there are some drawbacks to electro-osmosis directed transport, especially related to the strong dependence of electro-osmosis flow on the channel surface properties. For instance electro-osmotic flow can result in varied amounts of analyte retention, impacting the efficiency and reproducibility of chromatographic separations; the coatings sometimes added to micro-channels used for cell analysis can lower the net surface charge of the channel, thus suppressing the flow rate; limited flow rate for time resolved applications; the presence of an electric field may be undesirable in some cases – i.e. unwanted electorphoretic separation, alteration of biological cells ⁸⁷. Another limitation of electro-osmosis is that it is only applicable to polar fluids containing some concentration of ions ⁹².

Pressure Drives (Hydrodynamic Flow): This is a conventional method of achieving flow in fluid systems, something that has been well established by engineers. Flow in this case is driven by the action of a pressure difference, which is applied between an upstream and a downstream terminal in a device. Applied pressures spread right through the fluid with finite speed, though changes do not occur everywhere throughout the fluid instantaneously as they are limited by the speed of sound ⁹². The actual transfer of pressure in a fluid is carried out at the molecular level through intermolecular forces and momentum gain through increased molecular collisions (more significant in the case of gasses). The usual means of obtaining a pressure differential in microfluidic systems is by connecting an external macro syringe pump with the excess of fluid to be injected into the micro-channel. This system gives good control over the pressure differential; however it can prove problematic to obtain highly accurate control of the fluid flow ⁸⁷.

The use of microfluidic pumps has been investigated, with over 200 journal articles covering new micro-pumps or analyzing micro-pump operation since the early 1980's ⁹⁴. There exists a wide range of mechanical and non-mechanical pumps available to microfluidics, e.g. check-valve, peristaltic, valveless rectification, rotary, ultrasonic, centrifugal, magneto-hydrodynamic, electro-hydrodynamic, and as discussed previously electro-

osmotic ^{88, 94}. The majority of micro-pumps reported are classified as reciprocating displacement pumps, otherwise known as membrane or diaphragm pumps ⁹⁴.

An issue with micro-fluidics and pressure driven flow is found within the Poiseuille flow equation (equation 3.4) – the fluidic resistance. The high surface to volume ratio creates viscous effects that require a larger pressure gradient (typical operating pressures in microfluidic systems are between 1 kPa and 100 kPa) in order to provide the flow needed for the system – perhaps to the point of compromising the mechanical integrity of the device ⁹². Another problem with micro-mechanical pumps is that their fabrication and implementation into microfluidic devices can prove to be quite tedious – as opposed those of electro-osmotic systems. These disadvantages aside, the use of mechanical pumps continues to be a common means for pressure driven flow. The availability and cost of equipment such as syringe pumps, combined with its ability to move a broader range of materials, and its insensitivity to channel materials make pressure driven flow a practical approach for many applications.

2.2.1.3. Fabrication Technologies

Fabrication technology for microfluidic devices has evolved largely out of techniques developed in the field of micro-electromechanical (MEM) engineering where techniques such as photolithography, etching, deposition, micro-wetting, and micro-impression all permit the fabrication of miniaturized systems ⁷⁷. As a convention these technologies can be categorized into *hard* and *soft* techniques; hard referring to technologies based on etching/lithography/deposition of hard materials such as glass and silicon, soft referring to technologies that manipulate elastomers or plastic materials.

An important consideration with respect to the current work is that the majority of micro-fabrication techniques have been built up around MEM's technologies, where it is most common to work with silicon and glass based media. When working with IR detection these techniques must be extended to different IR transparent crystal media, e.g. CaF₂ or ZnSe, where fabrication techniques are less developed. Besides being considerably more expensive than the more common glass/silicon substrates typically used, there are other differences in these IR transparent substrates that will have consequences on the application of micro-fabrication techniques. Keeping this fact in

mind a brief description of common micro-fabrication techniques is provided and, where possible, applications of the technique to IR specific materials.

Hard Techniques - Etching

As previously mentioned, the use of silicon or glass as a substrate in micro-design is a relatively mature technology. These hard materials are open to techniques such as etching, lithography, and deposition, which are capable of obtaining micro-channel dimensions in the range of $0.2-500~\mu m^{-77}$. Silicon as a micro-device substrate is suitable for various reasons: wide availability, possibility for integration with electronic circuits (semi-conductor), and its physical and chemical properties make it compatible with a wide range of established micro-fabrication processes with sub-micrometric precision. Glass, for the most part, can be thought of as analogous to silicon in respect to the micro-fabrication techniques discussed here.

One of the principle methods is the wet etching of silicon/glass. This involves protecting some portion of the substrate with a mask while it is exposed to a liquid phase chemical attack – a technique that can be traced back to the 15th century for the creation of designs in armour ⁷⁷. Isotropic and anisotropic etchings are two classes of etching with important differences. Isotropic etching creates spherical cavities, as the chemical reaction takes place equally in the three spatial dimensions. Due to its 'underetching effect' isotropic etching is less useful in designing lateral structures ⁸⁴. Anisotropic etching can be carried out along one plane, making it possible to design flat surfaces, and cavities. Isotropic etching is carried out using an acid called HNA (mix of HF/HNO₃/CH₃COOH), while anisotropic etching uses a strongly basic solution. The overall advantages of wet etching techniques can be summarized as: high selectivity, availability of planar or curved surfaces, high repeatability, and controllable etching rate with 'etchant' concentration ⁸⁴. With respect to IR transparent materials, it has been demonstrated that CaF₂ can be etched using laser induced heating.

Dry etching is another 'hard' technique, whereby a solid-state surface is etched in the gas phase, physically by ion bombardment, chemically through a reactive surface species, or through some combination of physical and chemical mechanisms ⁹⁵. Drawbacks of physical dry etching include slow etching rates, low selectivity (due to ions attack on all materials), and a 'trench effect' caused by reflected ions [8]. The chemical

dry etching technique is an isotropic technique that exhibits behaviour quite similar to its wet etching equivalents ^{84, 95}. An important physical-chemical dry etching technique called reactive ion etching (RIE) combines low pressures, radio frequency heating, and the bombardment of ions ^{77, 84}. This technique is quite important to the micro-machining industry, and variations of it are capable of achieving relatively high aspect ratios (e.g. deep reactive ion etching, DRIE). Other physical–chemical techniques include anodic plasma etching (APE), magnetically enhanced reactive ion etching (MERIE), triode reactive ion etching (TRIE), and transmission coupled plasma etching (TCPE). In general dry etching techniques yield finer patterns than wet etching, and provide the advantage of greater safety - as there is no need for corrosive acids or bases ⁹⁵.

Soft Techniques – Photolithography

Photolithography is an important micro-fabrication technique which involves the projection of light (typically between 300-450 nm for optical lithography) through a mask which is designed to protect specific parts of a photosensitive resist that has been deposited onto a substrate 77. The masks themselves are generally constructed from quartz with deposits of chrome to form the protected pattern translated onto the photosensitive resist. A polymer resin is deposited onto the substrate (e.g. glass, silicon, CaF₂) where it is then spin-coated (centrifugally spread and evaporated simultaneously). The thickness of the polymer film is proportional to the initial concentration of the polymer in solution and the viscosity of that solution, while it is inversely proportional to the angular rotational velocity ⁷⁷. The polymer cannot be deposited on too thickly, due to loss in precision of the patterns etched into it through the mask - thus thinner deposits are often used. After spin-coating, the remaining film is heated to ensure the removal of remaining solvent from the solution, which may otherwise lead to cracks upon drying. The final step is referred to as exposure, where the substrate with polymer are aligned and exposed to a luminous flux (e.g. mercury vapour lamp) which starts the physic-chemical reactions that attenuate the solubility in certain solvents ⁷⁷. Positive resists refer to polymers whose lighted zones become soluble in a certain solvent, while the unexposed – or dark zones remain insoluble and vice versa for negative resists.

2.2.1.4. FTIR for Detection in Micro-fluidic Systems

It has been put forward by some that FPA-FTIR spectroscopy is the most powerful spatial/chemical analysis tool of its kind, and that the inherently high throughput nature of the technique would make it tremendously adaptable to micro-fluidic systems ⁹⁶. The coupling of FTIR for flow injection analysis (FIA) and liquid chromatography (LC) applications has been described as an established yet relatively unexploited technique⁹⁷, 98; the principles of FIA/LC-FTIR could be enhanced further with micro-fluidic sampling accessories and FTIRI detection. It has also been observed that with more and more fluidic functions becoming available in microchip format, the necessity for high performance detection has never been more relevant 99. FTIRI is well suited to microfluidic detection for a variety of reasons: 1) the ability to rapidly collect spatially resolved chemical images, 2) the multiplexing capabilities of FTIR allow for rapid multicomponent qualitative/quantitative analysis, 3) the micro-fluidic platform can be fabricated directly onto an IR transparent material, and 4) the scale of micro-fluidic systems (path-length) are often well suited for mid-IR transmission measurements while ATR accessories allow for a range of other possible arrangements. The combination of the two technologies is also advantageous for sampling purposes in that there exists the potential for enhanced repeatability and accuracy, there is containment of chemicals within a closed system (important for toxic/volatile analytes), there is minimized reagent consumption and waste generation, and the whole system is highly adaptable to automated high-throughput analysis.

The number of papers using FTIR for high-throughput analysis is growing, as the performance capabilities of FPA detectors improve – now in their third generation of development (section 2.1.4.2). Snivelly et al developed a high-throughput parallel analysis platform using a Nicolet Magna 860 FTIR spectrometer equipped with wide band-pass filter, KBr diffuser, and a 64 × 64 MCT FPA, combined with a novel gas-phase sampling accessory ¹⁰⁰. The accessory, which arranged a series of stainless steel channels each with IR transparent windows (n=16) arranged in an array fashion, enabled the rapid parallel identification of CO oxidation over a series of commercial catalysts, while also allowing the quantification of reactivity and selectivity of these catalysts for the substrate. Kazarian et al have produced a number of applications utilizing an ATR-FPA-

FTIR spectrometer $^{96,\ 101-105}$. In their paper on chemical imaging of micro-fluidic flows, Chan et al 105 used a Varian 7000 FTIR spectrometer with a 64 x 64 FPA and a single bounce inverted ZnSe ATR sampling accessory to monitor the H/D exchange of H_2O/D_2O mixtures. Their sampling accessory involved a PDMS micro-channel self adhered to the ATR crystal, and fastened by screwing a plate of polymethyl methacrylate on to the top side of the structure. This system allowed for the separate introduction of two fluids which united at a 90° angle, then the 1000 μ m wide and 50 μ m deep channels snaked over the field of view for detection. From this system it was concluded that the in situ monitoring of chemical reactions and fluid mixing is possible.

Other work by Kazarian *et al* using the same instrumental system, explored different micro-fluidic structures using the same adhesion technique ⁹⁶: 1) a PDMS multi-well grid to monitor up to 156 samples simultaneously (figure 2.10c), and 2) a 4 parallel multi-channel system for monitoring the dissolution of different polymer formulations (figure 2.10d). Another approach by Kazarian et al ¹⁰⁶, and also Kirkwood et al ¹⁰⁷ for applications in pharmaceutical and bacteria identification purposes respectively, was to employ a micro-drop deposition technique (figures 2.10a and 2.10c respectively). In this approach the samples are uniformly 'stamped' onto an IR transparent substrate in an array format enabling the simultaneous measurement of many micro-drops of sample. Theoretically this technique would allow for the measurement of as many samples as there are detector elements of the FPA, e.g. 1024 samples for a 32 x 32 FPA; although practical considerations make this a purely boastful claim.

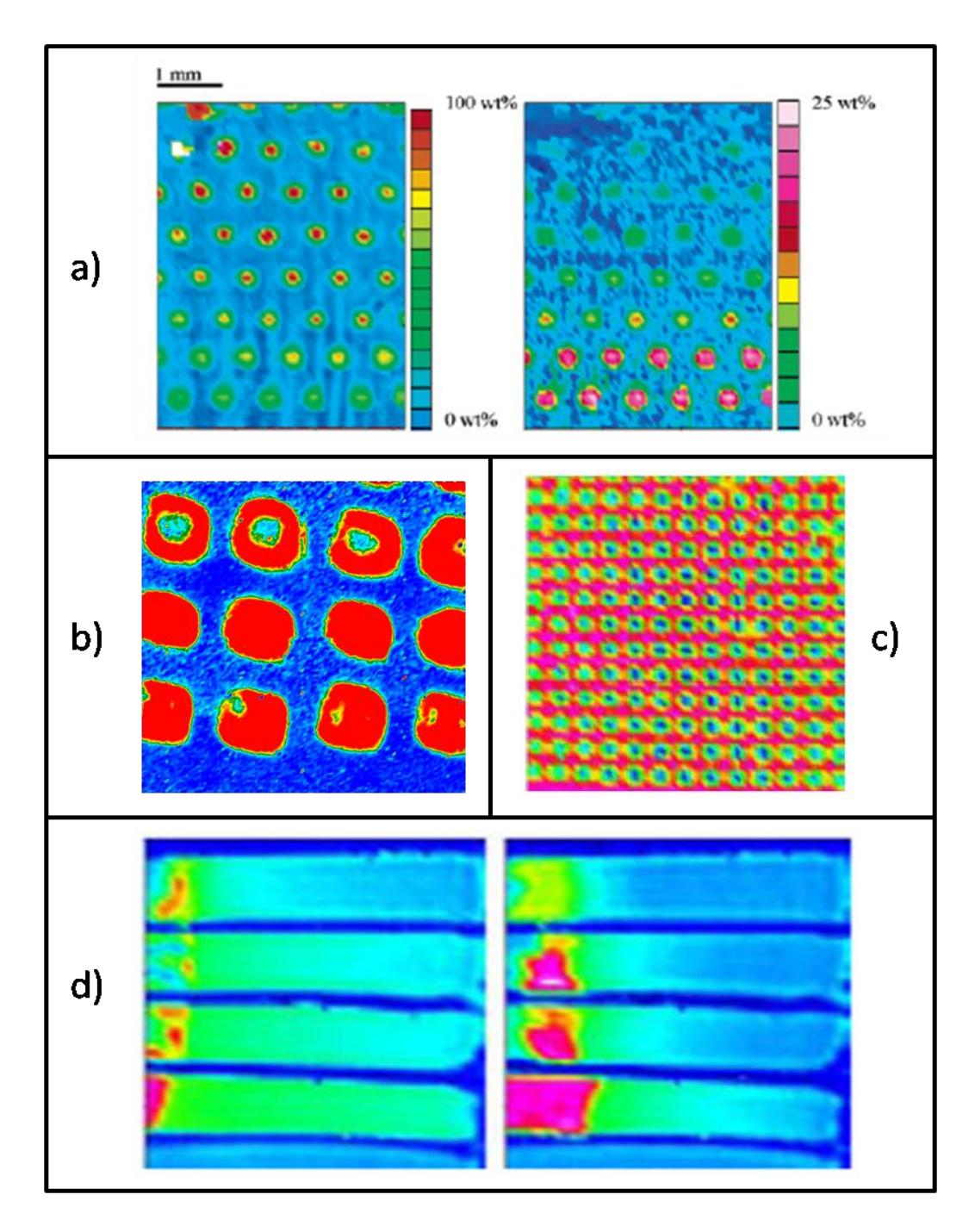


Figure 2.10. Examples of HT-FPA-FTIRI studies: a) micro-droplets of poly(ethylene glycol)/ibuprofen formulations 106 ; b) micro-depositions of bacteria culture 107 ; c) PDMS multi-well demountable grid 96 ; d) 4 micro-fluidic channels for monitoring of polymer dissolution 96 .

The technique of time resolved (TR) spectroscopy has seen some success of applying FTIR spectroscopic techniques to measuring micro-fluidic systems. TR-FTIR has proven to be a useful tool for obtaining structural information on the course of dynamic chemical processes - for example, enabling insight into reaction kinetics, ligand interactions, protein conformational changes, complex formation ¹⁰⁸. There are a number of papers utilizing FTIR microscopic detection of micro-channel systems designed to control chemical interactions. Hinsman et al 109 conducted work on a a fast diffusion based mixer (SU-8 polymer on CaF₂, ribbed mixer design) for the study of chemical reactions (three models: acid-base neutralization, addition of sulphite to formaldehyde, basic hydrolysis of methyl monochloroacetate). The apparatus proved to be very resistant to mechanical forces and chemical solvents, while their stopped flow liquid handling system was able to achieve highly reproducible. Kakuta et al 110 used a continuous flow and stopped flow TR-FTIR apparatus to achieve a time resolution of 0.5 - 10s in the observation of conformational changes in the protein ubiquitin, results of which were in good agreement with NMR spectroscopic measurements of the same system. The micro-machined mixer was off-chip in this study; solutions were first introduced into the diffusion based mixer then travelled onto the transmission cell for detection. This same approach was used by Masuch and Moss 111 to perform measurements of aqueous solutions of biological macromolecules (cytochrome c), where they provide a good overview of the optimization of experimental parameters. The time resolution of Masuch et al work was improved by Tang et al 112 to 6-15 ms (characterized by the reduction rate of 2, 6-Dichlorophenolindophenol), using a tuneable single frequency diode laser with MCT detector. This higher time resolution apparatus was also applied to the analysis of cytochrome c.

Kuan et al developed one of the first continuous flow systems using FTIRI for detection, using the addition of sodium sulphite to formaldehyde as a model system. Using the technique of multivariate curve resolution-alternating least squares to model the evolving chemical system they found that achievable time resolution was within the sub-millilitre range, but commented that the SNR achievable with the FPA hindered its application to more demanding systems ¹⁰⁸. It was also emphasized that the time resolution interpretation must consider the mixing time/mechanism, and the laminar flow conditions of the micro-fluidic system. The ability to simultaneously monitor

multiple fluid elements within the stream, together with the mixer being incorporated onto the sampling cell allows for the minimization of sample consumption with a maximum amount of data retrieval ¹⁰⁸.

2.2.1.5. Other Micro-fluidic Detection Techniques

Developments in micro-fluidic fabrication techniques in recent years have opened up a range of application possibilities, thus the demand for highly sensitive detection mechanisms to extract information from these systems has never been greater. It has been observed that the success of micro-fluidics is dependent on the abilities of researchers and engineers to develop detection processes various reviews cover a number of possibilities for detection of micro-fluidic systems ^{99, 113-115}. Optical detection methods are by far the most commonly found in micro-fluidic analytical devices, while electrochemical methods are becoming increasingly important, and mass analyzers comprise the third most significant level of attention in research. Mass analyzers in particular are significant in that fast and highly parallel separations in tandem with mass analyzers enable a very high-throughput potential ^{99, 115}. Optical methods are attractive due to their availability and the ease of coupling the micro-fluidic system with the detector type, while electrochemical methods are favoured for their good limits of detection for analytes of biological interest, and adaptability to integration within a microchip¹¹⁵. Other possibilities include:

- Fluorescence detection; very sensitive, but requires labelling for non-fluorescent analytes ¹⁰⁵.
- Raman spectroscopy; label free, not as sensitive as fluorescence ¹⁰⁵.
- Surface Enhanced Raman Scattering Detection (SERS); real-time, label free, very sensitive ¹⁰⁵.
- Thermal lens spectrometry (TLS); extreme sensitivity, very sensitive alignment ⁹⁹.
- NMR planar micro-coils; readily coupled to microstructures, modest sensitivity ¹¹⁴.

SERS and TLS are among the most popular 'up and comers' in micro-fluidic detection due to their universal response and no requirement for the chemical treatment of samples ¹¹⁴.

2.3. Conclusions

FTIR spectroscopy is an information rich spectroscopic technique, often described as a multiplexing approach due to its ability to simultaneously obtain measurements of all resolution elements. When combined with chemometric calibration techniques this wealth of spectral information can be exploited to extract qualitative and quantitative information of a sample. The application of FTIR spectroscopy to process analysis in industry has found good levels of success, with numerous dedicated analyzers available on the market for high-throughput analysis purposes. Therefore there is a present market for high-throughput infrared spectroscopic techniques, and one might assume that this market is looking to grow further.

The introduction of FPA-FTIRI has evolved FTIR spectroscopy into another level. The technique maintains all of the advantages present with conventional FTIR spectroscopy with the added benefit of spatially resolved chemical information of a sample. This level of information may exploited in a number of ways, 2D spatial characterizations of samples, using the high levels of data redundancy to ensure the selection of quality data from 'homogenous' samples, or using the spatial resolution abilities of the multiple detector elements composing the FPA to make parallel measurements. This last possibility, which has just begun to be realized, has exciting implications to the field of high-throughput vibrational spectroscopy.

The problems with the early developments of FPA detectors have been improved upon with the advent of 2nd and 3rd generation models; however there still remains the question of detector element fidelity, which relates to the relative spectral quality/consistency of the IR picture elements. When looking to applications such as high-throughput micro-fluidic flow analysis and time resolved analysis, the relative response sensitivity of individual detector elements is put to the test. If individual pixels are biased in any way relative to one another, it will limit the ability to make inter-pixel measurements within an image. It is in the context of the high-throughput flow analysis system that the performance characteristics of the FPA-FTIR on hand with our group will be put to the test. Pixel element noise performance, consistency of response, linearity will be evaluated in the short and long term, and in order to justify the added expense of the FPA detector the efficiency of such a system will be compared to a simpler approach to illustrate the potential gains in throughput.

Chapter 3: FPA-FTIR Spectrometer Evaluation

3.1. Introduction

FPA-FTIRI involves the collection of spatially resolved chemical images of samples, allowing for full spectral measurements from each of the pixels of the resultant image. Typical formats of the FPA detectors used in FTIRI spectrometers are measured as row x column (r x c) range from 32x32 to 256x256, while much greater sizes are available for astronomic applications (e.g. 2056 x 2056). In the case of the 32 x 32 FPA, as has been utilized in this study, there are then 1024 individual spatial points of data within a single image. From each point, depending on the spectral resolution parameters of the collected image, there exists a full IR spectrum worth of data (e.g. 387.5 points for 8cm⁻¹ resolution). A number of studies have focused on the imaging of heterogeneous samples on the micron scale, ranging from the characterization of imitation cheeses ⁵, identification of trace materials on latent fingerprints 116, selection of homogenous regions of bacterial depositions ¹⁰⁷, or the modelling of dispersions of pharmaceutical formulations in aqueous solutions ¹¹⁷. This last application begins to bleed over into another type of important imaging application, TR-FTIRI spectroscopy 118, whereby the individual response and sensitivity of detector elements can become quite important for interpretation of dynamic chemical processes taking place in the field of view of the FPA detector. A limited number of papers are found tying TR spectroscopy with an imaging detector, while those that have found that the SNR capabilities of such detectors limited the success for interpretation of complex spectra ¹⁰⁸.

The question of the analytical performance characteristics of FPA detectors, while presumed to be poor relative compared to conventional IR detection techniques, have not been fully addressed. A number of papers throughout the 1990's conducted performance characterization studies of FPA detectors, largely in the context of thermal imaging applications and the refurbishing of patterned noise features ^{23, 33, 35, 36}. Of particular importance is the issue of FPA detector non-uniformity, where due to a variety of reasons (see section 2.1.3.2), there will appear a characteristic pattern of response. There are a number of approaches (NUC) for the minimization of these spatial features, however a trace of spatial noise is always observed to persist. Snivelly et al ²³ were one of the few to make interpretations of an FPA-FTIR's detector element

response to a chemically homogenous sample (benzonitrile – CN stretching peak at 2229 cm⁻¹) where it was observed that, depending on the level of scan co-addition, the CV for the peak across the FPA could range from approximately 13.75% - 17.5%, for a post NUC FPA reading. Recent work within the McGill IR group ¹⁹ has found that this level of variance is consistent for several FPA detectors (3), and the trend translates into the analytical performance for the detector elements as a whole. Despite the noise response patterns and the low SNR performance of these FPA detectors, they were still able to obtain linear calibrations with milli-absorbance accuracy, where the performance improved through averaging and the use of noise cut-offs to eliminate noisier pixels ¹⁹.

The current study proposes an in depth investigation into the response characteristics of a continuous scan FPA-FTIRI system, in the context of making chemical measurements. Three basic model systems will be considered; 1) the open-beam response characteristics, 2) the repeated analysis of a stationary polystyrene calibration standard, and 3) the analysis of a set of aqueous calibration standards. From the openbeam data a thorough description of the noise characteristics of the FPA as a whole and the individual detector elements will be provided, allowing for optimization of scanning conditions for further data collection. The polystyrene study will provide information on the stability of measurements in the case of back to back scans, as well as day to day analysis. Also, as previous work has demonstrated that certain peaks will tend to provide less variant measurement than others ¹⁹, an investigation into the stability of different peaks will performed as validation of this phenomenon. The third case of the aqueous standards of sodium azide will provide additional validation to the polystyrene work, and also allow for optimization of collection of samples from transmission flow cells. For each circumstance above, a full characterization will be provided as well as the establishment of appropriate 'pixel filtration' procedures to select for the most relevant data for quantitative analysis purposes.

3.2. Experimental

3.2.1. Materials

A freshly purchased polystyrene calibration film (ICL, PhEur 2.2.24) was used for the collection of polystyrene spectra. Sodium azide (NaN $_3$) from Aldrich Chemical Company was used to gravimetrically prepare a set of 10 aqueous standards, ranging from approximately 0.0500-0.2000 M. Each standard was prepared with an analytical balance, directly weighing samples into a 100 mL volumetric flask, and were then diluted with 0.45 μ m filtered and distilled water, sealed, and thoroughly mixed. Samples were stored at room temperature in dark amber glass wear, with Teflon screw caps, for no longer than 5 days.

3.2.2.Instrumentation

The spectrometer used throughout the work was a Varian FTS 3000MX Excalibur FTIR spectrometer, fitted with a Varian 600 UMA microscope and Lancer FPA camera (32 x 32) - an MCT photovoltaic hybrid array detector. The optics of the microscope include a 4X and 15X objective, the 15X being the only FPA operative objective collection. The achievable spatial resolution of an individual detector element after projection of the sample through the microscope optics equated to $5.6 \ \mu m^2$; this measurement could be established through the inset microscope scale to ensure sample homogeneity in the FPA field of view.

3.2.3. Sample Acquisition

Data were acquired with various scanning conditions, the results of which are to be utilized for further analysis decisions. Ranges of spectral resolution were from 4-16 cm⁻¹, while scan co-additions ranged from a single scan to 1024 scan co-additions. The integration energy at the FPA detector was also adjusted for optimization purposes, although based on preliminary work it was often adjusted to an open beam integration energy value of ~9000 counts, see results for further validation of this value. The procedure for focusing the microscope optics was as follows: 1) place object firmly into position on stage and obtain optical focus using the visual objectives (as opposed to the in-microscope camera as there were almost always variations between the two focuses), 2) remove the sample from the stage and enter into the FPA non-uniformity correction Lancer window, 3) adjust the substage condenser so that the spread of data points viewed in the Lancer calibration

screen formed the highest 'rested' maxima with as even a possible distribution of the source energy over the FPA prior NUC, 4) establish the integration time so that integration energy sits at the decided value (again, typically 9000, unless otherwise specified), 5) perform NUC correction with open-stage, 6) replace sample and ensure that optical focus is still optimal, while also ensuring that no visible defects within the sample are present in the field of view. A slight alteration was made for the transmission cell/NaN₃ data collection; the focus was obtained on a bubble within the sampling transmission cell which was subsequently flushed with background solvent (water) within the microscope field of view, whereby - contrary to the open-stage and polystyrene work - the sub-stage adjustment, integration energy adjustments, and NUC were performed directly through the solvent filled transmission cell – see results for validation of this procedure. The loading of the transmission cell was done by manual injection using sterile syringes and thin gauge tubing, with stop-cock valves on the input and output sides of the transmission cell to ensure that a stopped flow was quickly obtained for scanning. Temperature control was obtained using two cartridge heaters and thermocouple linked to an Omega (CSi32 Series) temperature controller, whereby stabilization to within +/-0.1 C was guickly and easily achieved for consistent fluid measurements.

3.2.4. Data Processing & Analysis

All FTIRI data was collected via Resolutions Pro 4.0 with the dat. files (image files) subsequently exported to the in house software package ImageProcessor for further processing and imaging purposes. The color mapping of the software was set to build images on a 16 bit scale (dark red = high; dark blue = low), allowing for quick visual interpretation of results. This software also enabled the manipulation and exportation of data from desired coordinates of the image(s), and facilitated the viewing of the spatial impacts of filtering, derivative spectra, baseline correction and other standard spectral transformations. Exported FPA response was categorized as pixel ID paired with a measurement (decided and processed in the ImageProcessor suite), which were then easily manipulated in spreadsheet formats. Raw and processed pixel responses were exported to either Excel 2007 or Origins 7.0 for further statistical analysis and/or the creation of complementary graphics.

3.3 Results & Discussion

3.3.1. FPA-FTIR spectrometer noise performance characterization

As a first step in describing the behaviour of the FPA camera, an open beam response characterization was conducted. Based on preliminary work it has been observed that the integration energy of the camera, that is to say the amount of charge built up at the charge capacitors of the detector element read-outs, should be set to a level of approximately 9000 counts. This energy level is always approximated because the Lancer calibration window only allows for course adjustment of this parameter through manipulation of the integration time at the FPA, which in turn is a parameter that may be controlled precisely. Additionally, it is known from that the level of co-additions of continuous scan FTIR spectrometers will generate a square root improvement in SNR performance, while preliminary work in our labs, as well as other groups ²³ has shown the impact of this to be slightly diminished due to the complexities of the FPA detector. The adjustment of integration time/energy and the level of scan co-addition was investigated further in order to model correlations between the levels of FPA RMS noise on two levels: 1) as an overall FPA noise response value (figure 3.1, below), and 2) as a detector element distribution profile (figure 3.3, page 58).

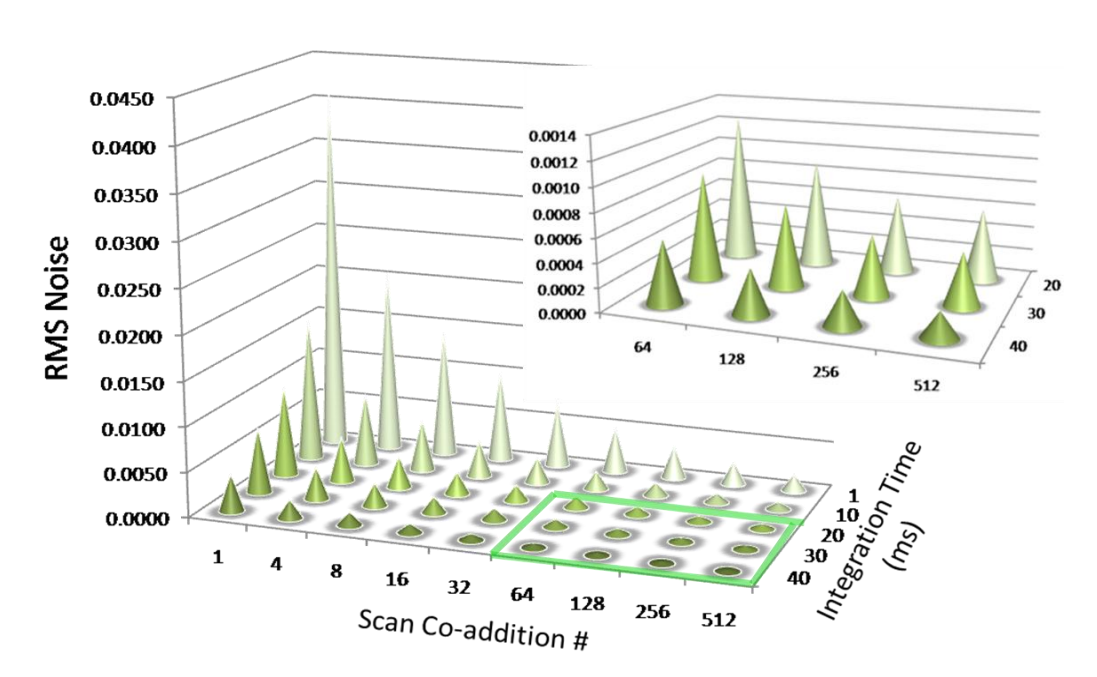


Figure 3.1. The average FPA RMS noise value from the region between 1800-1700 cm⁻¹, 8cm⁻¹ resolution, against co-addition and integration energy.

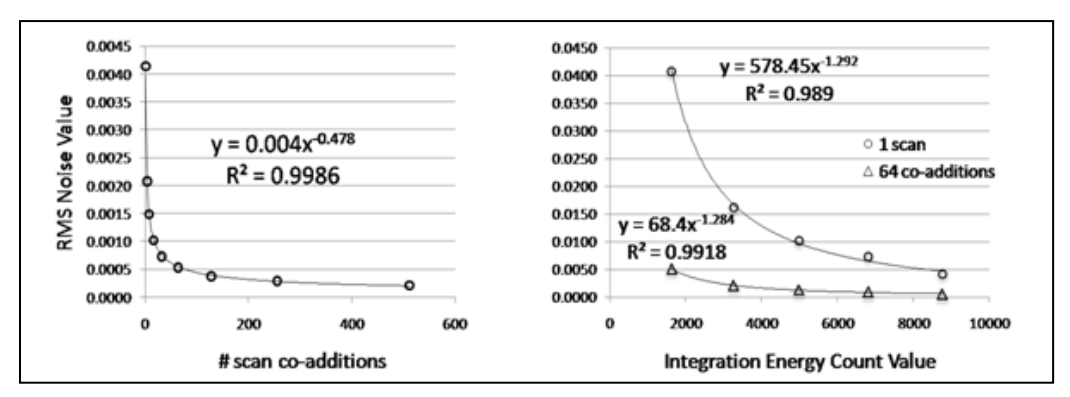


Figure 3.2. Left graph, power function relationship between RMS noise and number of scan co-additions at constant integration energy (8500); right graph, power function relationship between RMS noise and integration energy for two levels of scan co-addition.

The usefulness of the data from figure 3.2 is limited in that these values represent only the average response of all detector elements within the FPA. Nonetheless this information does provide a sense of the achievable noise performance for the FPA as a whole. Looking at the left graph in figure 3.2 it is observed that there is the expected trend for a photovoltaic detector, with a roughly square root reduction in RMS noise as a function of increasing scan co-addition. In terms of integration energy the RMS noise again decreases as a power function (right graph of figure 3.2), although the gains of this are depreciated significantly at higher levels of scan co-addition. It can be said that as a reasonable compromise between scanning time and noise level, the optimized noise performance of the FPA detector as a whole is RMS = 3.0×10^{-3} for the defined region (1700-1800 cm⁻¹) which is characteristic of the spectral profile for this MCT-FPA detector (4000-950 cm⁻¹). This relates to a detection limit of the detector array as a whole in the magnitude of milli-absorbance measurements, 1 and 2 orders of magnitude larger than that of DTGS and MCT single-point detectors, respectively.

The information in figure 3.3 begins to provide more exhaustive insight into what really lies behind the average noise response reported above. The plot shows both the standard deviation (SD), and the coefficient of variance (CV) for all of the detector element noise responses within the FPA. This is an open beam response therefore only the source, instrument optics, and the detector array could contribute to these levels of variation. Assuming that any variations from the source are negligible, that the variations from the instrument optics are constant, and that an NUC has been

performed on the detector array prior to image collection, the magnitude and spatial profile of the RMS noise response distribution must be attributed to the detector elements comprising the FPA detector.

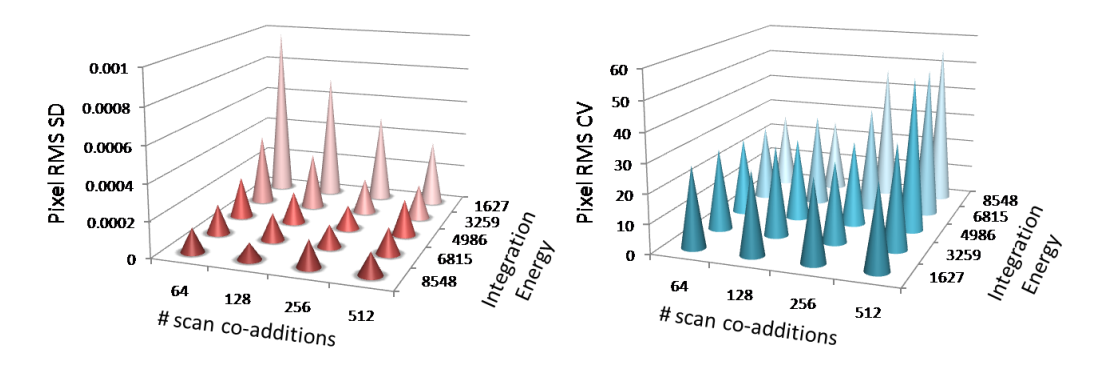


Figure 3.3. Impact of scan co-additions and integration energy on pixel RMS SD (left graph) and RMS CV (right graph). RMS SD calculated from 1024 pixels of image, RMS CV = (RMS SD/RMS mean) \times 100. Note the inversed integration energy scale between the two graphs (for clarity).

Looking to the SD graph in figure 3.3 it is seen that increases in each parameter have a positive effect on the distribution of pixel RMS noise, although these improvements become less apparent at higher levels of integration energy and higher scan coadditions. This then supports the utilization of higher integration energies (>7000 counts), as with the RMS noise distribution there is essentially a plateau for scan coadditions greater than 64. However the data in figure 3.1 still holds, i.e. the mean pixel RMS noise level continues to decrease with increasing levels of scan co-addition, and this is reflected in the CV graph in figure 3.3. The CV increases in the 512 co-addition category due to the SD remaining relatively constant, but the mean RMS value decreases. Therefore the scanning conditions in terms of distribution of noise response are optimized when greater than 64 co-additions and integration energy of ~7000 counts are employed. Based on this, figure 3.4 illustrates this distribution as a 2D representation and histogram.

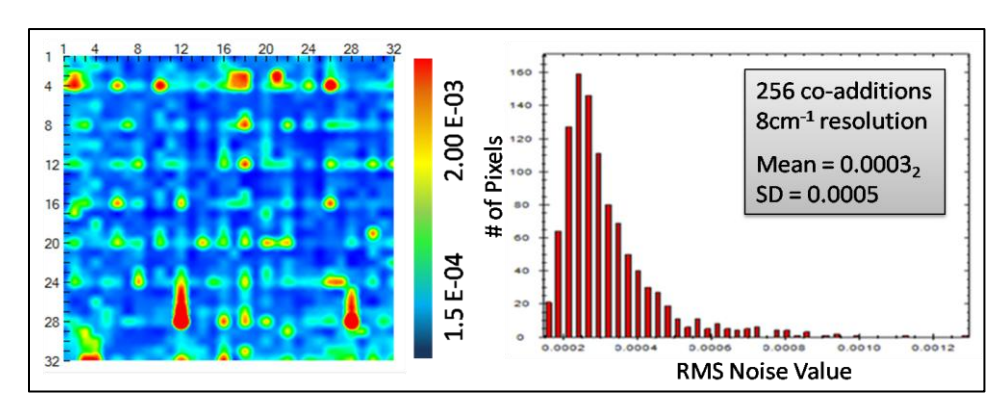


Figure 3.4. At left, 2D plot (pixel row x column of FPA) of RMS noise for the predefined region (1700-1800 cm⁻¹); at right, histogram representation of RMS noise distribution over the FPA.

Looking at the 2D plot of the pixel response found in figure 3.4, it is immediately apparent that a non random *spatial noise pattern* is persisting after the NUC performed on the FPA prior to scanning. This pattern of higher noise pixels is so regular that it can be attributed to every fourth row (4, 8, 12 ... 32) and less regularly within the even numbered columns – a pattern that matches previous observations with the same instrument under a wide range of scanning conditions ¹⁹. This pattern has been attributed to the fabrication process ¹⁹, and appears to be more pronounced in the later generation FPA's compared to the older generation within our own lab. This patterned noise is evident as the long right tail of the histogram, and consistently amounts to roughly 20% of the total detector array, with some rows/columns appearing more affected than others (e.g. row 4, column 18). This can be measured in a variety of ways, but an adaptation of the 2D image in figure 3.4 allows for the visualization of the removal of pixels based on RMS noise cut-off (figure 3.5).

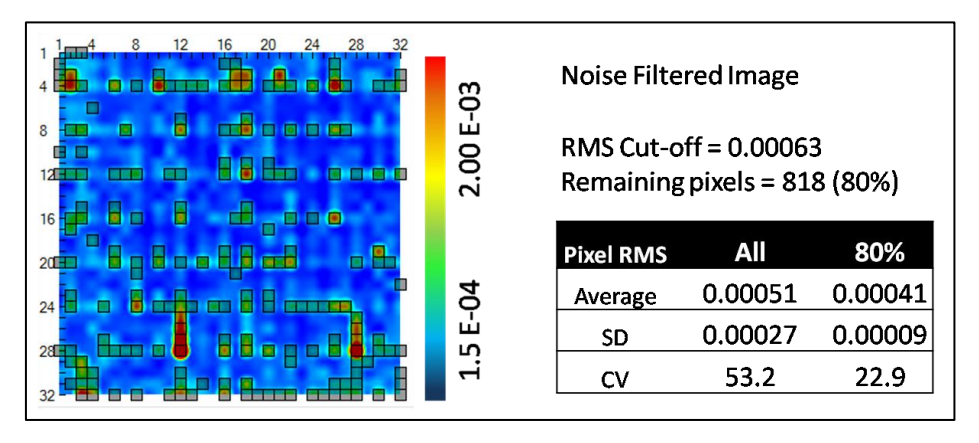


Figure 3.5. 2D plot illustrating the impact of an RMS noise cut-off for the removal of high noise detector elements from the overall response.

Figure 3.5 demonstrates how a noise filter cut-off can easily be applied to an image for the removal of the detector elements based on the noise features. The filter here has been designed to remove the spatial noise – the darkened pixels (squares) have been removed from the overall image, related in the adjacent statistics and also in the unseen histogram where the long right skew has been completely eliminated. The remaining pixels (80% of the FPA) exhibit an improvement in their descriptive statistics: a slightly depressed average, a significantly depressed SD – relating to a significantly lower CV value. This technique may be easily employed as a pre-filter in order to improve the overall sensitivity of the FPA, and to enhance the overall uniformity of the selected pixel population. It is noted that the top 10% of pixels have a mean RMS noise value of 0.00028 +/- 0.00002 (1SD), yielding a CV of 8.4% (see table 3.1). Regardless if 20% of pixels are removed, if looking to microfluidic applications a large number of detector points will still exist along the fluid path – with the ability to pick from the population of pixels to optimize the spectral information obtained.

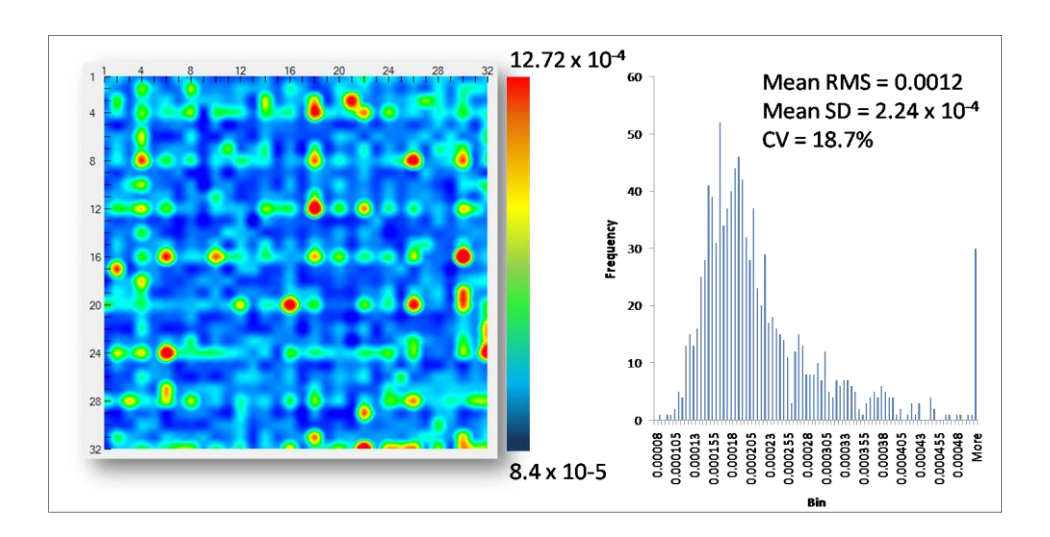


Figure 3.6. RMS SD per pixel, the result of 20 repeated scans, 64 co-additions, and 8 cm⁻¹ resolution. The value at each pixel is the SD for that pixel from 20 repetitions of the noise measurement. RMS noise measured from the region 2300-2200 cm⁻¹.

A comment on the consistency of noise response among the individual detector elements of the FPA, where there is a range of consistency when looking to individual pixels for a series of repeated measurements. It appears (see figure 3.6) that the same spatial pattern seen with 'noisy' pixels is seen with 'inconsistent' pixels, i.e. not only do these pixels posses higher noise response, they are also the most erratic of the FPA as

well. Therefore, a filter based on RMS noise cut-off could eliminate the inconsistent pixels (in terms of noise response) to the desired level – within limits. The average level of stability as measured from the data in figure 3.6 is found to be a mean SD in noise of 2.24×10^{-4} with a CV of 50.6%. After filtering 20% (with highest SD removed), the mean SD is 1.80×10^{-4} with a CV of 20.4%. A similar pattern is observed as with the image filtering based on raw RMS noise.

3.3.1.1. Pixel Selection and Co-addition Strategies

A simple means of selecting/removing pixels from within the FPA image, based on their relative noise properties, has been demonstrated. Previous work in our own lab has demonstrated that gains in noise performance can be obtained by co-adding pixels within the array — similar to using scan co-additions for noise improvements. It was observed that the gains from the co-adding of pixels, which resulted in a power function improvement, were significantly diminished at levels of co-addition greater than 64 pixels. In this scheme the pixels were selected at random from over the FPA until no pixels were left - a valid procedure when looking for the selection of best quality data from a heterogeneous image encompassing the entire FPA field of view. However, it leaves the question of how co-adding specific areas of the FPA can improve performance, particularly when it has been observed that definite features of spatial noise exist within the FPA image.

	RMS Noise Average Per:				
FPA	Raw total	Filter1 (90%)	Filter2 (80%)	Filter3 (50%)	Filter4 (10%)
Average	0.00051	0.00044	0.00041	0.00035	0.00028
Std. Deviation	0.00027	0.00013	0.00009	0.00005	0.00002
Columns	Column	2 Columns	4 Columns	8 Columns	16 columns
Average	0.00042	0.00042	0.00041	0.00041	0.00041
Std. Deviation	0.00004	0.00003	0.00002	0.00002	0.00000
Rows	Row	2 Rows	4 Rows	8 Rows	16 Rows
Average	0.00041	0.00041	0.00041	0.00041	0.00041
Std. Deviation	0.00003	0.00002	0.00002	0.00002	0.00001

Table 3.1. FPA portion of table illustrates the gains in the pixel distributions noise performance with the elimination of high noise pixels; filter value indicates portion of the FPA which has been used to generate average/SD. Columns and rows portion of table illustrates how pixel co-addition of spatially adjacent pixels impacts the overall noise performance. The row/column data have had filter 2 run before the co-addition of remaining pixels, therefore not each column/row had equivalent pixel volume.

Using the same example of the optimized open-beam response image from the previous section (RMS noise from the spectral region 1800-1700 cm⁻¹, 4cm⁻¹ resolution, ~9000 integration energy, and removal of the most severe spatial noise features), an analysis of continuously increased levels of pixel co-addition is investigated. The RMS noise data in table 3.1 illustrates the impact of further noise refinement, or noise filtering (FPA section), and also the impact of co-adding spatially adjacent pixels. The coadding of pixels has been carried out in the orientation of first columns of pixels, then rows – e.g. averaging a single row, then averaging two adjacent rows, etc. Whether the co-adding is conducted in the column or row sense, the end result is statistically equivalent. The standard deviations for the columns and rows differ from those in the FPA section of table 3.1, in that they represent the standard deviation between each of the columns – where the standard deviation for the FPA section represents the variation between individual pixels making up the average. This shows that an excellent degree of stability in noise terms can be afforded by careful co-addition of spatially adjacent pixels within the FPA. The downfall of the pixel co-addition approach is the loss of spatial resolution of the already diffraction limited IR microscope, thus the benefits are highly application specific - e.g. co-adding pixels from a highly heterogenous sample for noise improvement purposes would be inappropriate, and conversely laterally co-adding pixels with in a homogenous fluid stream can be highly beneficial.

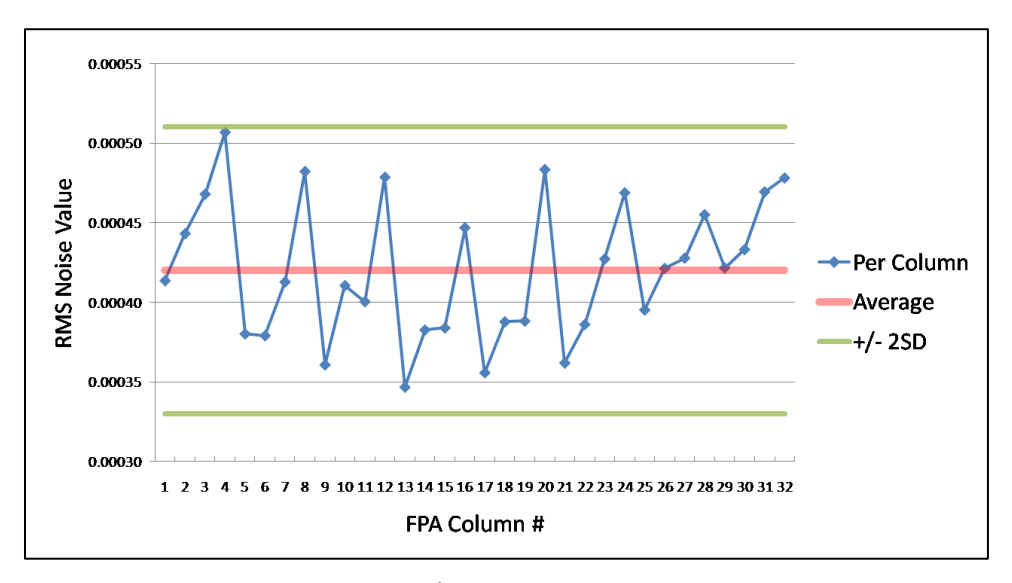


Figure 3.7. RMS noise (1800-1700 cm⁻¹) average per FPA column. Data is averaged after the removal the highest noise pixels (filter 2 as in table 3.1), therefore each column does not have the equivalent number of pixels.

Figure 3.7 illustrates how each column of the FPA falls within a 95% confidence interval of the global average. This distribution may be further refined with higher degree of noise pre-filtering, or with increased levels of pixel co-addition. It is also interesting to notice the periodic pattern of noise moving across the FPA in column increments – almost consistently a low, then a steady rise over 1-2 columns, then a rapid drop and plateau minimum for 1-2 columns, and again back to a maximum. The distribution of the noise when regarded per column, has roughly the same mean value of noise compared to that of the entire (filtered) FPA, although the distribution over the FPA is greater – this distribution has a CV < 5% in most cases when comparing the noise between divisions of the FPA (see table 3.1), while it is again emphasized that the remaining spatial noise features will certainly bias these distributions. As a whole, with some minor selection, the behaviour of noise between detector elements is relatively stable, with a consistent distribution that may be enhanced to a small extent by pixel coaddition.

3.3.1.2. Atmospheric Interferences: FPA-FTIR Purge Issues

As an extra measure to guarantee the quality of the spectra collected from the FPA-FTIRI system, the dry air purge system was assessed. As mentioned in section 2.1.5.4, atmospheric contributions can present a significant source of interference, and can be thought of as noise. However, as opposed to detector limited noise features the atmospheric contributions of CO₂ and water vapour can be controlled through instrument/experimental design, and shouldn't form a significant disturbance to any imaging result. Figure 3.8 shows how the instrument picks up levels of atmospheric interference when the system is left unsealed – more specifically the microscope stage has been isolated as a major source of atmospheric interference. By isolating the stage and letting the purge take its course it was possible to reach detector limited performance in the atmospheric regions of the IR spectrum. The ability to do so will be essential when looking to perform sensitive analysis of biological samples, for example protein measurements based on the Amide I and Amide II peaks would be severely compromised if the stage is left unsealed with any amount of disturbance present during IR measurements. This procedure ensures that a stable system is achieved,

whereby biological or other samples with spectral features in the atmospheric windows are uninhibited, i.e. maximization of sensitivity for these measurements.

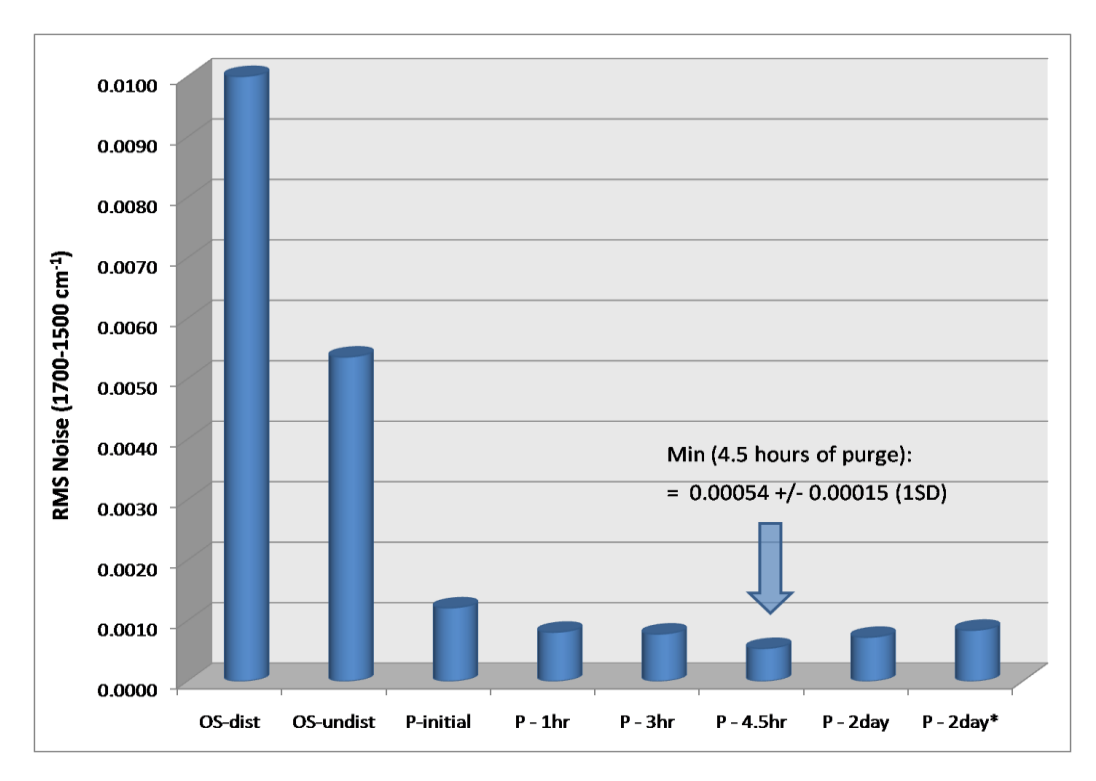


Figure 3.8. Plot of purge conditions versus RMS noise measure from the water vapour region of the IR spectrum – more efficient purge equals lower 'noise' measure. OS = open microscope stage; P = purge; dist. /undist. = disturbed/undisturbed stage; 2day* = application of initial disturbance to sealed stage.

3.3.2 Polystyrene Film Analysis

The first step of the FPA-FTIR response characterization was to take a close look at the noise features of the FPA detector by sampling the open-beam under a variety of conditions. The next phase was to introduce a controlled standard to generate a chemical response — a polystyrene calibration film was selected for this purpose. The polymer film was fixed to the microscope stage in such a way that the same point of the film would be sampled per detector element for a series of scans.

The polystyrene, when under magnification, is visually granular (see figure 3.9). This made the fixing of the sample to the stage all the more important – though when measuring the magnitude of these features under the microscope it is questionable whether the spatial resolution capabilities of the IR microscope would detect these differences, i.e. pixel crosstalk will smooth out most subtle features.

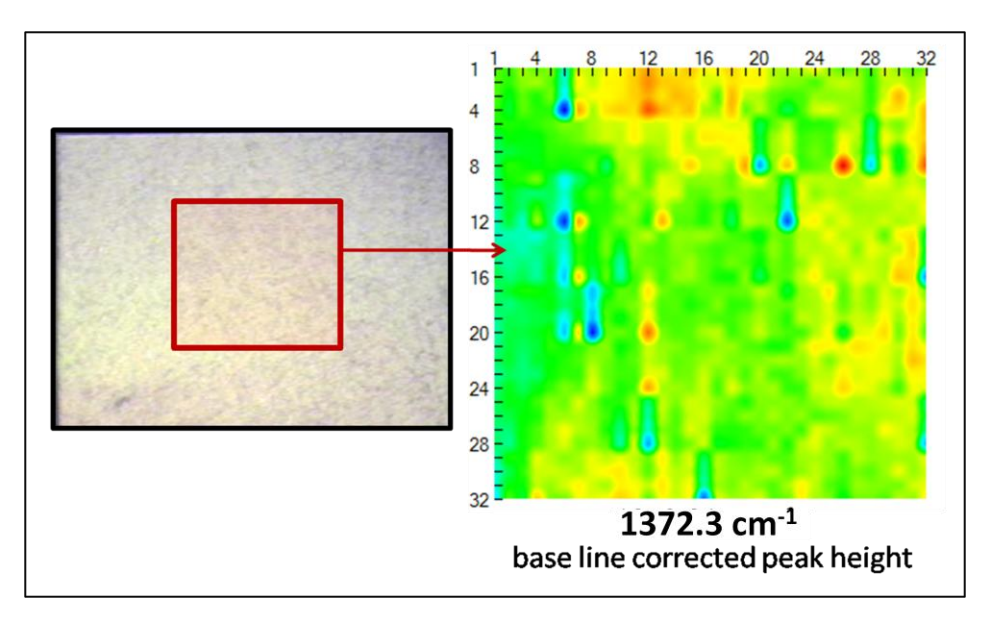


Figure 3.9. Optical and IR image of polystyrene. IR sample portion of optical image is highlighted.

The IR image in figure 3.9 is modelled on a two point baseline correction (1977.0-1919.2 cm⁻¹) and a peak height measurement at 1942.3 cm⁻¹, and was selected based on its relatively isolated position and an optimal absorbance range (~0.3). Looking in more detail at the image using this same peak response, the statistical distribution of the pixel response is presented in figure 3.10.

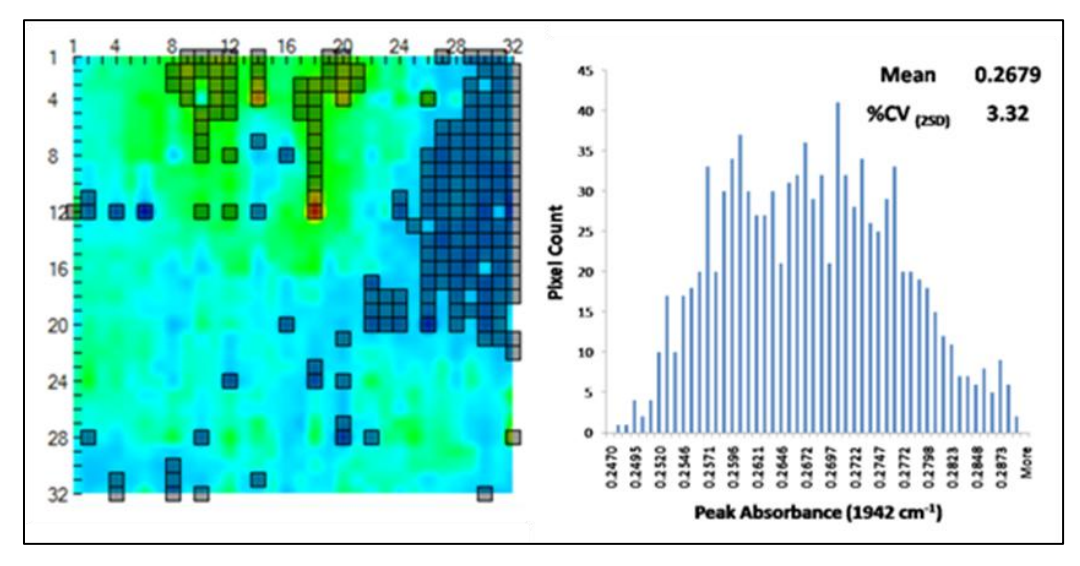


Figure 3.10. Distribution of detector element response at 1942.3 cm⁻¹ (after baseline correction). Image has been refined (darkened pixels) by removal of values outside +/-2SD, whereby the histogram represents the remaining pixel peak height distribution.

The refined image and histogram in figure 3.10 show that although the sampling area of the polystyrene is very small (180 x 180 µm) there is still an observable trend in the intensity of the peak height - which could be due to small differences in sample thickness, e.g. the right middle portion of the sample appears to be slightly thinner, while the middle top portion is slightly thicker compared to the bulk of the sampling area. Although these differences are rather minute, it is still important to utilize the pixels to the more homogenous portion of the sample, and after doing so the CV amounts to roughly 3.3% around the mean (0.2679 +/- 0.0088). Looking back to the noise analysis, it was observed that a milli-absorbance level of noise performance was achievable, thus it appears that an additional effect is taking place increasing the level of variation beyond what one might expect solely on the noise limiting behaviour of the pixels. A similar situation is observed for the analysis of peak area between 1975.1-1915.3 cm⁻¹ using the same baseline correction as peak height measurements, and the refined pixel information a CV value of 4.6% (7.0389 +/- 0.3222) is obtained. Likewise for the first derivative of the same peak features the CV value is 2.38%, and for the second derivative the CV is 3.57% over the refined area of the FPA. Thus it appears that performing a 1st derivative transformation of the detector element spectral data compensates for some of the variation not compensated for by a baseline correction, and provides the tightest distribution of response of the FPA as a post-treatment of the data (a gain of 1% in terms of CV value). Another aspect of figure 3.10 is that based on the peak height absorbance of the pattern of response is no longer as obvious; however when a 'quiet' region of the PS spectrum is modelled for RMS noise the same pattern (as in figure 3.5) persists. Additionally when looking to other PS peaks in a similar manner (figure 3.11), with a few exceptions (out of range peaks, CO₂ stretch, increased trend in fingerprint region) the level of variance appears relatively consistent throughout the spectrum.

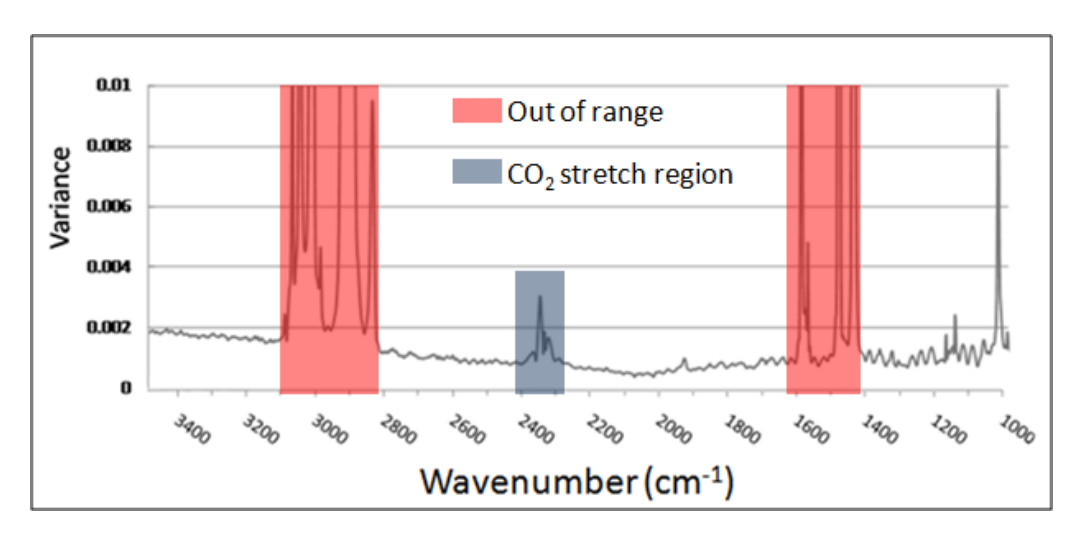


Figure 3.11. Variance spectrum from 1st derivative spectra for 1024 pixels of an image of PS.

Another aspect of spectral response that was observed using the PS standard was to quantify the consistency of detector element response in terms of 1) back to back scan response, and 2) day to day scan response. For simplicity the peak at 1942.0 cm⁻¹ is characterized using the same baseline correction and first derivative data processing protocols used above. The sampling for the back to back study consisted of a assessing each pixels response for a set of 20 scans using optimized scanning conditions (256 co-additions, 9000 integration energy) and a spectral resolution of 4 cm⁻¹. These statistics and the resulting 2D image of %CV per pixel, for these 20 measurements are presented in figure 3.12, both for baseline corrected measurements and 1st derivative measurements.

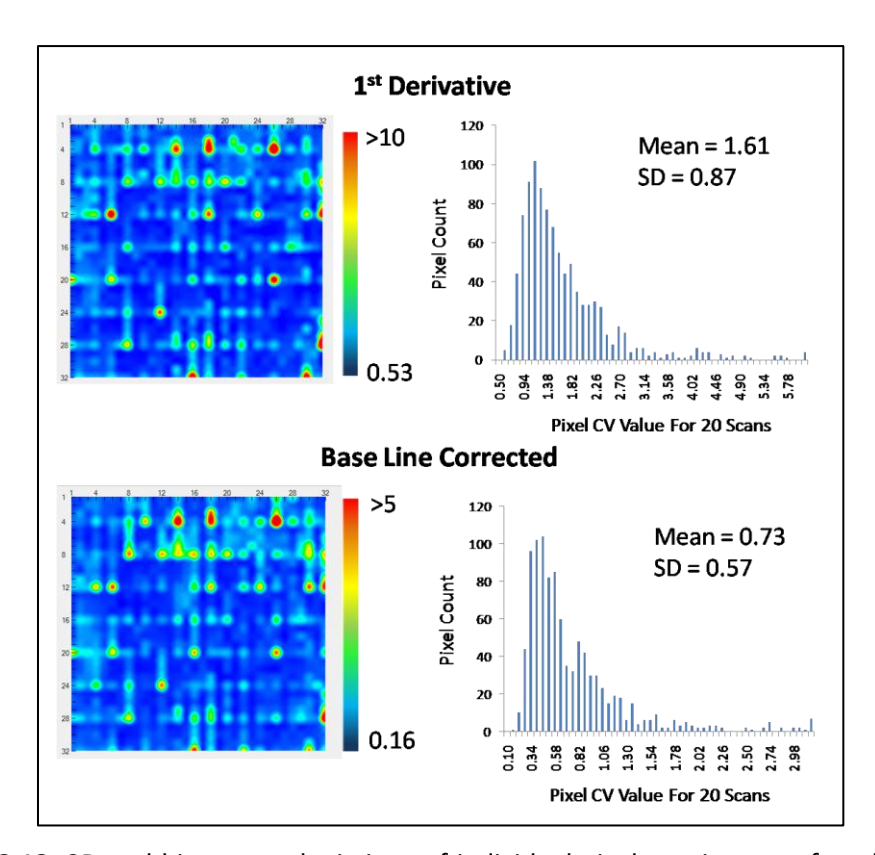


Figure 3.12. 2D and histogram depictions of individual pixel consistency of peak height response, for peak at 1942.3 cm^{-1} as base line corrected measurement, and a differential of the 1^{st} derivative measurement ($1936.5 - 1948.1 \text{ cm}^{-1}$). Each pixels value is calculated as the CV from 20 measurements.

Immediately it is very apparent that the noise features of the pixels seen in section 3.1 have translated to the pixel consistency of response, which makes perfect sense as pixels with lower SNR should relate to less stable measurements. Between the two methods of spectral processing the same pattern of consistency exists, however it appears that base line correction results in more stable measurements on a pixel to pixel basis. This is contrary to the observation made earlier whereby the response distribution within a single image was minimized in the case of a 1st derivative transformation compared to the base line correction data. These two characteristics a) magnitude of absorbance response distribution within a single image, and b) magnitude of pixel consistency distribution from a series of images, will each be of importance when performing quantitative measurements — and because each post-treatment technique can easily be applied, the benefits of each can be exploited.

The level of absorbance is important to the consistency of response, as has been suggested in figure 3.11 which describes the variance between pixels for each spectral

feature, with out-of-range absorbance resulting in very erratic response. This is of course a question of magnitude, and relates to the dynamic range - an important feature of any detector to quantify. As the dynamic range of MCT type detectors is notoriously limited (typically 0.2-1.0 absorbance units) there are no high expectations for the MCT detector elements of the FPA in this regard. Using the same technique applied in figure 3.12 to determine the distribution of pixel CV for a peak measurement an attempt to model the dynamic range using the PS standard was conducted, the result shown in figure 3.14.

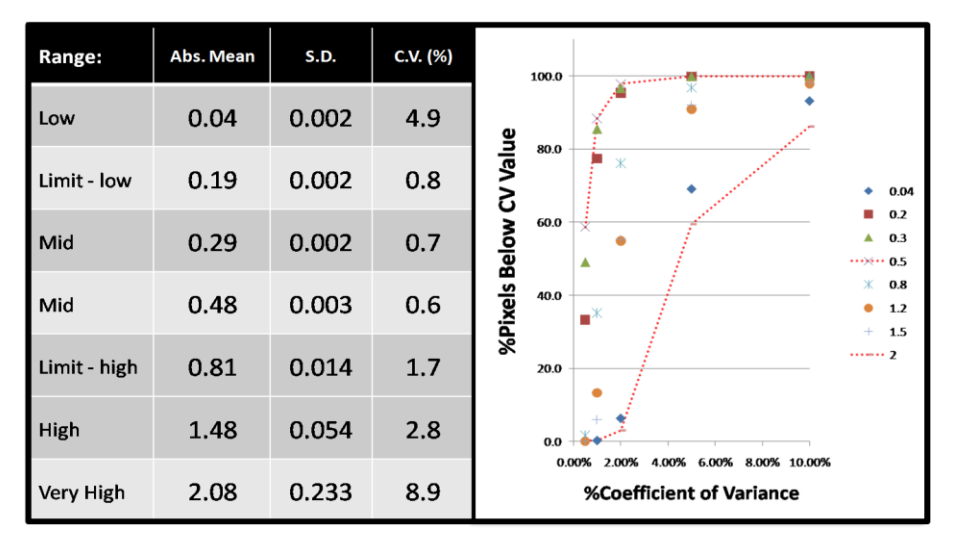


Figure 3.14. Baseline corrected peak measurements from peaks covering a wide range of absorbance. Peaks are selected from spectral regions of relative stability, and modelled for 20 repetitions; statistics at left describe the average absorbance distribution over the FPA for the various peaks.

The trend of CV distribution among the pixels for the range of absorbance measurements presented in figure 3.14, illustrates well the dynamic range of the FPA detector elements. It is apparent from the table of statistics, which are generated as the average of the 20 measurements for the pixel distribution, that peak heights above 0.8 absorbance and below 0.2 absorbance result in larger distributions of pixel response, while the tightest distribution is found around 0.5 absorbance. The graph at the right of figure 3.14 demonstrates that for a given absorbance value the proportion of pixels with a CV value below a certain level will vary greatly depending on the level of that absorbance, e.g. the proportion of pixels with a CV \leq 2% at 0.5 absorbance is 95%, while at 2.0 and 0.04 absorbance only 5% of pixels perform this well. The assumption here,

which is backed by the data from figure 3.11, is that the level of variation between different regions of the PS spectra is consistent, and that the changes in the pixel stability are strictly due to the level of absorbance. If this is the case, then the dynamic range of the average pixel can be set to roughly 0.2-0.8, as expected of an MCT detector. However, there always exist a number of pixels that remain stable for a higher range of absorbance, thus depending on their spatial orientation and the number data points required filters could be established to select for a desired pixel population, e.g. number of pixels with %CV less than 1% (within 0.3-0.7 abs.) equates to roughly 80% of pixels. Perhaps not so coincidentally this amount of pixels (80%) is what remains after removal of the worst spatial noise features; while this fact together with the same spatial pattern observed in the CV plots (figure 3.12). It is a safe assumption that an RMS cut-off will achieve the same impact as a CV cut-off, seeing as these two are directly related.

The back to back scans of polystyrene helped to establish the FPA detector element stability within a single session with the FPA-FTIR, but what of the day to day stability? To answer this, the back to back scan analysis procedure was conducted over several days and observations on the distributions for several peaks were made. It is noted that between individual runs it was necessary to reposition the PS standard in order for the FPA to be recalibrated and a new background collected before the beginning of the days run. This data is graphed for a single peak height in figure 3.15.

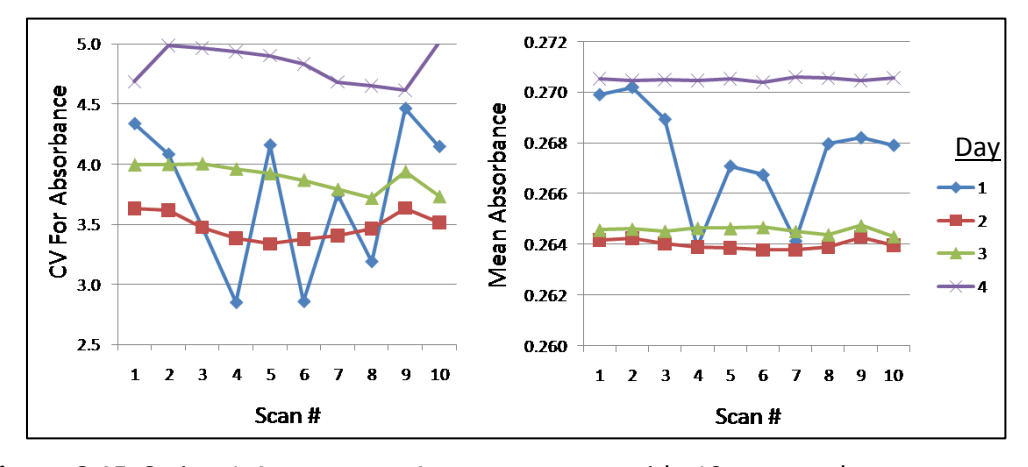


Figure 3.15 Series 1-4 represent 4 separate runs with 10 repeated scans per run. Measure was on 1942.3 cm⁻¹, with a 2 point baseline correction. Right graph shows the FPA average absorbance for the peak, left graph shows the relative magnitude of the distribution of that absorbance value over the FPA camera.

The information in figure 3.15 presents an interesting problem. The only differences between the series in these tables are the re-adjustment of the polystyrene strip and the time of analysis. Regarding the repositioning of the PS standard, this may account for the differences in the absorbance intensity between run 4 (latest date of analysis) and runs 2 and 3 (middle runs performed on same day with separate calibrations), but it does not explain the behaviour of run 1. The level of absorbance intensity spans the whole range seen between the other runs, but from one scan to the next. The chart of absorbance CV value mimics that of the mean absorbance - where run 4 has the widest spread of data, run 2 and 3 are fairly consistent with one another, and run 1 is the most erratic. The increase of CV value for run 4 seems disproportionate when compared with the data in figure 3.14, i.e. the increase in absorbance value does not seem to account for the increase in pixel response distribution. What can be said about the run to run data is that each is different from the next, and that the recalibration of the FPA prior to data collection seems to have an impact on the spread of data over the detector elements. It is encouraging that the two series within the same day generate quite similar responses; however it is apparent that when running quantitative experiments from one day to the next the response of the FPA camera would need to be carefully observed and corrected for above and beyond the NUC treatment provided by the instrument software.

An additional attempt to compensate for the non-uniformity among the pixels of the array involved the ratioing of peaks within the spectrum of the PS standard. Looking to the variability of individual peaks it has been demonstrated that the intensity of absorption is proportional to the magnitude of that response distribution over the FPA camera, and that a minimum distribution is found between approximately 0.2-0.7 absorbance units. In figure 3.13 the peak heights at 1583.6 cm⁻¹ and 1070.5 cm⁻¹ (CV = 2.75% for each peak, after +/-2SD refinement of pixel population, ~ 95% remaining) have been divided out for each pixel. The response for each peak is an average of 10 scans, 256 co-additions and 4 cm⁻¹ resolution, taken from series 2 in figure 3.15, as these readings are relatively stable. Based on the resultant distribution seen in figure 3.16 the spatial noise still persists, but the overall level of response distribution has been decreased nearly ¾ of a percent. Looking to other peak ratios a similar trend is observed, e.g. 1942.3/1155.4 cm⁻¹ achieves a CV value of 3.15% vs. 3.3 and 3.9%

(respectively) for the single peak measure. It is noted that taking a peak differential results in a widening of the pixel response distribution, e.g. when the difference per pixel is taken on 1155.4-1942.3 cm⁻¹ the resultant CV is greater than 10%.

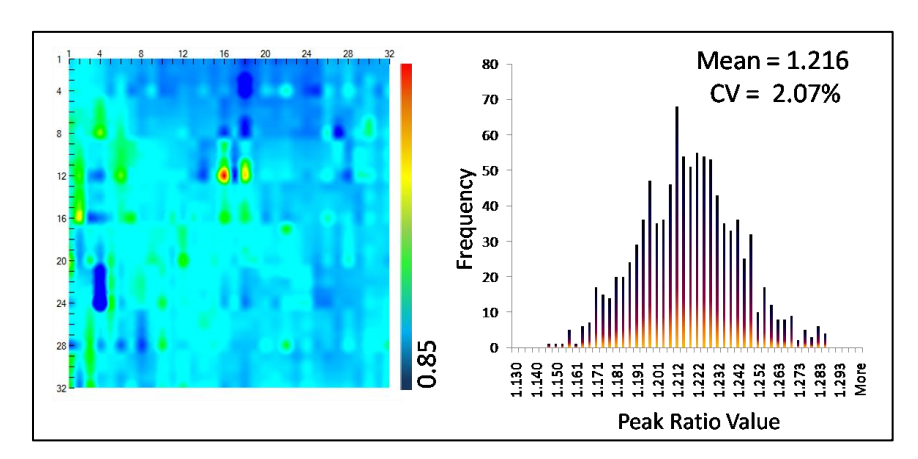


Figure 3.16 2D image and histogram distributions of pixel peak height ratio 1583.6/1070.5 cm⁻¹, each peak having a two point baseline correction.

3.3.3. Fluid Cell Measurements

As the end goal of this project calls for a novel transmission flow cell that incorporates the micro-fluidic fabrication of multiple channels for the observation of fluid streams. It is an important step then to optimize the collection of data from a transmission cell. Many conventional transmission cells have the fluid inputs/outputs set perpendicular to the fluid flow, where this presents a problem when sampling with an IR microscope, i.e. the cell design does not fit underneath the optics when the system is properly focused. Therefore a custom made cell was fabricated with the input/output lines sitting parallel with the inset crystal, with the fluid stream then flowing down and then through the crystal path-length forming a total of four 90° turns upon flowing in and out of the cell. The cell was a demountable design, with four screws for securing the two plates upon the cell and two gaskets. Four cartridge heaters were inset into the cell manifold, two for the top plate, two for the bottom, opposite of one another in order to achieve rapid and stable temperature control. The system could then be placed underneath the microscope stage, and fluid lines could be set in such a way that the microscope stage could be properly sealed and a proper purge obtained. A complete overview of the system is provided in figure 3.17, and the parameters of the equipment may be found in the experimental section.

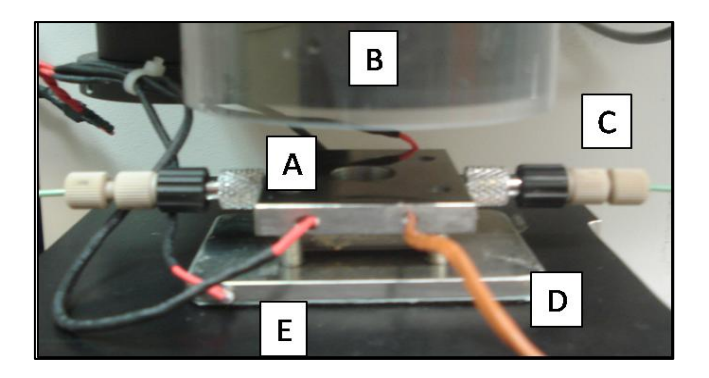


Figure 3.17. Apparatus used for FPA-FTIR transmission cell measurements. A – Demountable manifold with transmission port; B- IR microscope objective; C – Fluid line in (line out at left); D- Thermocouple; E – Heat cartridges (x4).

With the cell securely set onto the microscope stage, it was possible to obtain an optical focus of the cells path-length simply by passing a fluid stream (of the solvent to be used in the current experiment) and creating a series of bubbles within the pathlength. Subsequently the system may be flushed with the solvent to completely fill the path-length, and the FPA camera can be calibrated through the solvent filled transmission cell. Although the usual procedure for image collection involves calibrating the FPA with an unobstructed beam path (as in section 3.1 and 3.2) the practice of calibrating through the solvent filled cell allows for direct subtraction of the solvent media upon measurement. It is also convenient because the integration energy at the FPA can be more accurately established, i.e. calibrating the FPA with an unobstructed beam path to 9000 integration energy and then placing a liquid filled cell into the beampath will dramatically reduce the effective integration energy (e.g. ~6000-7000, dependant on pathlength and solvent/sample properties). The integration time at the FPA can be adjusted to compensate for the loss of integration energy, allowing for the recommended 9000 to be obtained at the cost of longer scan time. The resultant image of a fluid film of water is shown in figure 3.18, which includes the single beam spectrum, a 100% transmission line, and a peak absorbance measurement. The single beam spectrum is present simply to observe the visual homogeneity of the single beam over the FPA, and it appears that it is a tightly distributed feature according to the CV values (1.7% and 1.5% for the entire and top 10% of the FPA respectively). The 100% transmission line validates the spectral subtraction process for the FPA, as the noise features obtained match closely to those found in the open-beam noise analysis (see figure 3.1). For the absorbance measurement an aqueous solution of sodium azide (NaN_3) was used, as it is a well known internal standard ¹¹⁹, due to its good solubility in water and many organic solvents, and also due to its sharp absorbance between 2000-2100 cm⁻¹ where few other organic compounds absorb. It is noted that the liquid pathlength was calculated to be 33 μ m using the fringe method on the empty cell, and that the scanning was performed on a stopped flow of the liquid standard. Preliminary work with other solvent media (mineral oils) has shown the FPA calibration through the solvent (blank) filled flow cell to be the simplest and most effective approach to making quantitative measurements of such a fixed apparatus.

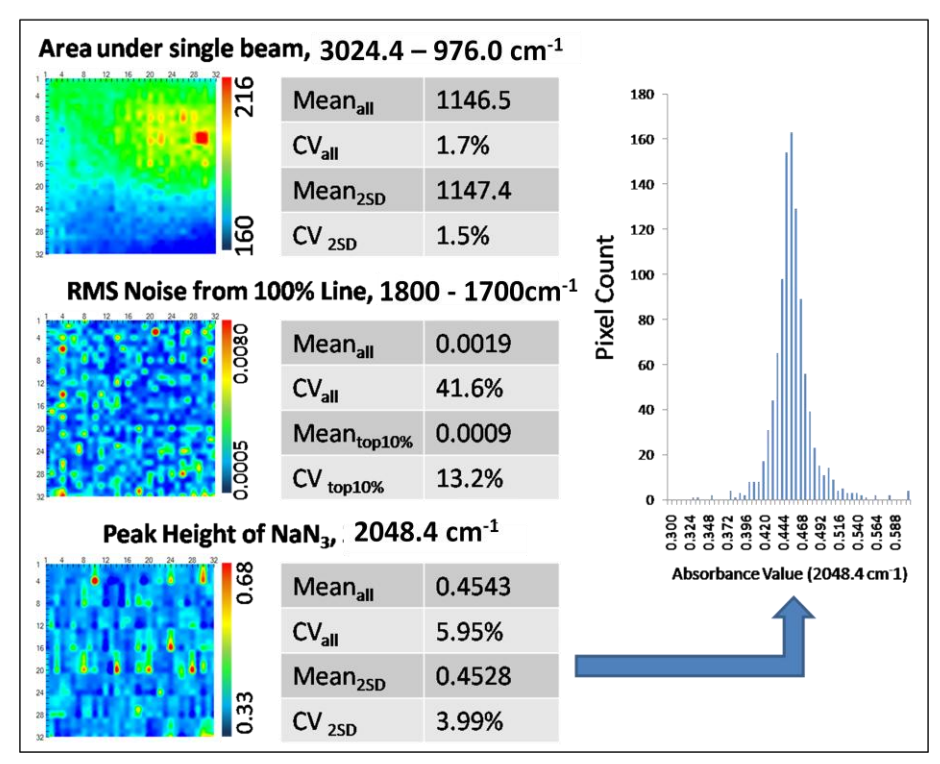


Figure 3.18 Distribution of FPA response through a liquid film. Top, image of single beam area; middle, image of noise response; bottom, image of NaN_3 peak, two point base line correction (2102.4, 1967.3 cm⁻¹).

The absorbance value of the NaN₃ NN double bond stretch at 2048.4 cm⁻¹, for a 0.3588 M aqueous solution resulted in a mean peak height absorbance value of 0.4543 +/- 0.0270 (95% confidence). Due to the highly centered 'normal' distribution, it was assumed to be valid to refine the data set by +/- 2SD, and when this is done the remaining pixels have a CV value of roughly 4%, down 2% from the raw pixel data. When compared to the PS standard peak (1942.3 cm⁻¹) with an average CV value for the raw pixel data of roughly 4%, and 3% when refined +/-2SD, the liquid film appears to be

generating a comparable magnitude of pixel absorbance distribution. Something noteworthy in the NaN₃ scan that was not observed with the PS scans is that the spatial pattern appears prominently in the FPA peak height map. This could perhaps be due to the relative molar absorptivity and path-lengths the respective samples, i.e. the NaN₃ molar absorptivity and smaller path-length generates a more sensitive response – one that is highly influenced by the noise aspects of the FPA detector. Alternatively the PS film may have an underlying fringe as a result of its film thickness (50 µm).

3.4 Conclusions

The impact of scanning parameters on the magnitude of RMS noise, and more importantly the distribution of that RMS noise over the FPA, has been evaluated. In terms of overall performance the individual pixels comprising the FPA detector are still an order of magnitude away from DTGS performance, while it is also noted that a relatively greater amount of time is required to obtain the levels of co-addition used in these experiments. When the integration energy is set above 7000 counts and the level of co-addition of pixels is greater than 64 the impacts on the pixel RMS noise distribution are maximized (lowest SD). The same spatial noise pattern observed in past work was seen again here, and is easily eliminated using an RMS noise cut-off filter, reducing the pixels to a roughly normal distribution of response. The actual volume of pixels with extreme noise measures relative to the median is small, and a 20% removal of pixels based on their noise properties safely removes the spatial noise patterns. Based on the post filtered normal distribution of detector element noise response, the average pixel of the FPA is limited to milli-absorbance noise levels – giving an impression of the instrument detection limit for quantitative analysis by FTIRI. Through the coaddition of spatially adjacent pixels (post removal of the spatial noise features) it was established that when looked at as a series of 32 parallel detectors there are negligible differences between rows/columns of the FPA as averages. When looking to repeated back to back analysis of pixels, it is observed that the average deviation in noise response per pixel is 10^{-4} , thus the noise response of pixels is quite stable – not considering those which are removed with the RMS noise cut-off filter. Thus the pixel noise is a relatively unwavering measurement, resulting in very sharp non-random features within the FPA, which may be removed if necessary, leaving a pixel population with the ability to make measurements with milli-absorbance accuracy.

It was found that for making mid-range absorbance measurements (0.268 Au) that the CV for the pixel population rested around 3%, amounting to a range of absorbance values from 0.259 to 0.277, well outside the expected level of deviation due to the pixel noise characteristics. This establishes the level to which pixels generate different responsivity – an additional effect to the noise distributions. For the individual pixel the mean CV for a series of 20 measurements was found to be 0.73 +/- 0.57%, which rests at the level of milli-absorbance accuracy - thus it is just when comparing the pixel population with one another that larger variations in absorbance are introduced. Additionally, the level of absorbance plays a key role in the average pixels absorbance stability, e.g. for peaks greater than 1.0 absorbance the population of pixels with a CV value less than 2% is severely diminished (5%), while at an absorbance of 0.5 that value is greater than 95%. This establishes a dynamic range for the pixels comprising the FPA, as outside the range of 0.1 and 0.8 the distribution of absorbance measurements among the pixel population begins to spread, and the consistency of individual pixels for those measurements also rapidly degrades. This shows that it is possible to generate FPA detector elements with wider dynamic ranges, and these may be selected for by the same process of pixel CV determination in other experiments.

A procedure was developed for the FPA-FTIR imaging of a flow through transmission cell, where the FPA calibration procedure was adjusted to perform the NUC step through the solvent (water) filled cell. The procedure was validated, and no negative effects were observed on the pixel response distributions relative to the open-beam and polystyrene results. The selected pathlength (33 µm) resulted in a peak height of the standard in the optimum absorbance range of the FPA, where the distribution of peak height over the pixels amounted to a CV comparable to the PS work (~4%). This work provides insight to just what is the single detector elements response like – what level of noise, and how stable are the measurements made. The apparent ineffectiveness of the NUC supplied with the instrument software is troublesome, as this may limit the available data points in further experiments looking to extract quantitative information from spatially limited regions of the FPA. It appears that overall, the long tailed distribution of the spatial noise accounts for roughly 20% of the pixels within the FPA, which translates to the removal of just over four columns of pixels from the total.

Chapter 4. Assessment of the Quantitative Performance of an FPA-FTIR Spectrometer

4.1 Introduction

In the previous chapter the FPA detector elements basic response characteristics were quantified. The noise performance capabilities of the pixel population were assessed, as was the absorbance responsivity. Also a procedure was developed and assessed for the FPA-FTIR microscope sampling of a demountable transmission cell, allowing for the facile imaging of liquid samples. With a system designed for the rapid loading of liquid samples, with accurate temperature control, the next step is to begin building models of the individual detector elements quantitative analysis capabilities. If the level of quantitative performance for the individual detector elements of the array can be established then decisions can be made about the application of these detectors as quantitative tools in real world systems. Applications which have already exploited FPA-FTIR do not generally do so with accurate quantitative measurements in mind, however the quantitative accuracy of individual detector elements has implications to any chemical measurement being made. If the relative responses of adjacent detector elements are to be used in making crucial decisions, a certain level of confidence must be ascertained such that their response is not merely an artefact of non-uniformity between detector elements. Measuring in the context of a quantitative analysis study allows one to make many valuable observations which are entirely relevant to qualitative applications as well. For example, if a bacteria smear is being scanned for the purposes of building a database for an expert bacteria identification system, but a considerable percentage of the FPA detector elements are generating inconsistent and/or erratic spectral responses where that percentage is characteristic of that detector – what impact will that have on the transferability of that spectral information if another FPA-FTIR system is used?

Previous work ¹⁹ with this FPA-FTIR spectrometer conducted a quantitative analysis on series of standards made up of methyl myristate in odourless mineral spirit. It was established that as a global average of detector elements, a good linear regression curve can be obtained, but when examined per pixel a significant spread in the CV with increasing standard concentration was observed. This observation is consistent with

those made in section 3.4.2, whereby the level of absorbance of a peak resulted in larger distribution magnitude over the detector elements of the FPA. This work continued by investigating the relationship between 'noisy' pixels and the overall regression SD (CSD), where it was observed that a minimum CSD was achieved by averaging the highest 20-40% pixels in terms of noise performance. Additionally steps were taken to develop software capable of calibrating individual pixels of the FPA so that the regression statistic spatial distributions could be analyzed, where it was found that 60% of pixels have a run-to-run SD of less than 20 milli-absorbance units, while at the other end, nearly 20% of pixels have a run-to-run SD of 35 milli-absorbance units or much higher. These 20% of pixels were attributed to the spatial noise pattern seen previously. It was also observed that the level deviation from linearity was well in excess of what might be caused by the observed noise features of the FPA, thus an additional effect to pixel responsivity is taking place.

Using the techniques developed in this work with methyl myristate a further quantitative study of several aqueous model systems will be conducted. Starting with a model system of NaN₃, least linear square (LLS) regressions will be built for the individual detector elements of the FPA camera. The day to day performance for the same calibration will be established. From this data a different approach to co-adding will be employed, contrary to the random selection of pixels from the FPA, spatially adjacent pixels will be combined and the benefits to analytical performance determined. Additionally a series of food relevant analytes will be modelled, and finally a milk analysis study will be conducted. Milk was selected based on two reasons, 1) established methodology for the quantitative analysis of milk and other dairy products, and 2) the current use of FTIR spectroscopy for the analysis of milk in industry where each spectrometer is capable of carrying out 300-600 samples/hr employing a single element DTGS detector. The high-throughput requirements placed on FTIR spectrometers for the commercial analysis of milk gives a context where the FPA-FTIR system would have a significant cost-benefit advantage. Essentially the development of a cell capable of carrying multiple fluid streams would make the FPA-FTIR system equal to m conventional IR spectrometers (where m equals the number of channels in the cell).

4.2 Experimental

4.2.1 Chemicals and Materials

Sodium Azide (NaN₃) standards were prepared by weight with distilled, 0.45µm filtered water to give a range of ~0.060 M to 0.200 M. Solutions were stored in airtight amber glass containers, in the dark at room temperature, and used within 5 days. Milk standards were obtained from a laboratory specializing in milk analysis, and consisted of 6 standards with reference analyzed levels of fat, protein and lactose content. Samples were sealed in plastic containers provided by supplier, and the bulk sample kept refrigerated at all times. All milk samples wer analysed for fat content by Röse-Gottlieb method with a Mojonnier extractor; protein by Kjeldhal; and lactose by HPLC.

4.2.2 Instrumentation

Same spectrometer set-up as in section 3.3.2. was employed. A parallel study using the FTIR spectrometer equipped with a DTGS detector was also performed. Modifications were made to the microscope stage for collection of spectra from D_2O samples, in that the purge apparatus optimized in section 3.4.1.2 was adapted in order to maximize sensitivity for Amide I spectral region. The custom made transmission cell illustrated in figure 3.16, was clamped into place on the microscope stage, linked to heaters and a thermocouple for accurate temperature control of the fluid. The cell materials used were CaF_2 (ICL, IR grade), spaced with a combination of Teflon spacers to obtain a path-length between 30-40 μ m, with lead gaskets between the manifold and the cells to ensure efficient heat transfer.

4.2.3 Sample Acquisition

Optical focus of the transmission cell was obtained by focusing upon the outlines of bubbles within the cell. The cell was then filled with the solvent (water unless otherwise specified) and an area of the transmission cell free of bubbles and/or debris was found and the transmission cell locked into place. The FPA NUC procedure was carried out through the solvent filled cell by setting an integration time that achieved integration energy between 7000-9000 counts. Prior to background and sample collection the transmission cell was temperature stabilized, temperatures were accurate to within +/-

0.2 °C (30 °C for NaN₃ standards; 40 °C for milk standards). Injection of samples was done manually using sterile syringes connected to Teflon tubing, so that the transmission cell was left undisturbed under the microscope stage. Volumes of sample injection varied depending on sample media; the transmission cells volume itself was minute, however the lines leading to the cell required flushing of the previous sample to avoid cross contamination and/or dilution. The NaN₃ standards were injected as 1 mL aliquots, milk standards as 2 mL aliquots. Collection using the DTGS involved setting up the transmission cell in the regular transmission compartment of the instrument, with all the connections, temperature control, and purge measures taken with the FPA-FTIR sampling, being easily transferred – thus ensuring that the only difference in sampling was the detector being employed.

4.2.4 Data Processing

Spectral processing employed the same procedure as described in section 3.3.4. Additional in house software (ImagePLS) was developed for the processing of LLS and PLS calibrations for groupings of pixels and for individual pixel calibrations. Many of the same features available in ImageProcessor were available in ImagePLS, thus it was possible to carry out pre-filtering procedures before building calibrations based on groupings of pixels within the FPA. Further statistical analysis of the data generated by ImagePLS was carried out in Excel 2007 and/or Origins 7.0.

4.3 Results and Discussion

4.3.1 Aqueous NaN₃ Calibrations: Linear Regression Modelling of FPA Pixel Population

In order to appreciate the 'linear' performance characteristics of the FPA, a first step was to build linear regression calibrations using the FPA as a single point detector, and then to adapt what was learned in chapter 3 to refine that detector to the better performing elements and quantify the gains. The data in table 4.1 illustrates the impact on the linear regression statistics using the co-addition of pixels within the FPA, where pixels are grouped at random thus the co-adding of a single row or column will not likely occur. By taking the average of all pixels within the FPA to generate a data point, a regression curve very similar in quality to the DTGS curve is generated (see first row, table 4.2), with the exception of the differing slopes. The slope deviation is not unexpected when working with different detector types with different responsivity. When the FPA is randomly sub-divided through the pixel co-addition process, the overall linear regression CSD follows a power function trend with a root factor of 0.496, and an $R^2 = 0.9997$ for the trend, matching observations made in previous FPA calibration work with methyl myristate standards ¹⁹. Note the increasing SD with increasing standard concentration in the plot at the right in figure 4.1, a trend which supports the observations in figure 3.14.

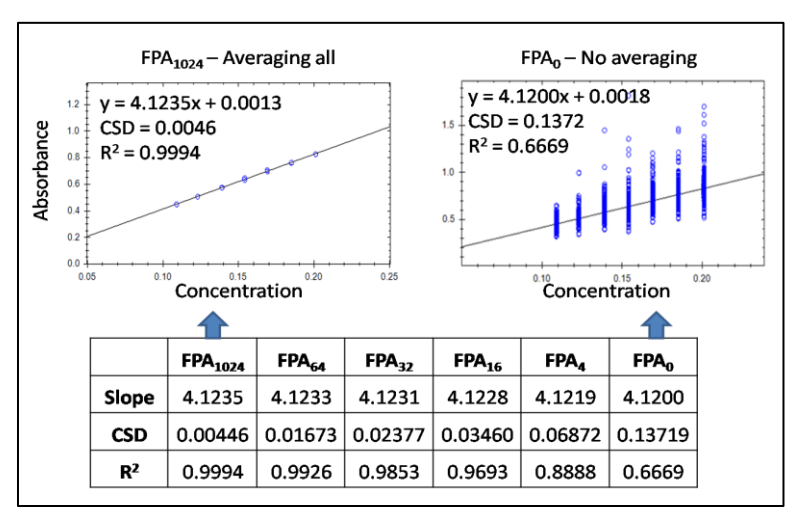


Figure 4.1 Linear regression data for increasing levels of FPA pixel co-addition, where the subscript indicates the number of pixels averaged to generate the data at a point in the calibration. Thus FPA₆₄ will generate 16 replicates per standard, each point consisting of the average of 64 random pixels.

Depending on the levels of pixel co-addition from within the FPA, some of the poorer linear regression characteristics can be negated. However, the sense in which the data in figure 4.1 was constructed is not useful for the end purpose of this project due to the nature of the co-addition process. When the FPA detection system is to be utilized for its spatial resolution capabilities with a series of adjacent fluid channels the data will need to be averaged in a spatial sense. It has already been demonstrated that a spatial noise pattern is evident on the FPA, which has serious implications to making quantitative measurements of multiple fluid channels within the FPA field of view. It is important to establish whether the spatial noise features relate to other pixel response characteristics.

Data Set	Slope, mean (CV)	CSD, mean (CV)	R ² , mean (CV)
DTGS	3.9517 (0.3%)	0.00443 (51.2%)	0.9996 (0.04%)
FPA ₁ (All Pixels)	4.1200 (9.3%)	0.03261 (>300%)	0.9703 (5.2%)
FPA ₂ (80% of Pixels)	4.0899 (4.3%)	0.02079 (60.8%)	0.9825 (1.0%)
FPA ₃ (50% of Pixels)	4.0901 (3.8%)	0.01877 (56.0%)	0.9887 (0.7%)
FPA ₄ (10% of Pixels)	4.0940 (2.8%)	0.01688 (50.9%)	0.9912 (0.5%)

Table 4.1 NaN₃ linear regression data for DTGS and for FPA pixel population with increasing levels of RMS noise filtering (FPA₂-FPA₄). DTGS data averaged from 3 runs using the same calibration standards.

The data in table 4.1 describes a) a DTGS calibration of the NaN₃ as a benchmark comparison, b) the FPA average – that is to say all 1024 detector element responses collected and averaged, and c) the FPA averages after pixel filtration based on the noise features of the calibration set. To remove pixels of the FPA image based on noise, the RMS noise in a region adjacent to the peak of interest were collected from each standard and averaged (per pixel). As can be seen the removal of noisier pixels from the FPA does enhance the linear performance of the detector as a whole – logical, as each of these other features have been attributed to the spatial features upon the FPA, and the removal of noise heavy detector element response from the average would be expected to boost the sensitivity and lower the variability in a linear regression model. Figure 4.2 elaborates table 4.1, showing the gains at 10% pixel removal intervals, and also shows the 2D representation of the regression feature being modelled. For each of the slope, CSD, and CC, the spatial noise features (see figure 3.5) are translated to poorer linear performance.

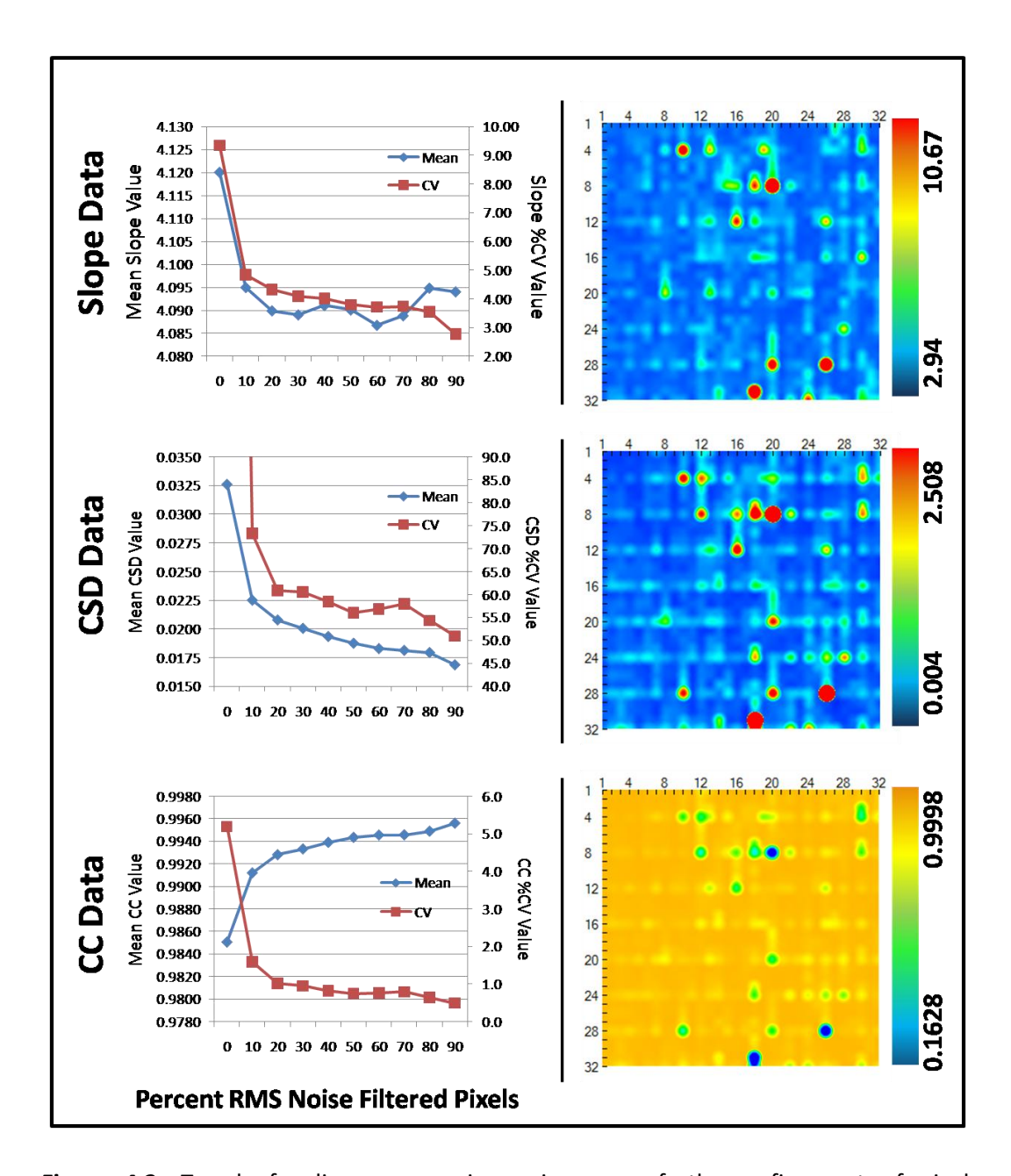


Figure 4.2. Trends for linear regression gains upon further refinement of pixel population according to an RMS noise filter. Each point in the plot represents the average of the remaining pixels (Mean series) and the magnitude of that features distribution (CV series). 2D representations of each feature (slope, CSD, and CC) with color scales illustrate their non-random spatial distribution over the FPA camera.

The slope and CC values follow a roughly power function gain, while the CSD is less predictable in this sense. In each case it can be seen that removal of greater than 20% of the pixel population based on their noise performance does not result in appreciable gains to the mean and the distribution around that mean. A comment that the CSD CV values seem disproportionately large; this is due to the magnitude of the absolute CSD values being relatively close to zero; thus it is the change in CSD CV values which form the important observation. Based on the trends of the spatial features seen in figure 4.2 it might be assumed that RMS noise would form a good basis for the reduction of the FPA pixel population to those with better linear performance. However, upon further inspection (figure 4.3), it appears that no strong correlation can be made between RMS noise features of pixels and their linear characteristics. Aside from the few outlying pixels which would be removed on the initial levels of RMS filtering, the pixel population is largely randomized, and further filtering will not have a drastic impact on the overall regression parameter. This then is what has been observed in figure 4.2, showing that the filtering of the pixel population based on noise is not the most effective approach, with many pixels showing lower CSD values being lost with lowest levels of noise filtration.

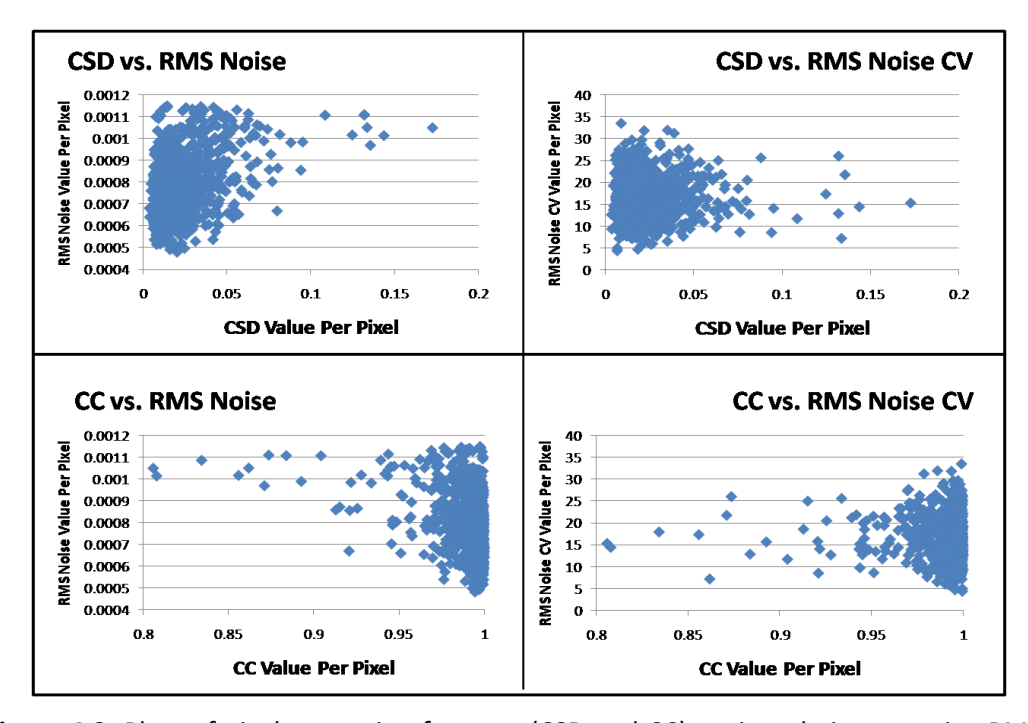


Figure 4.3. Plots of pixel regression features (CSD and CC) against their respective RMS noise characteristics (mean RMS noise and RMS noise CV), from a NaN₃ calibration set.

The selection of pixels based solely on their slope values is not an effective filtering option, as the slope values that are generated by the pixels say nothing about the fit of that slope to the data points, one only has to look at the CSD and CC 2D plots (figure 4.2) to see that there is a significant percentage of erratic pixel responses forming a spatial pattern over the FPA. It is these parameters (CSD and CC, or R²) that may shape an effective pixel selection procedure. The disadvantage of this approach is that a current calibration model must exist in order to apply the filter, where with an RMS noise filter the draw was that only a single image would be necessary to apply the filter. However, if the application at hand calls for the building of a calibration curve then this consideration is of little concern. Other possibilities of pixel selection filters were based on pixel CV value for repeated measurements, and a pixel relative error of prediction (%RE) based on an individual pixels ability to predict a validation standards concentration. To demonstrate the effectiveness of these various pixel filtering possibilities, table 4.2 is arranged to illustrate their impact on the predicative ability (RE) of the post-filtered pixel populations.

	%RE Per FPA Pixel Selection Filter:					
% FPA	%RE	CSD	CC	%CV	RMS	
Filtered					Noise	
20%	2.38 (75%)	2.73 (81%)	2.73 (81%)	3.44 (265%)	4.42 (264%)	
50%	1.41 (73%)	1.96 (77%)	1.97 (77%)	3.09 (360%)	4.62 (310%)	
80%	0.72 (74%)	1.32 (79%)	1.31 (80%)	3.82 (458%)	5.54 (375%)	

Table 4.2. Filtering of FPA pixels based on various parameters and their respective ability to narrow a pixel population with a consistently accurate predictive ability, measured as %RE. Values = %RE (CV).

Each of these filter approaches is an improvement over the unfiltered FPA pixel population, found to generate a mean %RE = 6.2% (CV = 620%). However, it is apparent that the RMS filter approach is among the least effective in retrieving the pixels with superior quantitative performance – if the relative error measure is to be trusted. The absolute value of the mean %RE and the magnitude of its distribution after the RMS noise filter and %CV filter show the worst selection ability. What's more, further refinement of the FPA based on pixel RMS noise performance actually selects for pixels

with increasingly inferior predictive ability. The CSD and CC filter selection procedures approach the level of the direct %RE filter, with removal of 20% of pixels based on these values almost matching that of the direct %RE filter. Also, it doesn't appear that there is any significant advantage to using one approach over the other (CC vs. CSD), as the statistics are virtually identical. For the refining of the pixel population, in terms of predictive performance, a direct CC or CSD filter appear to be the best approaches.

For the current conditions (64 scan co-additions, 8cm⁻¹ resolution, ~8000 integration energy, NaN₃ linear regression model, and a 20% CSD pixel filter) the average pixels response characteristics are:

- CC, 0.9973 +/- 0.0021
- CSD, 0.01247 +/- 0.00455
- Slope, 4.1058 +/- 0.2853
- RE, 2.73 +/- 2.33% (for the prediction of a mid-range standard).
- RMS noise, 0.00083 +/- 0.00026

A further question around these pixel characteristics which has not yet been addressed is that of their day to day stability. This was addressed simply by running the same NaN₃ calibrations repeatedly, ensuring that the same experimental conditions were applied, so that the only difference between runs will be a new NUC for the FPA, a slightly different integration energy, and in some cases a new NaN₃ calibration set. A total of 6 runs are presented, the first 4 are from the same calibration set over a period of four days, while the 5th and 6th are each from separately prepared calibration sets on separate days.

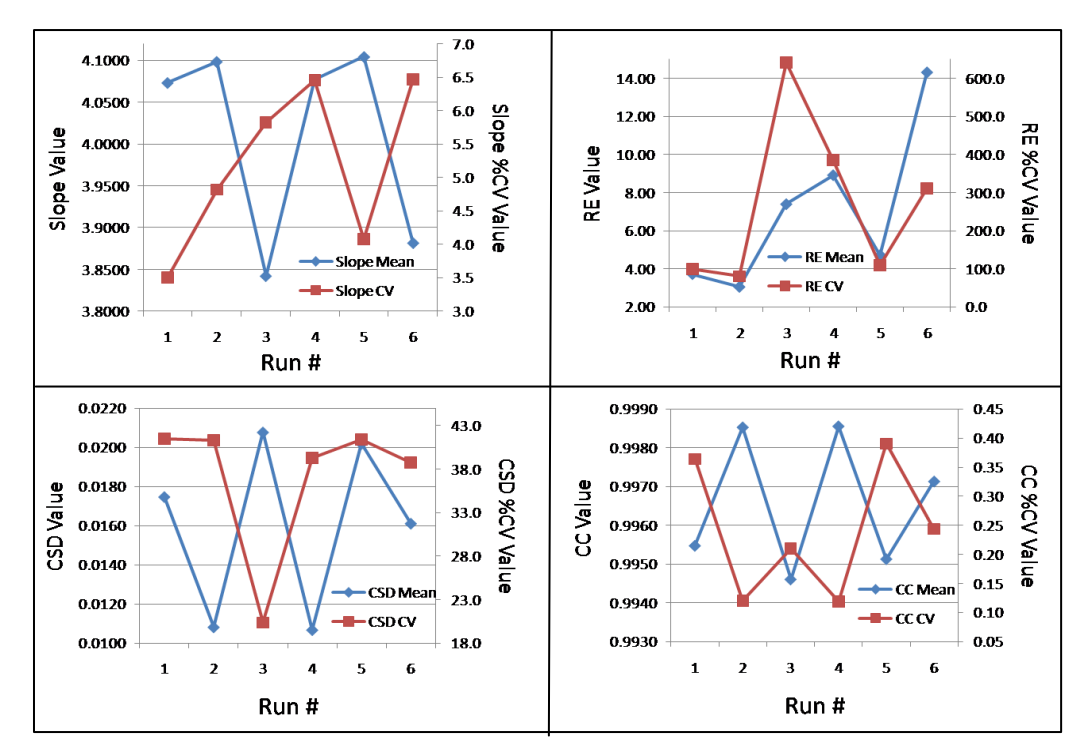


Figure 4.4. The day to day stability of various linear regression calibration features of NaN_3 . Each point is determined from the top 80% pixels of the calibration run based on pixel CSD values.

With regards to the slope data in figure 4.4, the refined pixel population's slope over six runs averages to 4.0127 +/- 0.1200, while the average distribution of pixels within a run generates a CV value of 5.19 +/- 1.25%. The CSD value over the six runs averages to 0.0160 +/- 0.0044, while the average distribution of pixels within a run generates a CV value of 37.1 +/- 8.9%. The CC value over the six runs averages to 0.9966 +/- 0.0017, while the average pixel distribution generates a CV value of 0.24 +/- 0.12%, forming the most tightly distributed line feature both within a single calibrations pixel population, and between multiple calibrations. The opposite is true of the RE value, with an average from the six runs of 7.02 +/- 4.22%, and the widest distribution by far at 271 +/- 221%. No consistently observable pattern appears in trying to correlate one feature to another (e.g. for run 2, low CSD mean value vs. low RE mean and SD; for run 4, low CSD mean value vs. high RE mean and SD). Thus by taking the mean values and measuring the magnitude of each features distribution, post CSD filtering of the population, it does not appear that any predictable trend in performance, and that these levels of variation must be attributed to the nature of each distribution. To investigate this further the distributions have been plotted as histograms (see figure 4.5, and appendix 1 for full

list), where based on the data in figure 4.4, comparisons of pixel CSD response are contrasted in fuller detail.

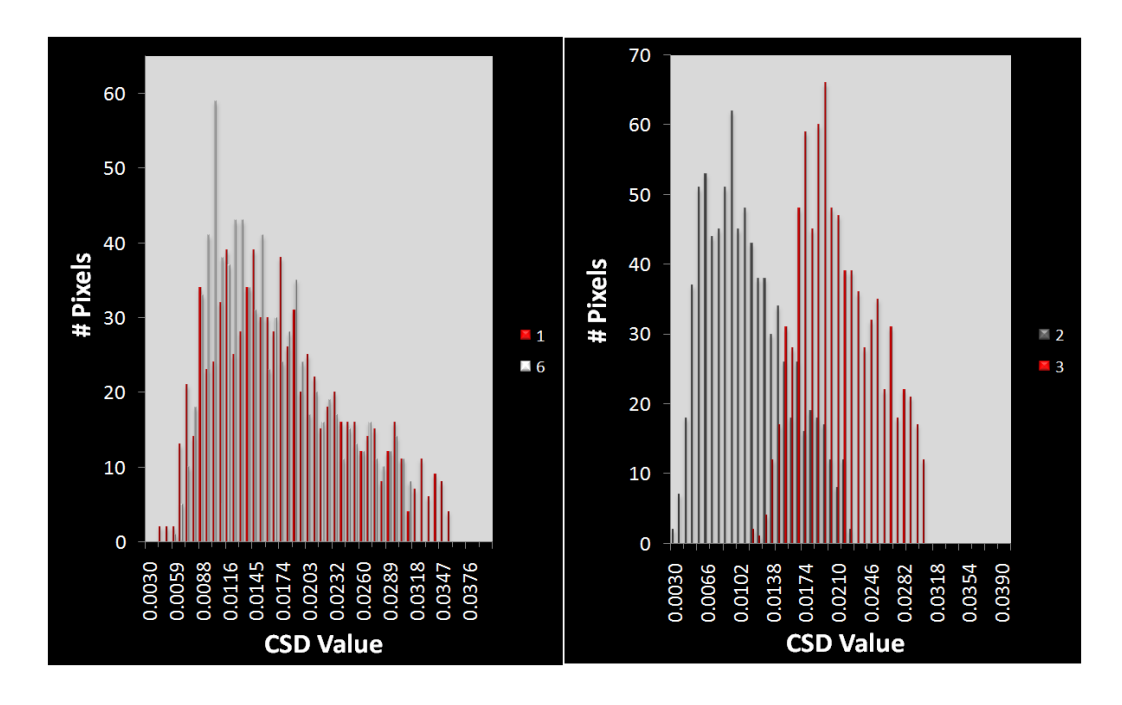


Figure 4.5. Histogram representations of CSD distributions for the NaN_3 aqueous calibration standards (0.010-0.200 M); left graph comparing run 1 to run 6, right graph comparing run 2 to run 3. Each run has had 20% of high CSD pixels removed prior to plotting.

The CSD distributions in figure 4.5 were selected to illustrate two phenomena seen regularly with any feature of the pixel population (slope, CC, RE, noise). Runs 1 and 6 give nearly identical distributions — one overlays the other, and their descriptive statistics confirm this similarity; keeping in mind that these two runs were run the farthest apart in time, with different calibration sets. Runs 2 and 3, each run out of the first trial calibration set (as with run1), are shifted quite significantly relative to one another, where run three appears to have a narrower distribution compared with the more positively skewed distribution of run 2. It appears that the CSD pixel filter has affected run 3 more than run 2, as the distribution appears unnaturally 'cut' on the high end — this does however create a more normal type distribution of the pixel CSD response, and the CSD CV is a more relevant measure of highly skewed distributions like the CSD and RE, but not of the 'normally' distributed pixel slope and CC values.

	$\%\text{CV}_{\text{median}}$	%CV	
CSD	39.88 +/- 9.30	37.09 +/-8.29	
СС	0.24 +/- 0.12	0.24 +/- 0.12	
RE	474 +/- 483	271 +/- 220	

Table 4.3. CV_{med} vs. CV for distributions of pixel calibration features as an average of the six runs.

It was hoped that the modelling of the pixels with multiple standards would lend stability to the predictive powers of the pixel population – i.e. the building of multiple points within the pixels response, then eliminating 20% of the pixel population based on CSD performance, and calculating the remaining population as the 'average' pixel. Contrary to expectation, a wide distribution of predictive accuracy is obtained from the pixel array (see %CV_{med} for RE, table 4.3). Also, it appears that significant shifts take place with all features of the pixel population going from one day's analysis to the next. The only variables between runs that can be identified are a) the recalculation of the NUC, and b) the slight shift in the detector integration energy between runs. The latter is unlikely to be the main issue, as in section 3.4.1 dealing with noise characteristics of the FPA the impact of integration energy was found to have minimal impact on the distribution mean/magnitude above a value of 6000. On a positive note, the predictive accuracy, as shown in the RE plot of figure 4.4, highlights that runs 1, 2, and 5 have generated a significant pixel population with a RE below 5%, and further that these same runs generate an average of ~150 pixels with an RE less than 1%. No correlation was observed with any of the other linear regression parameters and the higher accuracy pixels, suggesting that they may simply be due to random response - i.e. perhaps any pixel will by chance generate this accurate response.

Runs 3 and 4 had an expanded analysis of a single standard, i.e. one sample from within the curve was scanned repeatedly while building the calibration. Using this data, the stability of the pixel RE of prediction can be estimated, an also the data can be plugged into calibration sets from other days to see how cross prediction is handled. Rather than applying a CSD filter to the pixel data (which has varying levels of effectiveness in narrowing to the better RE pixel population), a direct RE filter was applied, by removing pixels based on their mean RE over the 12 replicates. The effects of

a CSD FPA filter vs. a direct RE FPA filter are shown for two series of 12 replicates (figure 4.6, below), each performed on the same calibration set within one day of each other.

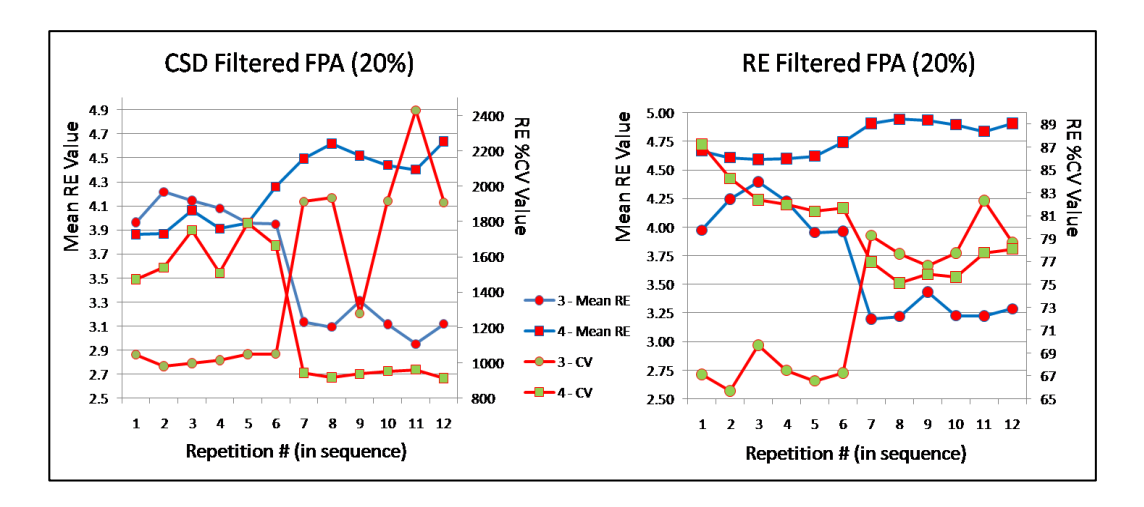


Figure 4.6. Two calibration sets are plotted for 12 repetitions (x –axis), showing the mean of the pixel populations RE value, and the associated CV value for that population. A CSD filter was applied in the chart at left, an RE filter at right – each removing the 20% of pixels with the highest respective value.

Going from the CSD filter to the RE filter does not show drastic changes in the mean RE values for the remaining pixel populations, however the CV values are significantly reduced with the RE filter approach. This illustrates the inefficiency of the CSD filter in obtaining those pixels with better predictive ability. The other observation is the magnitude of the variability in pixel response, i.e. looking to the RE filter data; the same sample may generate a relatively tight range of mean RE values, however the distribution of pixels from replicate measurements can have a standard deviation fluctuate from 65-85% relative to the mean — with no changes in operating conditions. Looking at a single pixel (5 x 21) in run 3 for the 12 repetitions it generates a mean RE of 0.66 +/- 0.47%, while in run 4 it generates a mean of 1.83 +/- 1.21%. This pixel was selected as the best performing in terms of RE value from run 3, to show what level of variability might be expected from the best crop of pixels.

4.3.2 Milk Calibrations: MLR and PLS Modelling of FPA Pixel Population

The linear regression modelling of NaN₃ has demonstrated the Beers law limits for the pixel population. Linear regression is rarely directly used in the modern application of spectroscopy for quantitative measurements; however it does form the fundamental backbone for more intensive calibration methodologies. It is suspected, based on previous accounts and knowledge of the complexity of the sample matrix, that modelling one component off a single peak will not provide the best accuracy in analysis, i.e. other components of the milk will contribute to a peak selected as representative of a single component, attenuating the end result to an extent. Figure 4.7 shows the optical image of the homogenized milk standards under the microscope, where droplets are visible in the stopped flow but in a size that does not impact the response of the FPA's significantly. The milk scanning procedure was optimized at 40°C as a stopped flow, with check valves on the input and outputs to ensure that a drift of the sample didn't occur during sampling – so any features that might be detected as heterogeneous by the FPA would be static throughout the scanning procedure.

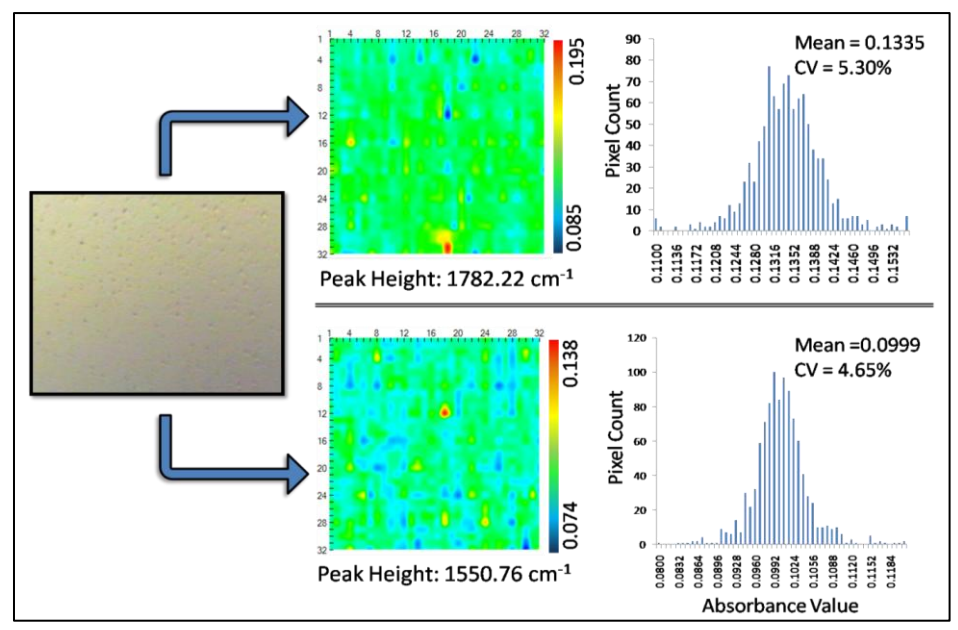


Figure 4.7. At left, an optical image of the FPA field of view of a stopped flow of homogenized milk. Middle top, IR map of the C=O stretching frequency indicative of the fat distribution; middle bottom, IR map of the Amide II peak indicative of the protein distribution. Right, respective histograms of absorbance values per pixel for the C=O and Amide II measurements, where the peak heights are baseline corrected at 1780.0 and 1490.0 cm⁻¹ respectively.

	Fat (174	Fat (1747.5 cm ⁻¹)		NaN3 (2048.4 cm ⁻¹)		
Statistic:	a	b	a	b		
RE	4.01 (101)	2.68 (68.6)	1.01 (80.1)	0.83 (67.6)		
CSD	0.0049 (11.6)	0.0053 (21.3)	0.0099 (38.0)	0.0112 (61.1)		
СС	0.9967 (0.07)	0.9961 (0.19)	0.9990 (0.08)	0.9985 (0.28)		

Table 4.4. LR-analysis of fat content and NaN_3 internal standard from milk calibration standards. Under each category (fat and NaN_3) a = 20% pixels removed based on CSD; b = 20% pixels removed based on RE. Values in brackets are the %CV for the remaining pixel population.

As an initial comparison to the previous section a calibration set was run with the addition of a NaN₃ spikes in increasing amounts, creating another component in the milk calibration set. This added standard established that 1) the milk matrix does not significantly impact the modelling of NaN₃, and more importantly 2) the principle components of milk are not modelled as efficiently as the NaN₃ case. Table 4.4 actually shows the superior linear regression for the NaN₃ component where the CSD for NaN₃ is nearly twice that of the respective fat values, while opposed to this the CC values are slightly improved over that of the fat. Between the two cut-off approaches (CSD and RE removal of pixels) the RE filter results in the best population of pixels in terms of RE and a similar selection in terms of CSD and CC, although they are in each case slightly degraded when compared with the CSD filter. In relation to the previous NaN3 calibrations performance is improved, noting that the collection of the milk standards was done at 256 scan co-additions vs. the 64 scan co-additions used in the previous NaN₃ work, illustrating the gains in predictive accuracy to be had with longer scan times. The best performing pixels, as selected with the RE filter in table 4.4, obtained an average prediction of fat content within 2.7% of the true value and a distribution magnitude among these pixels comparable to the NaN₃ in the same standard. It is also noted that the minimum absorbance at 1747.5 cm⁻¹ for the standard set was subbaseline with a CV of 90%, while the maximum absorbance was at 0.14 with a CV of 5.6%. These low end measurements are problematic, as the transmission cell pathlength cannot be extended much further past the current 35 um without further saturation effects due to the water bands. However, this work demonstrates that it is possible to make reasonable calibrations (comparable to the optimum range NaN₃ measurements

made earlier within 0.2 -0.8 absorbance) on the low end of the absorbance scale for the detector elements of the FPA camera.

Due to the linear regression calibration approaches inability to model the contributions between separate components within the milk matrix to each peak (which with the LR model are being analyzed as an individual component) the MLR calibration technique is often used for making quantitative measurements of milk in industry. MLR attempts to model the relationship between two or more explanatory variables and a response variable by fitting a linear equation to the observed data. The application of MLR to the FPA milk calibration standards also allowed for the direct comparison of results to the requirements of the AOAC for milk measurements (table 4.5, bottom row). The selection of peaks was based on early research with the assessment of FTIR for milk analysis ⁵⁰ (see experimental for details) and focused on the reference analyzed components of the milk standards (fat, protein, and lactose). The data in table 4.5 relates to the MLR calibrations made on a) the averaged peak responses for all pixels, b) the averaged peak responses post removal of the 20% highest RMS noise pixels, and c) the averaged peak responses post removal of the highest CSD pixels based on previous LR analysis per pixel.

	Fat		Protein		Lactose	
Pixels:	R ²	CSD	\mathbb{R}^2	CSD	\mathbb{R}^2	CSD
All	0.9945	0.1008	0.9961	0.0058	0.9940	0.0086
RMS (20%)	0.9944	0.1015	0.9928	0.0079	0.9974	0.0057
CSD (20%)	0.9960	0.0855	0.9929	0.0078	0.9946	0.0081
CSD (50%)	0.9976	0.0670	0.9954	0.0063	0.9955	0.0074
CSD (80%)	0.9980	0.0604	0.9962	0.0058	0.9945	0.0082

Table 4.5. Trending of MLR fit statistics upon furthered refinement of pixel population contributing to the average values used for calculations. RMS (20%) indicates removal of the highest 20% RMS noise from 1950-1750 cm⁻¹ based on image blanks; CSD (%) indicates the level of pixels removed based on individual pixels CSD from a precalculated linear regression.

The data in table 4.5 contrasts the fit statistics for the different approaches to pixel population refinement, and based on previous experience with the linear regression data, it would be expected that the CSD refinement approach would generate more significant improvements. For the fat this assumption holds true, with virtually no improvement to the fit statistics upon RMS refinement, and proportional improvement

with CSD refinement. The protein fit statistics see degradation upon RMS refinement, and a similar situation with the CSD refinement – until 80% removal of pixels which equates the average when using the average of all pixels. The lactose shows better improvement using the RMS approach compared with the CSD approach.

The data in table 4.5 is based on a single calibration run, while it is noted that in general for repeated runs, there is an improvement in the fit statistics based on the CSD approach for the fat and lactose components, while the protein component generates more variable results. It is also noted that for each scenario it doesn't appear that a terribly significant improvement or degradation is taking place with the fit statistics in the MLR model - however it needs to be demonstrated to what level are these pixel populations are performing compared with industry standards. To do this the MD_a, SDD_a, MD_r, and SDD_r were calculated based on the MLR curves predictions of the known standards values, and the results tabulated. As a first observation, it was found that the MD_a and MD_r in all cases were in the order of $10^{-6} - 10^{-7}$, well below the requirements of the AOAC for this parameter. However as indicated by the higher values of the SDD_a and SDD_r these extremely low MD_a values can likely be attributed to the noise level of the data set which makes it appear as no bias exists; therefore the values are better described by the SDD_a and SDD_r in this case. The nature of the detector at hand (FPA camera) explains this observation of noise drowning out observable bias in the mean differences, as it's noise levels are 1-2 orders of magnitude greater than conventional IR detectors.

In figure 4.8 (following page) the trends in the SDD_a and SDD_r are plotted for the varying levels of pixel refinement (based on the CSD values of the pre-linear regression selection of pixels), and several things can be noted about these trends. In each case there is a reduction in the absolute value of the SDD_a upon the initial levels of refinement – and in most cases this reduction is proportional throughout the successive levels of refinement, thus validating the procedure of pre-selection of pixels based on their LR CSD (or R²) values. For the SDD_r – an overall reduction in the absolute value for the two calibration sets does take place. The exception here is the lactose SDD_a, which appears to not generate any significant change with further removal of pixels (note the scale of the lactose SDD_a in figure 4.8). It was hoped that the refinement of pixels might narrow the gap between respective calibration sets, but this doesn't seem to be a

consistent effect of the procedure; the fat seems to narrow for each the statistics, but lactose is much less predictable, and the protein narrows with respect to the SDD_a but not the SDD_r. The trend of each the SDD_a and SDD_r seems roughly repeatable between runs with different calibrations in that similar patterns can be discerned for the pixel refinement procedures. Overall the changes in the statistics are not that great proportional to the level of pixel refinement, and are generally greater with respect to the fat and protein components than with the lactose – but as described below these small changes can have an important impact.

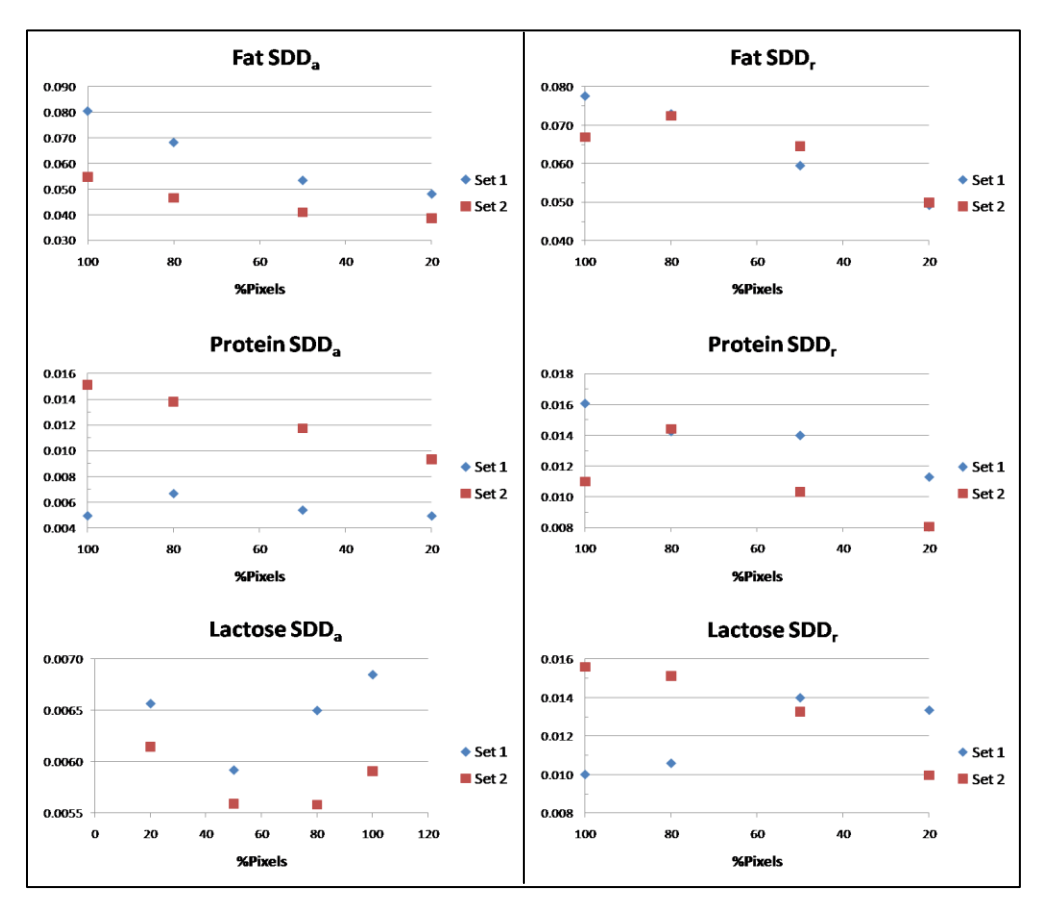


Figure 4.8. Trending of SDD_a and SDD_r for two sets of milk calibration standards. The SDD_a is for a set for individual calibration runs from two separate sets of standards. SDD_r is representative between two calibration runs per set – i.e. the differences between the repetitions of the same standards. The successive levels of pixel refinement based on their pre-calibrated CSD values is represented on the x-axis, while the SDD_a and SDD_r are represented on the y-axis of the respective charts.

With respect to the industry standards as defined by the AOAC, the lactose and protein components are predicted with enough accuracy and repeatability by the FPA to

be acceptable. The problem lies with the fat component, whereby both the SDD_a and SDD_r statistics have not met the standards (0.06 and 0.02 respectively); the SDD_a is quite close and with refinement can meet the standard – but the SDD_r is well off, and even with removal of 80% of the worst performance pixels. It is noted that an attempt to model the fat component using only the CH band (2924 cm⁻¹), only the ester band (1747.5 cm⁻¹), and a combination of both – where it was found that inclusion of generated the optimal result.

As a final illustrative measure, the pixels of the FPA were calibrated for the milk components using a PLS approach. This feature was incorporated into the same software used to generate the linear regression calibrations, and allows for the generation of the same 2D image plots of the resultant response distribution (figure 4.9). The RMSECV distribution gains for each parameter are demonstrated in figure 4.10, with increasing levels of latent variable fitting.

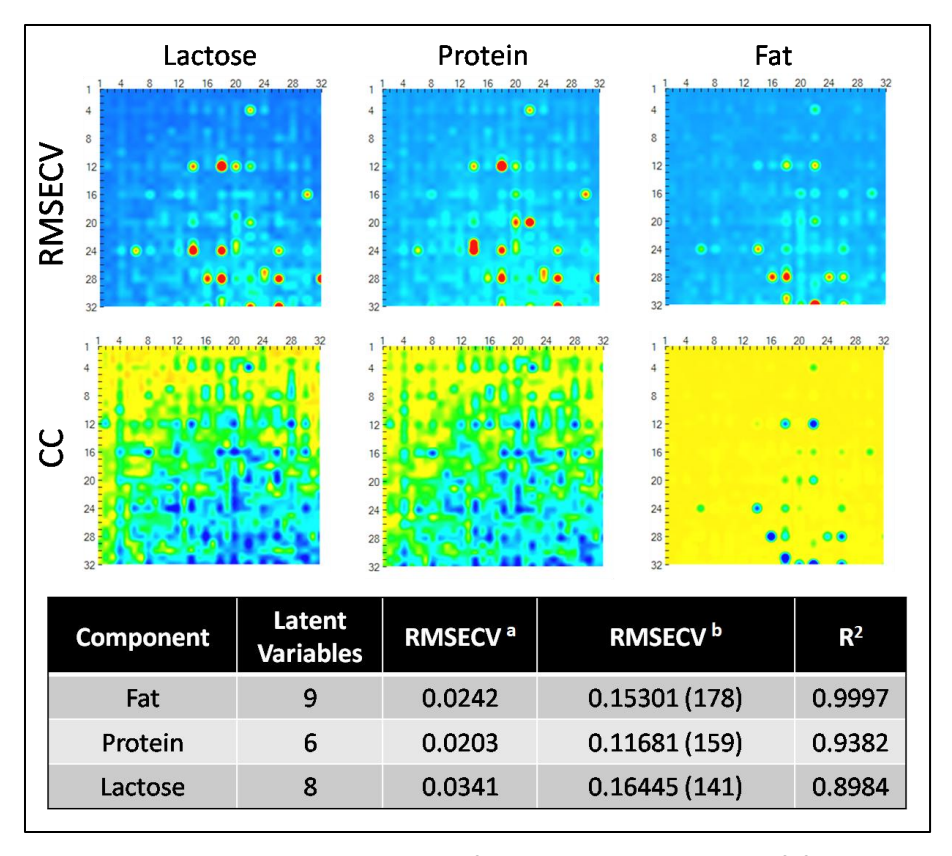


Figure 4.9. RMSECV and CC distributions for the PLS calibration of fat, protein, and lactose. Inset table shows latent variables selected from respective PRESS plots, ^a the RMSECV for the FPA as a whole (per component), ^b the RMSECV with CV in brackets for the pixel population, and the FPA average R² value.

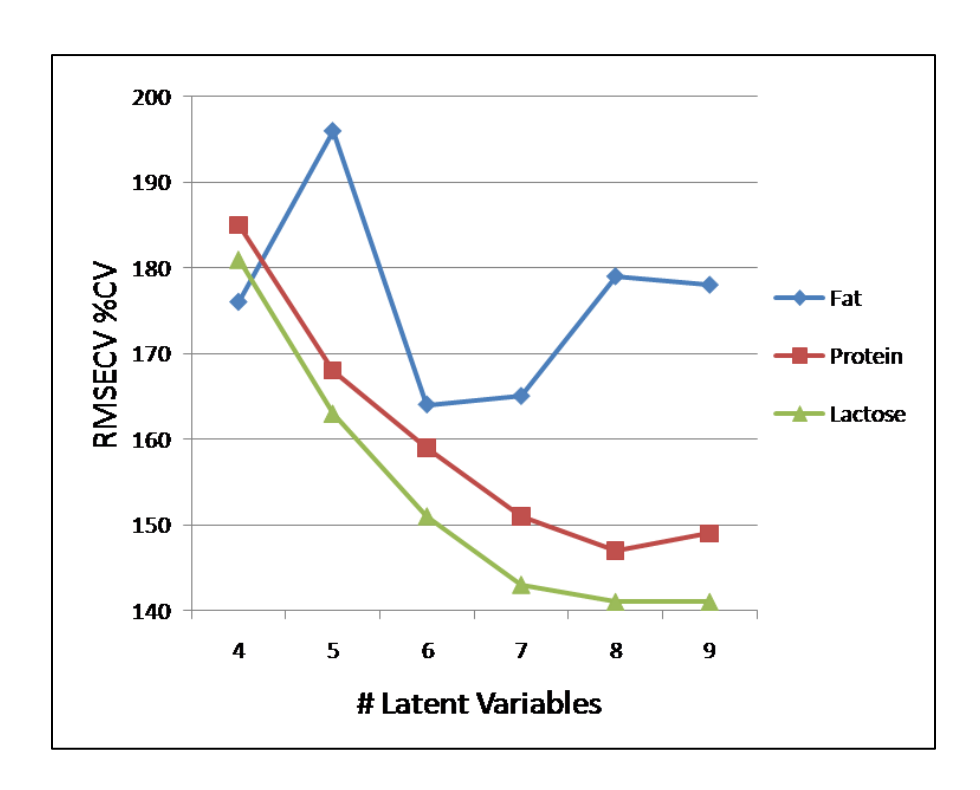


Figure 4.10 The level of RMSECV distribution versus the number of latent variables used in the PLS calibrations of fat, protein, and lactose.

4.4. Conclusions

The overall linear response of the FPA compares to that of the DTGS standard detector type used in many conventional FTIR spectrometers, however upon breakdown of the FPA into its constituent detector elements there is a rapid degradation in the linear regression performance. Taking the data in chapter 3 (about the RMS noise features) into account, it appears that the same spatial features are present for the slope, CSD, and R² performance characteristics of the detector elements. A filter removing the 20% highest RMS noise pixels from the calibrated pixels supports this observation in that there is a significant tightening of the response distributions (slope, CSD, and R²) and an improvement in the absolute means of the average detector elements CSD/R² values relative to the DTGS detector (CSD, 0.0169 vs. 0.0044; R², 0.9912 vs. 0.9996 – for the top 10% pixels vs. the DTGS detector). For each parameter it was found that for the initial 20% filtering the gains in further removal of pixels based on their noise features did not result in significant gains in global performance, and that looking at the pixel population as a whole no strong correlation actually exists between noise and linear regression parameters of the pixels.

Other more direct methods were thus experimented with, and it was demonstrated that in terms of selection of pixels with better predictive ability (in terms of %RE to the true value of the selected standard) the CSD and CC filters gave the best result aside from the direct %RE filter. In practice this would require that a pre-calibration be performed on the FPA prior to the analysis of a sample set, and from that information the pixels to be used in the analysis may be selected based on any of the pixel selection filters used here, with the recommendation of a direct %RE and a CC filter to remove at least the worst 20% performing pixels. It is interesting to note that the RMS noise filter approach is the least effective of the pixel filters employed, and actually results in an increased average %RE prediction value with a broader distribution over the FPA suggesting strongly that the noise features of the pixels cannot be the only consideration in determining the best 'quantitative' pixels. The day to day calibrations using the above model, found that the stability of each measurement is hard to predict – the average CSD value can double from one day to the next, with the magnitude of the distribution changing just as drastically - the same can be said for other calibration features. Thus it appears that differences from one FPA NUC and other spectrometer conditions have an unpredictable effect on the overall FPA response, stressing the requirement for a pre-calibration before each day's analysis. It is troubling that after modeling the pixels responses with multiple standards, and then making validation predictions based on that model, that such a wide range of predictions are still generated - and this again is likely due to the nature of the NUC performed on the detector elements giving unpredictable behavior for a good proportion of the pixel population.

The analysis of the milk standards provided an important addition to the NaN₃ calibrations in that it allowed for comparison to industrial requirements of quantitative performance, and also allowed for the performance of the FPA detector to be pushed with the multi-component analysis of a more challenging sample matrix. The homogenized milk samples did not have any observable features under the microscope. The utilization of a pre-homogenizer is required for all milk sample analysis by IR spectroscopy, and while this is not a problem to link to conventional transmission IR cells, it is envisioned to be problematic in coupling to the proposed multi-channel cell discussed in chapter 5. Overall, the linear performance for each of the protein and

lactose components of the reference analyzed milk standards met the requirements of the AOAC, while the fat component was not able to pass. The direct comparison of the fat component to the NaN₃ regression statistics shows that the performance of detector population is diminished – something that is improved when using the MLR calibration. The PLS calibration of the milk standards did not meet expectations – the RMSECV for the calibrations were a two orders of magnitude greater than the linear regression analysis, while contrary to the MLR results the fat component had the best relative performance with poor performance for the protein and lactose components. The same spatial features are observed within the 2D plots of each of these features, suggesting that the PLS approach does not compensated for this feature of the FPA.

Overall, it has been demonstrated that the FPA pixel population is capable of making milli-molar accurate predictions of the NaN₃ model system, and a percentile level of accuracy with the measurement of milk components. There is the continuation of the spatial features seen with the noise analysis, and pixels can be better selected by using the parameters obtained from a pre-calibration procedure. The spread of the pixel predictive ability seems to change from one day to the next and necessitates constant monitoring – i.e. transferability of a calibration model from one day to the next should be cross checked with calibration standards upon every analysis and the pixel population to be used based upon the result. The level of variability for an individual pixel performance needs to be contrasted to the level of variability between pixels, where it is a combination of these two factors that will decide how one might make predictions of a concentration gradient within a single image – rather than for a series of images as done in this chapter.

Chapter 5. FPA-FTIR Multichannel Sampling System.

5.1. Introduction

To define the concept of high-throughput analysis (HTA) is simple enough - where any process which enables the analysis of a high volume of samples in an efficient amount of time, obtaining the required level of analytical information can be called a high-throughput technique. These HTA techniques are of great significance in industry for the analysis and/or screening of products at different points of their production process for quality control and regulatory purposes. There has been a trend in recent years toward the development of these so called high-throughput chemical analysis techniques, where one of the main driving forces behind this trend is that of the pharmaceutical industry and combinatorial chemistry 96. The drive for new drugs discovery requires the analysis of countless thousands of formulations under a variety of experimental conditions, and carries with it a large monetary incentive. One technology which has revolutionized the field of high throughput drug discovery is micro and nanofluidics, where the massively parallel sample throughput of these arrays allows for unprecedented levels of high throughput screening (HTS). Both FPA-FTIR imaging and micro-fluidics are beneficial to a variety of other fields for the purposes of HTA and HTS, e.g. biological sciences ^{120, 121}, medical sciences ¹²², pharmaceutical sciences ¹⁰⁶, forensics science ¹²³, and food and agricultural sciences ⁸ all stand to benefit from these advances in one way or another. As discussed in the microfluidics section of chapter 2, there are many means of detecting processes on micro-fluidic platforms – LIF, SERS, thermal lens spectrometry, and a variety of other exotic sensor techniques – but what is proposed by some is that perhaps that old familiar FTIR is up to the task. With its multiplexing capabilities, where the rapid collection of a wealth of spectral information occurs quite rapidly, FTIR makes for a very powerful analytical tool. It is adaptable to micro-fluidic systems, in that many of the typical dimensions utilized (10's of μm) are characteristic of conventional transmission FTIR measurements, while the ATR sampling accessory allows for measurements of even smaller fluid sample thickness (on the order of a micron). There are limitations to the applicability of FTIR to micro-fluidic systems, mainly: spatial resolution limitations due to the diffraction limit of IR radiation ($^{\sim}\lambda$), and the beam size of conventional FTIR systems is too large to make useful measurements of a microfluidics system, making an IR microscope accessory essential.

The approach to HTS-FTIR spectroscopy undertaken with this chapter incorporates the FPA-FTIR detector - in other words a multichannel detector, with a novel IR transmission sampling cell. FPA-FTIR for HTS analysis is not a new concept; however it is hardly the main application focus of the detection technology. Many studies have used the technique for the measurement of multiple deposits and a few have used the system for making measurements on micro-fluidic systems 96, 105, 124. The current multichannel cell has been micro-fabricated using photolithographic techniques to create a series of parallel channels, capable of passing several fluid streams within the field of view of the FPA detector. The streams are completely separated by polymer divisions, and each will encompass several rows/columns (dependant on orientation) of the FPA detector elements. This arrangement works around the two limitations of FTIR spectroscopy to the measurement of micro-fluidic systems in that the individual detector elements are capable of sampling in the range of a few micrometers with the help of the IR microscope optics. Additionally, the detector array allows for the sampling of multiple fluid streams simultaneously, and because it is an FTIR spectrometer, multiple components from each of the streams may be measured simultaneously as well. This system provides a very high throughput analysis tool, adaptable to many fields. The model systems used in the following experiments evaluates the feasibility of passing multiple fluid streams with the current cell design, and performs experiments to test the potential quantitative abilities of the system. As each of the systems has been designed as prototypes, recommendations will be made based on the results obtained for future developments.

5.2. Experimental

5.2.1. Materials and Equipment

Micro-fluidic multichannel cell: The cell was constructed using photolithographic techniques, with an SU-8 negative resist upon a CaF₂ substrate; see reference for details of the process. The end design of this multichannel cell was to be a demountable design that could be taken apart repeatedly in order to deal with an blockage issues that may occur during sampling, thus the CaF₂ plate with the multichannel features was placed against another cell (same dimensions) that had been drilled to have a hole matching each of the inputs/outputs of the multi-channels. The drilled and undrilled CaF₂ plates were then manually aligned and fastened together for sampling using a custom made manifold.

Multichannel cell manifold: The multichannel cell required a new manifold design in order to utilize each of the channels as a flow through transmission sampling device. Decagon geometry was used, consisting of a fluid input plate and a fixing plate used to sandwich the micro-channel and drilled CaF_2 crystal plates together. The fluid input plate had four of the sides used for inputs, then an empty side on each extremity of the inputs, and the other four sides used as outputs – the drilled CaF_2 plate was aligned with the input/output ports on the bottom side of this plate. The transmission port of the cell was coned from a diameter of 1.2 cm down to 0.4 cm at the CaF_2 plate side, in order to minimize the stray light passing through the sample, and to maximize the contact of the manifold with the multichannel cell. Each input/output had a male luer lock input inserted to attach the tubing assembly, which in turn was connected to a syringe pump (SyringePump NE-1800) capable of achieving the μL/min flow rates used in experiments. Each syringe was linked to a 0.45 μm milli-pore filter to ensure any remaining particulate in the standards/samples was removed prior to passing through the 30 μm bottleneck of the multi-channels.

5.2.2. Samples

Samples consisted of the NaN₃ standards used in chapter 4, prepared by weight, and stored in Teflon capped amber glass ware at room temperature. Additional samples of ethanol/water solutions were prepared for testing the level of viscosity on the loading of

the system – however these were not prepared with quantitative measurements in mind (not calibration standards). The channels themselves provided a sample for spectroscopic interpretation, with the SU-8 polymer deposition thickness over the features of the channels.

5.2.3. Data Acquisition and Processing

The open beam FPA NUC was carried out, followed by an open-beam background collection, whereby the multichannel cell was then moved into position using the optical microscope for alignment. After placing the multichannel cell and locking it into place, the Lancer calibration window was again opened and the IR microscope sub-stage was used to adjust the response back to a maximum, while the integration time was used to approximate the open-beam NUC calibration energy. Alternative calibration scheme was followed, whereby the multichannel cell was fixed to the stage and the FPA NUC took place through the channel features, followed by a background collection enabling subtraction of the cell features from the subsequent fluid samples. Scans were collected at 16 cm⁻¹ resolution, based on preliminary work demonstrating the gain in FPA pixel noise performance with decreased spectral resolution. The fixing of the multichannel manifold to the stage became of upmost importance during scanning in this mode – as the subtraction pixel per pixel could be impacted dramatically by minor shifts of the apparatus.

5.3. Results and Discussions

5.3.1. Micro-fluidic Multichannel Transmission Cell For FPA-FTIR Quantitative Analysis

The key components for the development of a micro-fluidic multichannel transmission cell are depicted in figure 5.1. The photolithographic fabrication of the multichannel cell was carried out so that one cell contained all of the micro-structured features (figure 5.1A), while the facing cell held the drilled inputs/outputs. This design allowed for the separation and cleaning of the unit if any serious clogging of the system occurred, which was a continual problem with previous work using a sealed cell approach. The two cells were fixed using the pressure supplied by the custom designed manifold (figure 5.1B). The port of the manifold for transmission of the FTIR beam line was optimized in order to maximize the surface area of the IR crystal contacted by the manifold while still letting a sufficient amount of energy to pass onto detection. With the tubing assembly fixed to the micro-channel manifold (figure 5.1C) and the pumping system connected to the tubing assembly (figure 5.1D), the system was ready for sample collection.

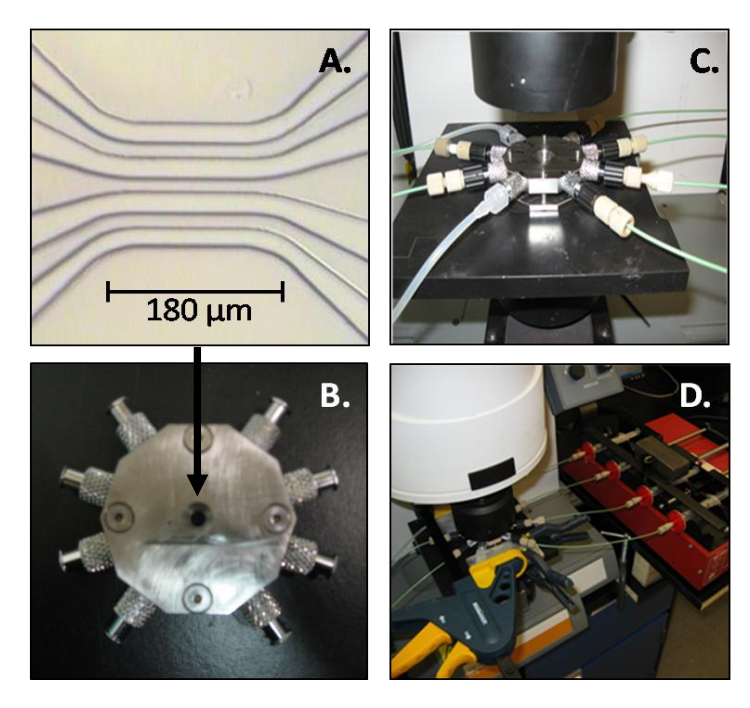


Figure 5.1. Multichannel sampling apparatus. A. SU-8 micro-channel structures on a CaF₂ substrate; B. Custom transmission cell manifold for multichannel assembly and sample loading; C. Constructed multichannel mounted to tubing assembly D. Pumping assembly fixed to stage-locked multichannel cell.

The main issues with the development of demountable cell design lie with the manual construction of the cells within the manifold. A practical means of assembling the system would have to be developed if it hopes to be used for more routine analysis – any small misalignment of the drill holes with the micro-channel fluid inputs/outputs results in an inoperable cell, i.e. fluid cannot be passed using the current design. It is also noted that the reassembly of the cells carries with it a high degree of risk as far as polymer delamination is concerned – particularly if the cell manifold has been wetted. Thus the benefits of having a cell design that is demountable for cleaning/de-clogging purposes are countered to a certain extent by the extreme sensitivity of the system upon repeated handling.

The loading of the cells using the syringe pump was the other main issue around the sampling of the multichannel system. It was found that flow rates greater than 100 µL/min resulted in the stalling of the pump array, while at lower flow rates leakage from the manifold fittings was a constant issue. Generally the lower the flow rate the better the performance, but this has definite practical limitations – i.e. the high throughput sampling of such an assembly would call for the rapid loading of the cell. A flow rate of 20 µL/min was settled on as a compromise, however regular leakage still occurred. Often the loading of only 2-3 channels would occur, followed by a backwash when the fluids were not able to pass through the output side of the cell. Most of these issues can be attributed to the high pressures involved combined with the small misalignments of the two cell plates with one another – again emphasizing the need for a more efficient means of assembling the cells. The successful loading of the cells was achieved for the collection of several spectra, however the repeatability of this was poor, and in the end more time spent on unsuccessful construction of the cells within the manifold than with obtaining useful spectral data of fluid samples.

Due to the need to keep a micrometer level of precision within the field of view the fixing of the multichannel cell manifold to the microscope stage formed an important part of the analysis – and proved more challenging than was initially expected. Due to the level of vibration introduced by the syringe pump through the tubing assembly, a certain level of strain was put onto the manifold when it was clamped into place. By securing both the syringe pump and the micro-channel manifold it was possible to obtain the required level of stability, although the current arrangement shows that

there would be a need for a special container upon the microscope stage that would allow for the easy locking of the multichannel cell manifold into place for scanning – precise enough to guarantee micrometer level repeatability of placement, allowing for a higher level of confidence in the transferability of a background scan of the multichannel features (i.e. an FPA pixel always samples an identical position).

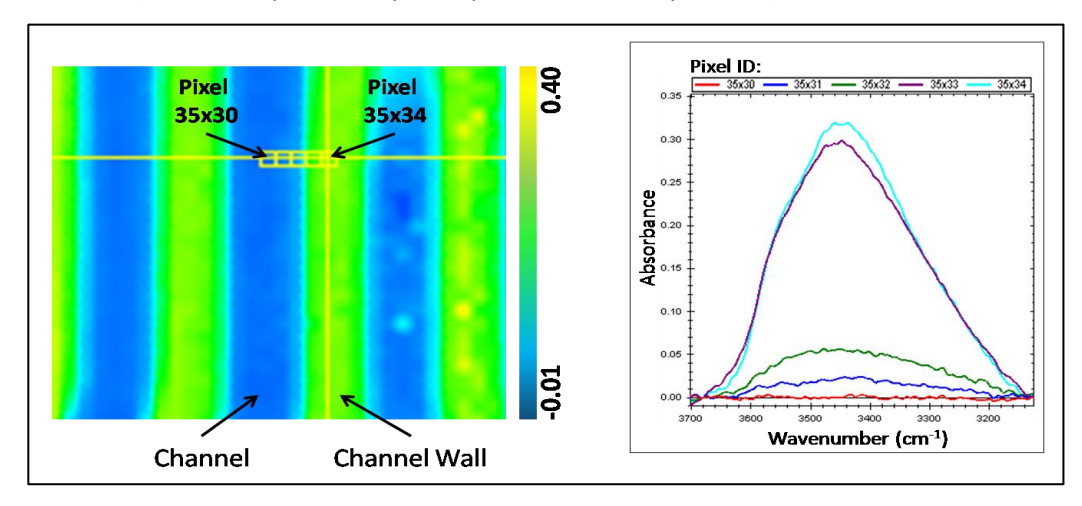


Figure 5.2. FPA-FTIR image of the empty multichannel cell, showing the pattern of SU-8 polymer within the cell. Left, 2D image for the intensity of 3420.0 cm⁻¹ of the SU-8 polymer. Right, blue spectra is from within a channel structure, red spectra from within channel wall (yellow blocks indicate selected pixels).

The data shown in figure 5.2 shows a scan of the multi-channels obtained against an open-beam NUC FPA and an open-beam background, in order to illustrate the features of the channels. The modelled peak area is characteristic of the SU-8 polymer used to create the micro-channel structures, where it generates a strong response in the fingerprint regions up to approximately 1600.0 cm⁻¹, and also from 2800.0-3700.0 cm⁻¹. What is hoped is that the developing process during micro-fabrication will eliminate the majority of the polymer within the desired channel structures, however what is found is that a significant residue remains at all points of the channels (see the blue spectra in figure 5.2). It is actually noted that due to the curing process of the exposed polymer, slightly different spectral features exist within the residual, i.e. a stronger slope riding from 1600.0-1800.0 cm⁻¹, and a weak broad response from 1900.0-2400.0 cm⁻¹. It is also noted that there are no sharp edges observed within the 2D image, where a gradual decrease in the polymer signal intensity is observed when tracing from a channel wall into a channel that rides over a minimum 2 pixel width. The obvious consequence of this residual polymer is that it will likely compromise measurements made in the affected

spatial-spectral regions, depending on the ability to compensate by spectral subtraction (figure 5.3). Three background collection approaches have been attempted and their results illustrated in figure 5.3 using different combinations of FPA NUC and background ratios. It can be seen from figure 5.2 that channel regions exhibit different levels of SU-8 residual – the lighter blue versus darker blue within the channels, thus the success of each approach in figure 5.3 is dependent upon the secure positioning of the cell within the FPA field of view.

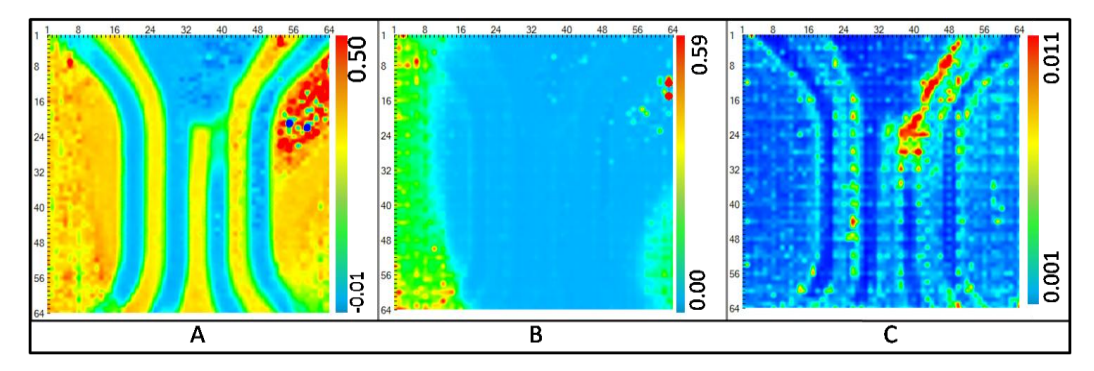


Figure 5.3. Scanning of empty micro-channels: A. Open-beam NUC and open-beam background scan of micro-channel structures, imaging peak height at 3420.0 cm⁻¹; B. Open-beam NUC and micro-channel background scan of micro-channel structures; C. Micro-channel NUC and micro-channel background scan of micro-channel structures. B and C are imaging RMS noise of 1st derivative from 3800.0-3200.0 cm⁻¹.

The multichannel background images are modelled differently than the open-beam background image, in that rather than a peak intensity map an RMS noise map of the 1st derivative spectra is used. This was done due to the fact that there was no interpretable peak information in the resultant multichannel subtraction images. The RMS noise analysis of the same peak region allows one to see how well the background subtraction performed. It is interesting to see how the RMS noise analysis is reflected as the visual imprints of the channel structures in figure 5.4 (b & c), where in scheme B the edges of the channel walls appear to generate higher noise, and in scheme C all SU-8 regions appear to generate higher noise.

The advantage of scheme A is that the multichannel cell only need be steady for the duration of the scan collection, whereas with schemes B and C the multichannel must maintain exact positioning in order to ensure correct ratio on a pixel to pixel basis. It is apparent that where the SU-8 thickness is greater a higher level of noise will result upon subtraction. The subtraction differences in scheme B appear less drastic between channel and channel wall, not factoring in the micro-channel NUC creates a patterned trend on the left portion of the FPA altering the color scaling scheme, however it is still seen that the centers of the channels are slightly lower than the channel wall features. Scheme C gives the clearest picture of channel versus channel wall noise features, and also exposes the spatial noise features observed in chapter 3 are quite evident. The overall noise distribution is lower for scheme C; however the majority of high noise in scheme B is seen to be isolated to the left side of the image. Depending on the requirements for analysis, it is recommended that scheme A be used when removal of the SU-8 residual is not necessary, and scheme C if removal is necessary.

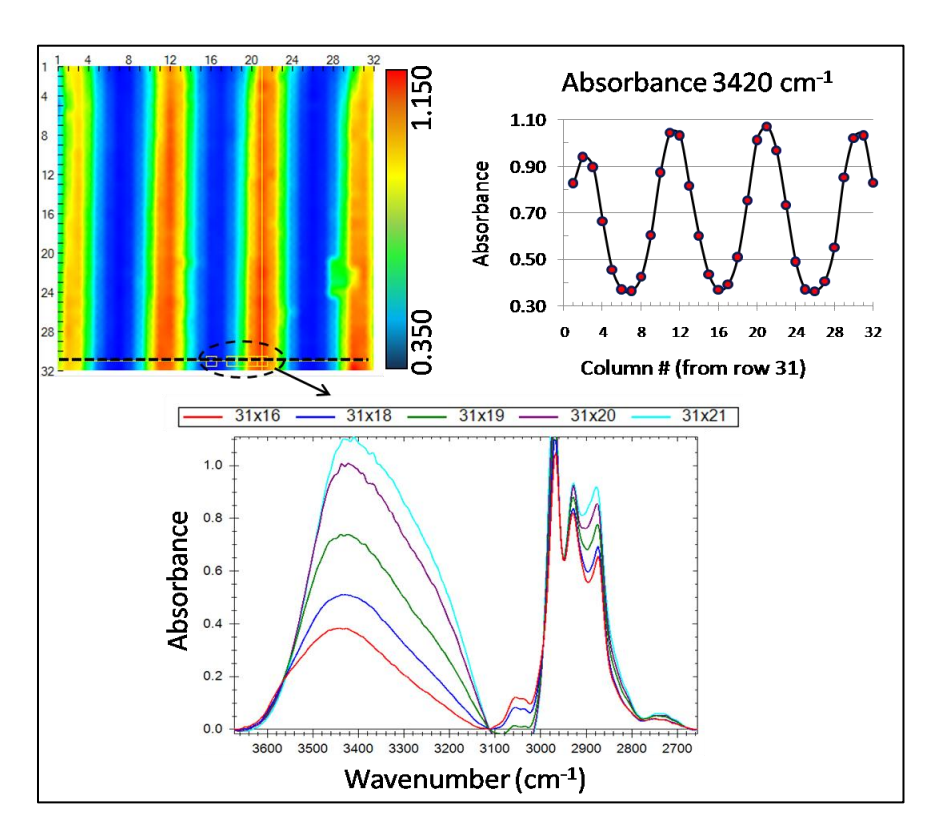


Figure 5.4. IR imaging of ethanol fluid flow through the multichannel structures. Top left, 2D IR representation of ethanol filling channels (modelling peak height at 3420.0 cm⁻¹); top right, profile of ethanol (+SU-8) response; bottom, spectral profile for selected pixels from 2D IR image.

Ethanol was selected as a first sample to test the multichannel cell in terms of loading/pressure/flow rate capabilities, due to its lower viscosity at high concentrations and its relevance to the IR analysis of alcoholic beverage products. Scheme A from figure 5.3 is used in building this image, thus there are contributions from both the ethanol and SU-8 components for the overall response at the broad O-H band running from 3100.0-3600.0 cm⁻¹. Based on the images in figure 5.4 and 5.5 it can be safely assumed that a transition is taking place in the green regions of the 2D image in figure 5.6, where the SU-8 thickness is decreasing and the absorption is due to the presence of ethanol. This is supported in the profile image, where the bottom level of absorbance is equivalent to the maximum level of absorbance of SU-8 in the same cell when empty. There is therefore a profile of sample path-length present in each channel – i.e. they are not rectangular, and the sample absorbance will change depending on where the pixel is taken from within the fluid channel.

Having the presence of a path-length differential within the same field of view for multiple samples (4 channels = potential 4 samples in the current scenario) offers a potential advantage to analysis in that if an sample contains an unknown concentration of analyte the path-length profile gives a wider range of sensitivity measurements much like in the case of the multi-cell accessory in section 5.4.1. When looking to figure 5.6's spectral information for the peak at $3420.0 \, \mathrm{cm}^{-1}$, within the fluid portion of the channel the absorbance measure ranges from $\sim 0.5 - 1.2$, going from the optimum detector element dynamic range to off-scale in a 4 pixel range. The path-length profile presents a problem if simply looking to collect the response from within a fluid – and would necessitate the use of an internal standard when making quantitative measurements using groupings of pixels.

With the idea of utilizing an internal standard and building some data comparable to the previous chapters work, NaN₃ standards were again utilized to evaluate the pixel performance, this time from within a channel. The result in figure 5.7 shows the successful loading of three calibration standards plus on off screen water blank (the water blank was shifted to outer portion of the FPA field of view to maximize the exposure of the other three channels containing the standards). It is visually apparent based on the color scale that a concentration gradient is present going from one fluid channel to the next, illustrative of the increasing concentration standards injected into

each channel. The average response of the centermost pixel rows are shown in the linear regression analysis of the four data points - where they are actually zero corrected against a blank scan of the multichannel in the same position. It is seen that the averaged performance is actually inferior to that of the work conducted in chapter 4, and this is likely due to the interference of the SU-8 residual from within the channels. It becomes difficult to build calibrations between individually selected pixels from each channel, due to the variability already observed in chapters 3 and 4, combined with the added interference of the SU-8 residual, e.g. a range of LR CSD and R² values can be obtained depending on where the pixels are grabbed from within the channel. The distribution of pixel absorbance response is similar to that seen in figure 3.17 (4-6%) and actually looks relatively stable after some light filtering (2-4%). The slope of the 'one scan calibration' does not compare to the slopes built using multiple images of NaN₃ standards, 1.0 - 1.5 versus the 3.9 - 4.2 seen in figures 4.1 - 4.4. This is likely due to a combination of factors between the two methods of calibration curve building. The data for chapter 4's NaN₃ linear regression was built from repeated scans, while the data in figure 5.5 is constructed from smaller groups of pixels within the same FPA image. Where it was seen that the stability of individual pixels is reasonable, the differences between pixels was greater - this then will reflect to a more unpredictable regression when trying to construct a curve from pixels within a single image from the FPA.

Another difference is that the level of integration energy passing through the multichannel transmission cell is about 3000 counts less than with the calibrations built using a conventional cell in chapter 4, thus there is less efficient energy throughput. Several possibilities exist to try and construct calibrations from this data; randomly selecting pixels from each channel, grouping pixels from similar regions of the channel for an average response.

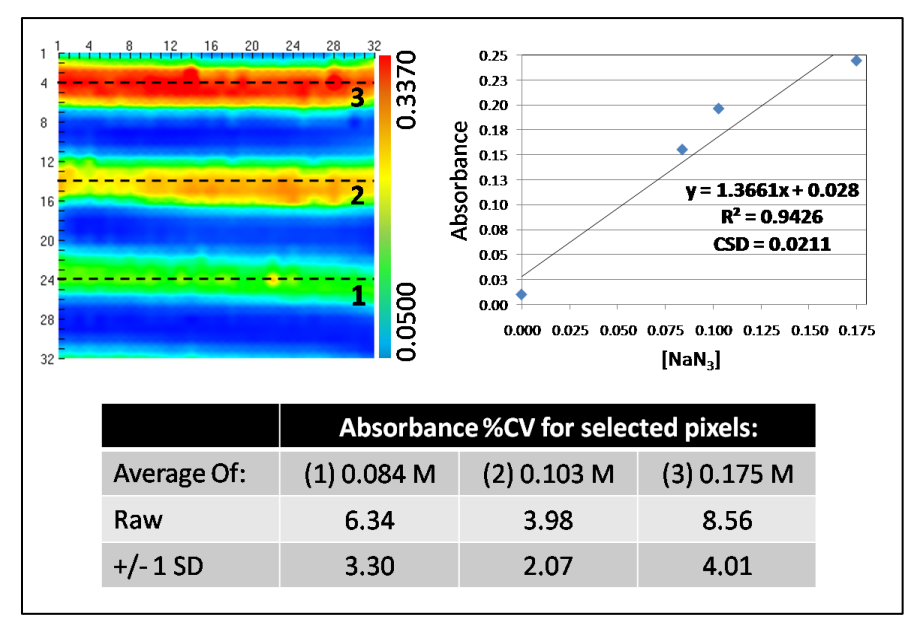


Figure 5.5. One scan calibration model of aqueous NaN_3 within the multichannel cell. Top left, IR 2D image of the three fluid streams numbered 1-3; top right, calibration statistics using the average of the highlighted rows in the 2D image; bottom table showing the distribution of pixel absorbance for the selected rows with their associated concentrations.

5.4 Conclusion

The utility a novel micro-fabricated (photolithography, SU-8 negative resist) multichannel transmission cell has been evaluated. The cell design was built to be demountable, within a custom designed manifold, capable of loading separate solutions into each of the four micro-channels, creating a high-throughput flow through demountable multi- (4) channel transmission cell. In principle the design is workable, as it was successfully loaded with aqueous dye solutions, ethanol solutions, and aqueous NaN₃ solutions – however due to practical considerations around the loading of the cell, and the demountable design - more extensive experimentation was not possible. The main limitation of the design has to do with the fluid loading - the macro/micro interface, which is traditionally a problem with the design of micro-fluidic devices. In order to ensure that the fluid was loaded, the micro-fabricated cell had to be perfectly in line with the drilled top cell – where repeated separation of the cell for realignment led to degradation of the micro-fluidic channels. The idea of a demountable micro-fluidic system is attractive in the sense that it allows for cleaning of small debris from the micro-channels which would otherwise render a sealed cell system unusable – however it also exposes the system to potential damage.

Additionally, the design of the micro-channels themselves could be better for the purposes of maximizing the fluid channels in the field of view of the FPA. Roughly 50% of the pixels are lost due to the channel barriers, and even when the channels are aligned evenly it is not possible to fully fit each of the four under the field of view of the 32x32 FPA. The upgrade to the 64x64 FPA does encompass the entire channel system, and also gives access to the branching points allowing for the extraction of much more data from each channel. A potential solution to this problem would be to utilize the laminar flow characteristics of micro-flows, and design a cell which would run multiple fluid streams together and directing the resultant grouping of fluid streams into an area equivalent of the FPA field of view. This would eliminate the presence of the polymer, and also the remaining residue problem seen within the micro-channel structures of the current design. The gradient of the polymer residual does appear to completely dissipate in some points, however this is the exception and in most sampling points there is always a presence of an SU-8 signal which is very strong in the finger print region. This had consequences on the sampling schemes used, whereby it was shown to be effective to collect a background of the empty multichannel cell for subtraction from the loaded channels; noise performance within the center of the channel structures was equivalent to the noise performance of a clean cell for the measured regions. The fingerprint region was significantly affected by the presence of the residual polymer and subtraction was less effective, a serious drawback for the sensitivity of the current design.

Overall the high-throughput potential of the multichannel transmission cell combined with the FPA-FTIR detector has been demonstrated. The hardware will need improvement in order to conduct more thorough investigations of this approach for HTS analysis, and the cell design should be modified taking into consideration the observations made from the above experiments. Multiple fluid streams have been monitored, and a moderate quality calibration curve constructed off of a 'single' detector, something that has not been accomplished before with FPA detectors in the literature. The ability to monitor live streams of sample based on a color gradient could provide an efficient screening technique, while expanding the FPA (n = 64, 128, 256...) could increase the number of simultaneously monitored channels. With the increasing capabilities of FPA detectors, such a system could be very feasible for making sub milliabsorbance FTIR measurements of multiple fluid streams.

Chapter 6. Research Summary and Conclusions

The response distributions for the detector elements of an FPA camera within an FTIR imaging spectrometer have been characterized. The noise level of the MCT-FPA $(^2x10^{-4} - RMS; 256 \text{ co-additions and } 8\text{cm}^{-1} \text{ resolution, integration energy } > 7000)$ as an average of 1024 pixels is inferior to that of the single point DTGS and MCT detectors by 1 and 2 orders of magnitude respectively. Using the above scanning conditions, the SD of the noise within the FPA detector elements is ~10⁻⁴, with a CV for all detector elements of approximately 50%, where there is a strongly right skewed distribution of this noise. Looking closer at the distribution of noise and the 2D representations of that response, it is apparent that the NUC performed on the FPA prior to analysis (using instrument software) is not fully correcting the problem, i.e. the non-random spatial noise is quite noticeable (every 4th row & several even numbered columns) and is largely attributed to the right skew of the pixel noise distribution. Collecting a pre-scan 100% transmission line or using a region from within a samples spectrum allows for the easy removal of pixels from the total based on their noise features. The higher performance pixels of the FPA (in terms of RMS noise) are more tightly distributed; the best cases (top 10% of pixels) on average have a CV of 7 +/- 0.7 %. The effective instrument detection limit (in terms of absorbance) for the average pixel using the above prescribed conditions, post removal of the spatial noise features, sits at 0.003, while the top 10% of pixels within that population have an average of 0.0015. The ability to push the detection limit through careful selection from the pixel population is feasible, but this is limited in its repeatability as the average pixel has a RMS noise CV value of roughly 20%.

The level of peak response distribution was evaluated using solid and liquid samples and it was found that the level of variation in detector element response was greater than that expected based solely on their noise characteristics. Within the decided dynamic range of the average detector element (0.2-0.8 absorbance) the CV value for repeated measurements saw the greatest proportion of stable pixels (95% of pixels with a repeatability CV of 2% or less, for 20 measurements), however outside of this range there was a rapid degradation in individual detector element consistency. It was noted that with the linear regression modeling in chapter 4, the SD of the pixel response for the standards peak increased with concentration even when built to keep within the decided dynamic range of the FPA. This is due to the fact that each detector element

generates a linear response unique of its neighbor, and thus will generate a different sensitivity, resulting in the widening of the pixel data within the calibration— i.e. the mean value might be 0.8, but a proportion of those pixels will be greater than even 1.0.

The linear regression modeling of the detector elements acted as an extension of the work conducted in chapter 3, and it found that a significant proportion of pixels were able to construct reasonably linear calibration curves from the varying concentrations of NaN_3 in aqueous solutions, and milk samples. The main measures of linear regression analyzed (CSD and R^2) were more effective than the RMS noise filter approach yielding a better predictive accuracy, in terms of %RE from a true value determined with a validation standard,. The same non-random spatial features were present for each of the calibration features, although it was apparent that the correlation between noise and these calibration parameters is not as direct as one might think, based on the pixel selection procedures developed. Overall for the optimized scanning conditions, a precalibration will allow for the selection of pixels with a CSD mean of 0.0125 +/- 0.0046 (based on the ideal situation of the NaN_3 calibrated data).

A factor not mentioned up to this point is the time of analysis required to achieve the milli-absorbance SNR and the minimized level of response distribution; roughly 3 minutes of scanning are required for the current conditions, which is certainly not appropriate for a high-throughput analysis tool. Improvements in the achievable SNR and the response time and data downloading from the FPA detector will need improvement to be truly applicable to accurate quantitative analysis in a highthroughput application. As with the design of the multi-cell sampling accessory, speed is of the essence if such an accessory were ever to be taken seriously – although the level of scan speed for the FPA-FTIR is compensated for by the fact that the prototype system is capable of collecting from multiple channels of sample simultaneously. Thus, even if instrument designers are able to achieve FPA-FTIR performance which is still two times slower than the conventional DTGS detector, there will still be the potential to put through two times as many samples with the current multichannel design. Alternatively, if fabrication processes are improved to the point that the number of fluid streams in the FPA field of view are increased to 8, 16, 32 etc, this would easily compensate for the time of analysis limitation of current FPA-FTIR spectrometers.

The points discussed in chapter 5 about the limitations around the micro-fluidic multichannel demountable transmission cell are some of the biggest limitations to the current work. The fact that the loading of the cell with fluids was never satisfactorily solved reflects an ongoing difficulty within the field of micro-fluidics - connecting the macro to the micro. The design of the current prototype calls for the easy disassembly of the entire manifold/cell. If the demountable design is to work efficiently, the connections on the manifold must be redesigned in order to withstand the very high pressure build up put onto the system, they must minimize the dead volume in order to have more efficient flushing of the micro-channel system, and the alignment of the multichannel cell plates must be better controlled by some type of locking/placing mechanism. The multichannel fabrication technique used in this study was excellent in that it held up nicely to the fluid pressures, it was quite durable considering the amount of handling that it endured through the study, and it maintained efficient separation of the fluids within the channels when loaded. The problems which have been highlighted are to do mainly with the residual polymer post development in the micro-fabrication process, and the sensitivity of the polymer adhesion after repeated disassembly of the apparatus. The sensitivity of the system is hardly a surprise due to the nature of the delicately positioned channel barriers, but if the current design is ever to be used in a practical light, a degree of confidence must subsist with their structural integrity.

The FPA-FTIR analysis of multiple fluid streams has been accomplished, and it has been demonstrated that it is possible to perform 4 times the work in a single scan. The extensive analysis of the FPA-FTIR in chapters 3 and 4 has illustrated the potential of the technique to monitor much more data streams than just 4 – that actually there is no appreciable benefit (in terms of predictive accuracy) to co-adding 256 pixels of data or 32. This means that after careful inspection and removal of erratic and/or non-random 'bad' pixels from the pixel population, it is quite safe to say that one column or one row equals that of the neighboring column or row. Where one has to exercise caution is when looking to use individual pixels of data from the FPA as a reliable response relative to its neighbor. Although a good proportion of pixels have been shown to have a relatively stable response, the level of stability is itself subject to a distribution – and there is the issue of the spatial noise pattern which affects a select group of pixels consistently. Comparing an individual pixels prediction to another is difficult even after a

linear regression modeling of the entire pixel population and this again is likely due to the nature of the pixels themselves and the inability to accurately correct for nonuniformity using a two point correction.

Citations:

- 1. J. C. Tate, P; Guenard, RD; Harner, R, ed., *Process Monitoring by Mid- and Near-Infrared Fourier Transform Spectroscopy*, John Wiley & Sons Inc., New York, 2006.
- 2. F. R. van de Voort and A. A. Ismail, *Trends in Food Science & Technology*, 1991, **2**, 13-17.
- 3. J. D. S. GOULDEN, J. SHIELDS and R. HASWELL, *International Journal of Dairy Technology*, 1964, **17**, 28-33.
- 4. R. Bauer, H. Nieuwoudt, F. F. Bauer, J. Kossmann, K. R. Koch and K. H. Esbensen, *Analytical Chemistry*, 2008, **80**, 1371-1379.
- 5. N. Noronha, E. Duggan, G. R. Ziegler, J. J. Stapleton, E. D. O'Riordan and M. O'Sullivan, *Food Res. Int.*, 2008, **41**, 472-479.
- 6. R. Bhargava, *Analytical and Bioanalytical Chemistry*, 2007, **389**, 1155-1169.
- 7. K. Flynn, R. O'Leary, C. Roux and B. J. Reedy, *Journal of Forensic Sciences*, 2006, **51**, 586-596.
- 8. G. Steiner and E. Koch, *Analytical and Bioanalytical Chemistry*, 2009, **394**, 671-678.
- 9. N. Sheppard, in *Handbook of Vibrational Spectroscopy*, ed. P. R. Griffiths, John Wiley & Sons, Ltd., New York, Editon edn., 2006, vol. 1.
- 10. A. Rogalski, *Progress in Quantum Electronics*, 2003, **27**, 59-210.
- 11. M. Ford, in *Handbook for Vibrational Spectroscopy*, ed. P. R. Griffiths, John Wiley & Sons, Ltd., New York, Editon edn., 2006, vol. 1.
- 12. L. M. Mihaly, M.C., Wiley-VCH Verlag GmbH & Co., Weinheim, Editon edn., 2009.
- 13. J. M. Chalmers, in *Handbook of Vibrational Spectroscopy*, ed. P. R. Griffiths, John Wiley & Sons Ltd., New York, Editon edn., 2006.
- 14. I. W. L. R. Bhargava, *Appl. Spectrosc.*, 2001, **3**, 57-70.
- A. Sommer, ed., Mid-infrared Transmission Microspectroscopy, John Wiley & Sons, New York, 2006.
- 16. I. W. Levin and R. Bhargava, Annu. Rev. Phys. Chem., 2005, **56**, 429-474.
- 17. J. Gallet, M. Riley, Z. Hao and M. C. Martin, *Infrared Physics & Technology*, 2008, **51**, 420-422.
- 18. P. D. L.M. Miller, *Biochimica et Biophysica Acta (BBA) Biomembranes*, 2006, **1758**, 846-857.
- 19. A. Ghetler, McGill, 2009.
- 20. C. Couts-Lendon and J. L. Koenig, *Appl. Spectrosc.*, 2005, **59**, 717-723.
- 21. M. J. Nasse, R. Reininger, T. Kubala, S. Janowski and C. Hirschmugl, *Nuclear Instruments & Methods in Physics Research Section a-Accelerators Spectrometers Detectors and Associated Equipment*, 2007, **582**, 107-110.
- 22. E. B. Theocharous, J.R., in *Handbook of Vibrational Spectroscopy*, ed. P. R. Griffiths, Jong Wiley & Sons, Inc, New York, Editon edn., 2006, vol. 1.
- 23. C. M. Snively and J. L. Koenig, *Appl. Spectrosc.*, 1999, **53**, 170-177.
- 24. E. Theocharous, Infrared Physics & Technology, 2006, 48, 175-180.
- 25. L. H. H. Kidder, A. S.; Lewis, E. N., in *Handbook of Vibrational Spectroscopy*, ed. P. R. Griffiths, John Wiley & Sons Inc., New York, Editon edn., 2002.
- 26. E. N. Lewis, P. J. Treado, R. C. Reeder, G. M. Story, A. E. Dowrey, C. Marcott and I. W. Levin, *Analytical Chemistry*, 1995, **67**, 3377-3381.

- 27. C. P. I. Pelletier, *Appl. Spectrosc.*, 2005, **59**, 156-163.
- 28. R. B. Ira W. Levin, *Annu. Rev. Phys. Chem.*, 2005, **56**, 429-474.
- 29. M. R. K. Dean A. Scribner, Joseph M. Killiany, *Proceedings of the IEEE*, 1991, **79**, 66-85.
- 30. P. R. H. Griffiths, de J.A., in *Fourier Transform Infrared Spectrometry*, John Wiley & Sons Inc, Hoboken, NJ, USA, Editon edn., 2007, pp. 303-320.
- 31. M. Z. Tidrow, Materials Science and Engineering, 2000, **B74**, 45-51.
- 32. M. Y. T. S. Eminoglu, T. Akin, *J. Microelectromech Sys.*, 2008, **17**, 20-30.
- 33. F. D. S. Jonathan M. Mooney, William S. Ewing, James E. Murguia, Jerry Silverman, *Optical Engineering*, 1989, **28**, 1151-1161.
- 34. R. R. P. Phillip L. Jacobson, Aaron Koskelo, Robert C. Quick, Jerry Romero, *Chemical and Biological Sensing II*, 2001, **4378**, 71-81.
- 35. M. Schulz and L. Caldwell, *Infrared Physics & Technology*, 1995, **36**, 763-777.
- 36. J. M. Mooney and F. D. Shepherd, *Infrared Physics & Technology*, 1996, **37**, 595-606.
- 37. S. Rainieri and G. Pagliarini, *Infrared Physics & Technology*, 2002, **43**, 345-351.
- 38. W. W. Jason Morrison, Jitendra Paliwal, CSBE/ASABE Intersectional Conference, Paper Number: MBSK 06-108, Saskatoon Saskatchewan, 2006.
- 39. R. C. Hardie and D. R. Droege, *Eurasip Journal on Advances in Signal Processing*, 2007.
- 40. C. S. Martin, S. Torres and J. E. Pezoa, *Infrared Physics & Technology*, 2008, **51**, 564-571.
- 41. J. Baars, Optical Materials, 1996, **6**, 41-54.
- 42. R. H. Hannah, in *Handbook of Vibrational Spectroscopy*, ed. P. R. Griffiths, John Wiley & Sons Ltd., New York, Editon edn., 2006, vol. 1.
- 43. F. R. V. d. V. Jacqueline Sedman, Ashraf A. Ismail, ed., *Attenuated Total Reflectance Spectroscopy: Principles and Applications in Infrared Analysis of Food*, Marcel Decker Inc, New York, 1998.
- 44. J. Grdadolnik, *Acta. Chim. Slov*, 2002, **49**, 631-642.
- 45. H. Mark, in *Handbook of Vibrational Spectroscopy*, ed. P. R. Griffiths, John Wiley & Sons, New York, Editon edn., 2006.
- 46. K. C. Danzer, L.A;, Pure & Appl. Chem., 1998, **70**, 993-1014.
- 47. P. R. Griffiths, in *Handbook of Vibrational Spectroscopy*, ed. P. R. Griffiths, John Wiley & Sons Inc., New York, Editon edn., 2006, vol. 1.
- 48. R. Corporation, *Multiple Linear Regression Analysis*, http://www.weibull.com/DOEWeb/multiple_linear_regression_analysis.htm, Accessed Dec-16, 2009.
- 49. B. Nadler and R. R. Coifman, Journal of Chemometrics, 2005, 19, 107-118.
- 50. F. R. Vandevoort, J. Sedman, G. Emo and A. A. Ismail, *Journal of Aoac International*, 1992, **75**, 780-785.
- 51. F. Ulberth and M. Henninger, Journal of Dairy Research, 1994, 61, 517-527.
- 52. N. Nathierdufour, J. Sedman and F. R. Vandevoort, *Milchwissenschaft-Milk Science International*, 1995, **50**, 462-466.
- 53. E. A. M. deJong and J. Kaper, *Netherlands Milk and Dairy Journal*, 1996, **50**, 35-51.
- 54. A. K. Hewavitharana and B. vanBrakel, *Analyst*, 1997, **122**, 701-704.
- 55. P. W. Hansen, Milchwissenschaft-Milk Science International, 1998, **53**, 251-255.

- 56. C. Heuer, H. J. Luinge, E. T. G. Lutz, Y. H. Schukken, J. H. van der Maas, H. Wilmink and J. Noordhuizen, *Journal of Dairy Science*, 2001, **84**, 575-582.
- 57. R. A. Cocciardi, A. A. Ismail, F. R. Van de Voort and J. Sedman, *Milchwissenschaft*, 2002, **57**, 90-93.
- 58. S. Sivakesava and J. Irudayaraj, *Journal of Dairy Science*, 2002, **85**, 487-493.
- 59. F. A. Inon, S. Garrigues and M. de la Guardia, *Analytica Chimica Acta*, 2004, **513**, 401-412.
- 60. Y. E. Deng, Q. Zhou and S. Q. Sun, *Spectroscopy and Spectral Analysis*, 2006, **26**, 636-639.
- 61. N. Nicolaou and R. Goodacre, *Analyst*, 2008, **133**, 1424-1431.
- 62. P. Uden and L. O. Sjaunja, *Anim. Feed Sci. Technol.*, 2009, **152**, 123-132.
- 63. M. Gallignani, C. Ayala, M. D. Brunetto, J. L. Burguera and M. Burguera, *Talanta*, 2005, **68**, 470-479.
- 64. R. T. Wilson, HS, Trends in Analytical Chemistry, 1999, 18, 85-93.
- 65. R. Schindler, R. Vonach, B. Lendl and R. Kellner, *Fresenius Journal of Analytical Chemistry*, 1998, **362**, 130-136.
- 66. M. Haberkorn, P. Hinsmann and B. Lendl, *Analyst*, 2002, **127**, 109-113.
- 67. R. A. Cocciardi, A. A. Ismail and J. Sedman, *Journal of Agricultural and Food Chemistry*, 2005, **53**, 2803-2809.
- 68. V. Dixit, J. C. Tewari, B. K. Cho and J. M. K. Irudayaraj, *Appl. Spectrosc.*, 2005, **59**, 1553-1561.
- 69. J. L. Moreira and L. Santos, *Analytical and Bioanalytical Chemistry*, 2005, **382**, 421-425.
- 70. A. P. Lobo, B. S. Valles, N. F. Tascon, R. R. Madrera and O. F. Garcia, 2006.
- 71. K. Fernandez and E. Agosin, *Journal of Agricultural and Food Chemistry*, 2007, **55**, 7294-7300.
- 72. D. W. Lachenmeier, *Food Chemistry*, 2007, **101**, 825-832.
- 73. N. Tena, R. Aparicio and D. L. Garcia-Gonzalez, *Journal of Agricultural and Food Chemistry*, 2009, **57**, 9997-10003.
- 74. A. A. Christy and P. K. Egeberg, *Chemometrics and Intelligent Laboratory Systems*, 2006, **82**, 130-136.
- 75. J. Dubois, F. R. vandeVoort, J. Sedman, A. A. Ismail and H. R. Ramaswamy, *Journal of the American Oil Chemists Society*, 1996, **73**, 787-794.
- 76. A. A. Ismail, F. R. Vandevoort, G. Emo and J. Sedman, *Journal of the American Oil Chemists Society*, 1993, **70**, 335-341.
- 77. P. C. Tabeling, S., *Introduction to Microfluidics*, Oxford University Press Inc., New York, 2005.
- 78. G. M. Whitesides, *Nature*, 2006, **442**, 368-373.
- 79. S. E. Ong, S. Zhang, H. J. Du and Y. Q. Fu, *Frontiers in Bioscience*, 2008, **13**, 2757-2773.
- 80. Y. Y. Yan, *Journal of Bionic Engineering*, 2007, **4**, 97-107.
- 81. D. B. Weibel and G. M. Whitesides, *Current Opinion in Chemical Biology*, 2006, **10**, 584-591.
- 82. N. Lion, F. Reymond, H. H. Girault and J. S. Rossier, *Current Opinion in Biotechnology*, 2004, **15**, 31-37.
- 83. H. Bruus, *Theoretical Microfluidics*, Oxford University Press Inc., New York, 2008.
- 84. N. T. W. Nguyen, S.T., *Fundementals and Applications of Microfluidics*, Artech House Inc., Norwood, 2002.

- 85. O. Skurtys and J. M. Aguilera, Food Biophysics, 2008, 3, 1-15.
- 86. D. Janasek, J. Franzke and A. Manz, *Nature*, 2006, **442**, 374-380.
- 87. D. Dutta, A. Ramachandran and D. T. Leighton, *Microfluidics and Nanofluidics*, 2006, **2**, 275-290.
- 88. N. T. Nguyen, X. Y. Huang and T. K. Chuan, *Journal of Fluids Engineering-Transactions of the Asme*, 2002, **124**, 384-392.
- 89. C. C. Chang and R. J. Yang, Microfluidics and Nanofluidics, 2007, 3, 501-525.
- 90. J. G. Santiago, *Analytical Chemistry*, 2001, **73**, 2353-2365.
- 91. T. M. Squires and M. Z. Bazant, *Journal of Fluid Mechanics*, 2004, **509**, 217-252.
- 92. V. Tesar, *Pressure Driven Microfluidics*, Artech House Inc., Norwood, 2007.
- 93. A. E. Herr, J. I. Molho, J. G. Santiago, M. G. Mungal, T. W. Kenny and M. G. Garguilo, *Analytical Chemistry*, 2000, **72**, 1053-1057.
- 94. D. J. Laser and J. G. Santiago, *Journal of Micromechanics and Microengineering*, 2004, **14**, R35-R64.
- 95. F. Tay, *Microfluidics and BioMEMS Applications*, Kluwer Academic Publishers, Boston, 2002.
- 96. S. G. Kazarian, *Analytical and Bioanalytical Chemistry*, 2007, **388**, 529-532.
- 97. R. Schindler and B. Lendl, *Analytical Communications*, 1999, **36**, 123-126.
- 98. S. Armenta, S. Garrigues and M. de la Guardia, *Trac-Trends in Analytical Chemistry*, 2007, **26**, 775-787.
- 99. K. B. Mogensen, H. Klank and J. P. Kutter, *Electrophoresis*, 2004, **25**, 3498-3512.
- 100. C. M. Snively, G. Oskarsdottir and J. Lauterbach, *Catalysis Today*, 2001, **67**, 357-368.
- 101. S. G. Kazarian, K. L. A. Chan, V. Maquet and A. R. Boccaccini, *Biomaterials*, 2004, **25**, 3931-3938.
- 102. K. L. A. Chan and S. G. Kazarian, *Journal of Combinatorial Chemistry*, 2005, **7**, 185-189.
- 103. K. L. A. Chan and S. G. Kazarian, *Lab on a Chip*, 2006, **6**, 864-870.
- 104. K. L. A. Chan and S. G. Kazarian, *Analyst*, 2006, **131**, 126-131.
- K. L. A. Chan, S. Gulati, J. B. Edel, A. J. de Mello and S. G. Kazarian, *Lab on a Chip*, 2009, 9, 2909-2913.
- 106. K. L. A. Chan and S. G. Kazarian, *Journal of Combinatorial Chemistry*, 2006, **8**, 26-31.
- 107. J. Kirkwood, S. F. Al-Khaldi, M. M. Mossoba, J. Sedman and A. A. Ismail, *Appl. Spectrosc.*, 2004, **58**, 1364-1368.
- 108. N. Kaun, M. J. Vellekoop and B. Lendl, *Appl. Spectrosc.*, 2006, **60**, 1273-1278.
- 109. P. Hinsmann, M. Haberkorn, J. Frank, P. Svasek, M. Harasek and B. Lendl, *Appl. Spectrosc.*, 2001, **55**, 241-251.
- 110. M. Kakuta, P. Hinsmann, A. Manz and B. Lendl, Lab on a Chip, 2003, 3, 82-85.
- 111. R. Masuch and D. A. Moss, *Appl. Spectrosc.*, 2003, **57**, 1407-1418.
- 112. T. Jia and G. Feng, *Appl. Spectrosc.*, 2006, **60**, 1477-1481.
- 113. V. Namasivayam, R. S. Lin, B. Johnson, S. Brahmasandra, Z. Razzacki, D. T. Burke and M. A. Burns, *Journal of Micromechanics and Microengineering*, 2004, **14**, 81-90.
- 114. P. J. Viskari and J. P. Landers, *Electrophoresis*, 2006, **27**, 1797-1810.
- 115. C. Q. Yi, Q. Zhang, C. W. Li, J. Yang, J. L. Zhao and M. S. Yang, *Analytical and Bioanalytical Chemistry*, 2006, **384**, 1259-1268.

- 116. C. Ricci, P. Phiriyavityopas, N. Curum, K. L. A. Chan, S. Jickells and S. G. Kazarian, *Appl. Spectrosc.*, 2007, **61**, 514-522.
- 117. S. G. Kazarian, K. W. T. Kong, M. Bajomo, J. Van der Weerd and K. L. A. Chan, *Food and Bioproducts Processing*, 2005, **83**, 127-135.
- 118. R. Bhargava and I. W. Levin, *Appl. Spectrosc.*, 2003, **57**, 357-366.
- 119. R. T. M. Fraser, *Analytical Chemistry*, 1959, **31**, 1602-1603.
- 120. J. Hong, J. B. Edel and A. J. deMello, *Drug Discovery Today*, 2009, **14**, 134-146.
- 121. P. I. Okagbare and S. A. Soper, *Analyst*, 2009, **134**, 97-106.
- 122. C. Petibois and G. Déléris, *Trends in Biotechnology*, 2006, **24**, 455-462.
- 123. M. Tahtouh, P. Despland, R. Shimmon, J. R. Kalman and B. J. Reedy, *Journal of Forensic Sciences*, 2007, **52**, 1089-1096.
- 124. J. Pajander, S. Matero, A. M. Soikkeli, O. Korhonen, A. Poso and I. Ketolainen, *European Journal of Pharmaceutical Sciences*, 2006, **28**, S37-S37.